THE EFFECT OF CARBON CONTENT ON THE MECHANICAL PROPERTIES AND MICROSTRUCTURAL EVOLUTION OF FE-22MN-C TWIP / TRIP STEELS

THE EFFECT OF CARBON CONTENT ON THE MECHANICAL PROPERTIES AND MICROSTRUCTURAL EVOLUTION OF FE-22MN-C TWIP / TRIP STEELS

BY

EILEEN EVA YANG, B. ENG.

A Thesis

Submitted to the School of Graduate Studies

in Partial Fulfilment of the Requirements for the Degree

Master of Applied Science

McMaster University

MASTER OF APPLIED SCIENCE (2010) McMaster University

(Materials Science and Engineering) Hamilton, Ontario

TITLE: The Effect of Carbon Content on the Mechanical Properties and Microstructural Evolution of Fe-22Mn-C TWIP / TRIP Steels

AUTHOR: Eileen Eva Yang, B. Eng (McMaster University)

SUPERVISORS: Professor J.R. McDermid

Professor H.Z. Zurob

NUMBER OF PAGES: xvi, 136

ABSTRACT

The development of new materials with a combination of high strength and ductility is required for the automotive industry, due to the demand for increased fuel efficiency while maintaining vehicle safety and performance. High-Mn steels combine exceptional strength and ductility to achieve the sustained rates of high work hardening required to achieve these objectives. Fe-22Mn-C alloys containing strain-induced deformation products (twins and ε-martensite) contribute to the high work hardening rates by acting as boundaries for dislocation motion. Three Fe-22Mn-C alloys were investigated with varying carbon contents of 0.6, 0.4 and 0.2 wt% and stacking fault energies (SFEs) of 37.2, 33.4 and 29.6 mJ/m^2, respectively. Their microstructural evolution and mechanical properties were evaluated.

The as-annealed Fe-22Mn-0.6C alloy comprised an austenitic microstructure, produced twins during deformation and had the highest sustained work hardening rate of the three alloys. The kinematic hardening contribution was due to the production of twins during deformation, adding to the overall flow stress. The flow stress was successfully modeled with contributions from the yield strength, isotropic hardening and kinematic hardening. The main damage mechanism was the separation of grain boundaries and the production of twins during deformation classified the 0.6C alloy as a TWIP steel.

The Fe-22Mn-0.4C alloy displayed an austenitic matrix in the as-annealed microstructure with twins and ε-martensite produced during deformation. The work hardening rate was sustained from the continuous production of deformation products.

The kinematic hardening contributed to the overall flow stress as a result of twins and ε-martensite acting as dislocation barriers. The mechanical behaviour of the alloy was modeled successfully by combining the yield strength, isotropic and kinematic hardening contributions to obtain the overall flow stress. Decohesion at γ - ε interfaces was observed to be the primary fracture mechanism. With the production of both twins and ε-martensite, the 0.4C alloy was labelled as a TWIP / TRIP steel.

The Fe-22Mn-0.2C alloy had the lowest carbon content of the three alloys and contained an initial dual phase microstructure of austenite and ε-martensite plates. Strain-induced ε-martensite was created during tensile deformation, with the kinematic hardening contribution resulting from the production of ε-martensite. An iso-work model was applied with contributions from the isotropic hardening of austenite and kinematic hardening of ε-martensite to the overall flow stress. Fracture was caused by separation along austenite – ε-martensite interfaces. The strain-induced ε-martensite created a TRIP effect within the 0.2C alloy.

Overall, the effect of carbon content on the microstructural evolution and mechanical properties within the Fe-22Mn-C system was determined. As the carbon content decreased, the SFE was lowered and a shift from the TWIP to TRIP effect was observed. The SFE phase map predictions were correct in predicting the as-annealed microstructure and deformation mechanism as determined by Allain et al. (Allain 2004b) and Nakano (Nakano 2010). The transformation kinetics and the role of carbon were not included in the SFE phase map predictions and were also factors to consider on the effect of carbon content on the Fe-22Mn-C alloys.

ACKNOWLEDGEMENTS

I would like to acknowledge and sincerely thank Dr. Joe McDermid and Dr. Hatem Zurob, my patient supervisors for their help, guidance and support these past few years. Their steady guidance and direction has helped me achieve my academic goals. Thank you for believing in me, and for investing time, effort and finances into me as well.

Thanks to Dr. Xiang Wang for his help with TEM analysis, Chris Butcher for constant help and guidance all things microscopy related, Dr. Steve Koprich for SEM training and his constant reliability, Rob Lemmon for his expertise with tensile testing, and Doug, John and Ed for their technical lab help and ALWAYS having fun while doing it.

Thanks to Elvira and the materials department for their administrative help. They were like a help center and also had the greatest snacks.

Thanks to Preeti for her friendship, trusty coffee breaks and for always having a friend to turn to when experiments seem to be unending, papers needed writing and meetings were looming. Thanks to Erika for showing me the ropes when I first arrived and for teaching me the "ins" and "outs" to many things. I enjoyed our chats and discussions in the office.

Thanks to my family and friends (esp. Lou) for their unending support and steadfast love these past years as this endeavour was not an easy one. They were beside me through it all and listened to me in times of doubt and frustration and in times of great joy.

Eileen Eva Yang

TABLE OF CONTENTS

Abstract iii

Acknowledgements v

Table Of Contents vi

List of Figures xi

List of Tables xvi

1. Introduction 1

2. Literature Review 3

2.1 Phase Transformations 3

2.1.1. Stacking Fault Energy 3

2.1.2. Twin Formation 8

2.1.3. ε-Martensite Formation 10

2.2 Work Hardening 12

2.2.1. Isotropic Strain Hardening 12

2.2.2. Kinematic Strain Hardening 14

2.3 TWIP Steels 16

2.4 TRIP Steels 17

2.5 High Mn TWIP/TRIP Alloys 19

2.5.1. Fe-30Mn Steel 19

2.5.2. Fe-24Mn TRIP Steel 20

2.5.3. Fe-22Mn-0.6C TWIP Steel 23

2.5.4. Fe-22Mn-0.376C TWIP / TRIP Steel 29

2.6 TWIP Model and the Effect of Chemical Composition 30

2.7 Iso-Work Model 32

3. Objectives 33

4. Experimental Method 34

4.1 Starting Material 34

4.2 Heat Treatment and Decarburization 35

4.3 Mechanical Tensile Testing 36

4.3.1. Monotonic Tensile Tests 37

4.3.2. Interrupted Tensile Tests 37

4.3.3. Load-Unload Tensile Tests 38

4.4 Fracture Analysis 40

4.5 Metallographic Sample Preparation 41

4.5.1. Cutting and Mounting 41

4.5.2. Polishing 42

4.5.3. Etching 42

4.5.4. Electropolishing 43

4.5.5. TEM Sample Preparation 43

4.6 Materials Characterization Techniques 44

4.6.1. Scanning Electron Microscopy (SEM) 44

4.6.2. Electron BackScattered Diffraction (EBSD) 45

4.6.3. Transmission Electron Microscope (TEM) 46

4.6.4. X-Ray Diffraction (XRD) 46

5. Results 48

5.1 As-Annealed Steels 48

5.2 Mechanical Properties 51

5.2.1. Monotonic Tensile Behaviour to Fracture 51

5.2.2. Work Hardening Response 55

5.2.3. Kinematic Hardening 56

5.2.4. XRD Phase Analysis 60

5.3 0.6C Alloy Microstructural Evolution vs. Strain 62

5.3.1. SEM Observations 62

5.3.2. EBSD Phase Maps 65

5.4 0.4C Alloy Microstructural Evolution vs. Strain 67

5.4.1. SEM Observations 67

5.4.2. EBSD Phase Maps 68

5.4.3. TEM Analysis 70

5.5 0.2C Alloy Microstructural Evolution vs. Strain 77

5.5.1. SEM Observations 77

5.5.2. EBSD Phase Maps 78

5.5.3. TEM Analysis 80

5.6 Fracture 85

5.6.1. 0.6C Alloy 86

5.6.2. 0.4C Alloy 88

5.6.3. 0.2C Alloy 91

6. Discussion 94

6.1 0.6C Alloy Summary and Analysis 94

6.2 0.4C Alloy Summary and Analysis 97

6.3 Modeling 0.6C and 0.4C Mechanical Behaviour 100

6.4 0.2C Alloy Summary and Analysis 111

6.5 Modeling 0.2C Mechanical Behaviour 113

6.6 Analysis on Effect of Carbon Content 118

7. Conclusions 121

8. References 125

9. APPENDIX 132

9.1 CO/CO_2 Decarburization Equations 132

9.2 Calculating CO/CO_2 Gas Ratios 133

9.3 Detailed Mounting Conditions 135

9.4 Detailed Polishing Conditions 135

9.5 Detailed Etching Conditions 136

LIST OF FIGURES

Figure 1.1 Strength – Ductility Balance for New Ferrous Alloys (De Cooman 2009) 2

Figure 2.1 FCC Stacking Sequence with Dissociation of Burgers Vector b_1 into Partials b_2 and b_3 (Venables 1963) 3

Figure 2.2 Deformation Structures as a Function of SFE a) at Room Temperature (Rémy 1976) b) as a Function of Temperature (Rémy 1977) 7

Figure 2.3 SFE Map Based on Carbon/Manganese (wt%) with ε-Martensite Limits (Allain 2004b) 7

Figure 2.4 Fe-Mn-C Phase Stability Diagram at 298K a) After Quenching b) After Tensile Testing (Scott 2005) 8

Figure 2.5 SFE Map with ε-Martensite Boundaries (Nakano 2010) 8

Figure 2.6 Twin Nucleation a) Stacking Sequence b) Crystal Structure Before and After Twinning (Kelly 1970) 9

Figure 2.7 Twin Nucleation Dislocation Model a) Twin-Matrix Interface b) Dislocation Representing Strain Field c) Thin Twin Dislocation Model (Kelly 1970) 10

Figure 2.8 Stacking Sequence in HCP ε-Martensite Nucleation (Bracke 2006) 11

Figure 2.9 HREM of Layered Structure of ε-Martensite with Processed Imaged Inset on Right Assuming Atoms are White (Putaux 1996) 11

Figure 2.10 Effect of Temperature and Strain Rate for 1) RT 2) 100°C 3) 200°C 14

Figure 2.11 Typical Bauschinger Effect during Forward and Reverse Flow Test (Sowerby 1979) 15

Figure 2.12 Back Stress Development as a Function of Strain (Bouaziz 2008) 16

Figure 2.13 Illustration of TWIP effect by a) Bouaziz and Embury (Bouaziz 2007) b) De Cooman et al. (DeCooman 2009) 17

Figure 2.14 Comparison of True Stress – Strain for TRIP and TWIP Steels (Frommeyer 2003) 18

Figure 2.15 EBSD Phase Map of Fe-30Mn Annealed Microstructure (Liang 2008) 20

Figure 2.16 TEM Images of a) Annealed Microstructure and b) Well-Developed Cell Structures in Fe-30Mn Alloy (Liang 2008) 20

Figure 2.17 Microstructural Evolution as a Function of Strain for Fe-24Mn (Liang 2008) 21

Figure 2.18 TEM Images of Fe-24Mn Alloy Microstructure at ε_t=0.20 (Liang 2008) 22

Figure 2.19 XRD ε-Martensite Phase Analysis for Fe-30Mn and Fe-24Mn (Liang 2008) 23

Figure 2.20 OM Revealing Grain Boundaries and Twins with Horizontal Tensile Direction at Various Strain Levels a) 0.0 b) 0.18 c) 0.26 d)0.34 (Allain 2004c) 24

Figure 2.21 Effect of Grain Size on a) Tensile Behaviour (Bouaziz 2008) b) Twinning Stress (Gutierrez-Urrutia 2010) 25

Figure 2.22 TEM Images of As-quenched Structure in Fe-22Mn-0.6C Alloy (Wang 2009) 27

Figure 2.23 TEM Images of Microstructure in Fe-22Mn-0.6C Alloy at ε_t=0.20 (Wang 2009) 27

Figure 2.24 TEM Images of Microstructure in Fe-22Mn-0.6C Alloy Cold Rolled to 70% (Wang 2009) 28

Figure 2.25 EBSD Images of Fe-22Mn-0.376C Cold Rolled Samples at Various Strains (Lü 2010) 29

Figure 2.26 Tensile Curves of Various TWIP Steels of a) Experimental Curves of Various Compositions b) Modeled and Experimental Comparison (Bouaziz 2009) 31

Figure 4.1 Tensile Sample Geometry 37

Figure 4.2 Sample Load-Unload Test 39

Figure 4.3 Bauschinger Unloading Loop Behaviour 40

Figure 4.4 OM Image of Fracture Surface Calculation 41

Figure 4.5 Etched Initial Microstructure of 0.4C Alloy 42

Figure 4.6 XRD Set Up by Proto LXRD Machine 47

Figure 5.1 Annealed Microstructure of 0.6C Alloy 49

Figure 5.2 Annealed Microstructure of 0.4C Alloy 49

Figure 5.3 Annealed Microstructure of 0.2C Alloy 50

Figure 5.4 True Stress – Strain Tensile Behaviour for 0.6C Alloy 52

Figure 5.5 True Stress - Strain Tensile Behaviour for 0.4C Alloy 52

Figure 5.6 True Stress - Strain Tensile Behaviour for 0.2C Alloy 53

Figure 5.7 Tensile Behaviour (True Stress - Strain) for All Alloys 54

Figure 5.8 Work Hardening Behaviour for All Alloys 56

Figure 5.9 Overlay of Load-Unload Test and Monotonic Tensile Test for 0.6C Alloy 58

Figure 5.10 Back Stress Development in 0.6C Alloy 58

Figure 5.11 Back Stress Development in 0.4C Alloy 59

Figure 5.12 Back Stress Development in 0.2C Alloy 59

Figure 5.13 XRD ε-Martensite Phase Analysis for All Alloys 61

Figure 5.14 SEM Microstructural Evolution as a Function of Strain for 0.6C Alloy 64

Figure 5.15 EBSD Phase Mapping of Microstructure for 0.6C Alloy 66

Figure 5.16 SEM Microstructural Evolution as a Function of Strain for 0.4C Alloy 68

Figure 5.17 EBSD Phase Mapping of Microstructure for 0.4C Alloy 70

Figure 5.18 TEM BF Images of Deformation Bands and SFs at ε_t=0.10 for 0.4C Alloy . 72

Figure 5.19 TEM BF- DF Images of Austenite and Twin at ε_t=0.10 for 0.4C Alloy 73

Figure 5.20 TEM BF Image of Dislocation Cell Structure at ε_t=0.30 for 0.4C Alloy 74

Figure 5.21 TEM Composite BF Image of Intersecting Deformation Bands at ε_t=0.30 for 0.4C Alloy 75

Figure 5.22 TEM Image of Deformed Microstructure at ε_t=0.30 for 0.4C Alloy..... 76

Figure 5.23 SEM Microstructural Evolution as a Function of Strain for 0.2C Alloy 78

Figure 5.24 EBSD Phase Mapping of Microstructure for 0.2C Alloy 80

Figure 5.25 BF Dislocation, SF and ε-Martensite Interaction for ε_t=0.05 for 0.2C Alloy 81

Figure 5.26 TEM Image of Deformed Microstructure at ε_t=0.05 for 0.2C Alloy..... 82

Figure 5.27 TEM BF Image of ε-Martensite Interaction at ε_t=0.20 for 0.2C Alloy 83

Figure 5.28 TEM Image of Deformed Microstructure at ε_t=0.20 for 0.2C Alloy..... 84

Figure 5.29 Fracture Stress - Strain for All Alloys 86

Figure 5.30 SEM Fracture Features in 0.6C Alloy 87

Figure 5.31 SEM Fracture Surface Cup-Cone Morphology and Voids in 0.6 Alloy..... 88

Figure 5.32 SEM Fracture Features in 0.4C Alloy 89

Figure 5.33 SEM Fracture Surface in 0.4C Alloy..... 90

Figure 5.34 SEM Fracture Features in 0.2C Alloy 92

Figure 5.35 SEM Fracture Surface in 0.2C Alloy 93

Figure 6.1 Kocks and Mecking Voce Equation for 0.6C Alloy 102

Figure 6.2 Tensile Experimental Results and Model Behaviour for 0.6C Alloy 104

Figure 6.3 Individual Modeling Contributions for 0.6C Alloy 105

Figure 6.4 Work Hardening Experimental and Model Comparison for 0.6C Alloy 107

Figure 6.5 Tensile Experimental Results and Model Behaviour for 0.4C Alloy 108

Figure 6.6 Individual Modeling Contributions for 0.4C Alloy 109

Figure 6.7 Work Hardening Experimental and Model Comparison for 0.4C Alloy 111

Figure 6.8 Tensile Experimental Results and Model Behaviour of 0.2C Alloy 115

Figure 6.9 Iso-Work Model Local Stress – Global Strain of 0.2C Alloy 116

Figure 6.10 Iso-Work Model Strain Partitioning of 0.2C Alloy 117

Figure 6.11 Iso-Work Model Stress Partitioning of 0.2C Alloy 118

Figure 9.1 Decarburization Illustration 133

LIST OF TABLES

Table 4.1 Chemical Composition of Steel Alloys (wt%) 34

Table 4.2 Decarburization and Heat Treatment Conditions 36

Table 5.1 Alloy True Mechanical Properties Comparison 54

Table 6.1 Parameter Values for 0.6C and 0.4C Alloy Tensile Property Model 103

Table 6.2 Parameters for 0.2C Iso-Work Model 115

Table 9.1 Thermo-Calc Commands to Determine C Activity 134

Table 9.2 Thermo-Calc Commands to Determine CO/CO_2 Ratio 134

Table 9.3 Activities and Gas Ratios for 0.2C and 0.4C Alloy 135

Table 9.4 Polishing Steps 136

1. INTRODUCTION

Initiatives to reduce carbon footprints, improve sustainability, decrease waste and increase efficiency are current demands for many industries. The automotive industry is looking to improve fuel efficiency and decrease material consumption, while continuing to advance in the development of stronger and safer products. Developing stronger materials with improved energy absorption, which are lighter and thinner, will allow reduced material consumption. With lighter vehicles, fuel efficiency will improve, along with lower CO/CO_2 gas emissions and a reduced green house gas effect. New alloys must be energy absorbent for crash resistance, with high strength and ductility (Grässel 2000, Frommeyer 2003, Scott 2005, Bouaziz 2007, De Cooman 2009).

A class of promising materials are the high-Mn austenitic steels which have shown both high strength and ductility (Bouaziz 2001, Scott 2005). Typically as material strength is improved, ductility (or elongation) is compromised as seen in Figure 1.1, with some different types of materials classified according to their strength and ductility. High-Mn steels move away from the general decreasing trend with a strong combination of both attributes. These high-Mn alloys are a variation of Hadfield steels which contain lower manganese with higher carbon. Hadfield steels contain homogeneous austenite preserved by quenching and have high work hardening rates arising from strain-induced phase transformations (Dastur 1981).

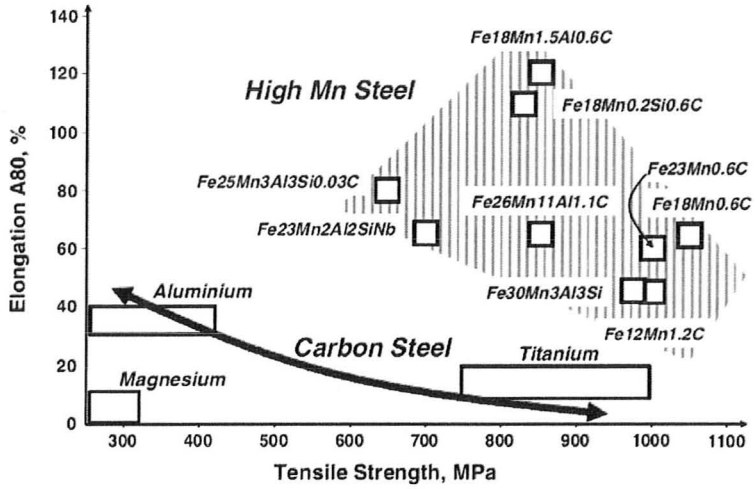

Figure 1.1 Strength – Ductility Balance for New Ferrous Alloys (De Cooman 2009)

Current grades of High-Mn steels usually contain more than 20 wt% Mn with less than 1 wt% C and small amounts of other alloying elements such as silicon or aluminum. The displayed high work hardening rates arise from strain-induced phase transformations during plastic deformation. These strain-induced transformations (twinning induced plasticity - TWIP or transformation induced plasticity - TRIP) are seen to create new "phases" (such as twin boundaries or ε-martensite) which contribute to higher kinematic work hardening rates by continuously introducing new dislocation barriers.

Research on the Fe-22Mn-C system is of interest due to the sustained rates of high work hardening from the strain-induced deformation products. The creation of twins and ε-martensite also act as a dynamic Hall-Petch effect in continuously refining grain size and decreasing the dislocation mean free path (Bouaziz 2001, 2007, 2008, Allain 2004a 2004b 2004c, Scott 2005, Gutierrez-Urrutia 2010).

2. LITERATURE REVIEW

2.1 Phase Transformations

2.1.1. Stacking Fault Energy

Stacking faults (SFs) are planar dislocations that disrupt the stacking sequence of a crystal lattice and the energy associated with them is classified as the stacking fault energy (SFE). In the face-centered cubic (FCC) lattice, a dislocation moving to a new position is often broken down into two Shockley partial dislocations, as the movement of the partial dislocations is more energetically favourable compared to one dislocation movement. With the movement of these planar dislocations, a disruption in the 123123123 (or ABCABCABC) stacking sequence is made, with b_1 as the overall dislocation Burgers vector and b_2 and b_3 as the Shockley partial dislocations in Figure 2.1 (Venables 1963).

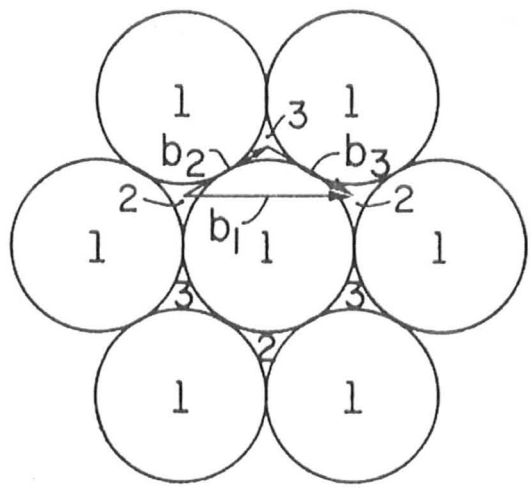

Figure 2.1 FCC Stacking Sequence with Dissociation of Burgers Vector b_1 into Partials b_2 and b_3 (Venables 1963)

Generally, stacking fault partial dislocations are either of the Shockley type or of the Frank type. The Shockley type has the dislocation Burgers vector in the same plane as the fault, while the Frank type has the dislocation Burgers vector normal to the fault plane (Reed-Hill 1992). The distance between the two partial dislocations can be measured and used to calculate the SFE, with more widely separated partial dislocations yielding a lower SFE. The movement of partials determine the type of fault created, with Frank type or intrinsic stacking faults developed by removing part of a close-packed plane, similar to slip of partials on every other plane and acts as an embryo for ε-martensite. Extrinsic stacking faults are produced by inserting a plane that is not correctly stacked or by slip of partials on two neighbouring planes, and acts as an embryo for a twin. Extrinsic stacking faults are less probable than intrinsic stacking faults (Reed-Hill 1992, Olson 1976a).

An ideal and effective SFE can be calculated with the effective SFE considering the effects of strain volume energy, while the ideal SFE neglects the strain energy. The effective SFE is derived from examining the free energy as seen in Equation 2.1, with the asterisk denoting the effective SFE, $\Delta G_{\gamma\rightarrow\varepsilon}$ the difference in free energy of $\gamma \rightarrow \varepsilon$, ΔG_s the strain energy, ρ the atom density in a close packed plane, n the thickness of the faults (usually 2 planes in thickness) and σ the energy of the FCC – HCP phase interface (Olsen 1976a). The molar surface density of the {111} type planes for FCC (ρ) is related to the lattice parameter a and the Avogadro number N (Equation 2.2). Most authors discussing and determining the SFE use the effective SFE rather than the ideal SFE (Olson 1976a, Ferreira 1998, Lee 2000, Nakano 2010).

$$SFE^{*} = n\rho(\Delta G^{\gamma\rightarrow\varepsilon} + \Delta G_S) + 2\sigma \tag{2.1}$$

$$\rho = \frac{4}{\sqrt{3}}\frac{1}{a^2 N} \tag{2.2}$$

2.1.1.1. Effect on Phase Transformation & Deformation Product

As the movement of the partials determine which type of fault is created, the various faults are discussed with their effect on phase transformation. An intrinsic stacking fault is formed by partial dislocation motion on every second plane changing the stacking sequence from the FCC ABCABCABC structure to the HCP ABCA-C-ABC sequence, often referred to as ε-martensite in high-Mn steels. When the partial dislocations move on two consecutive close-packed planes, the FCC stacking sequence changes to ABCACBCAB and manifests itself as a twin in high-Mn steels. In the case of high-Mn TWIP/TRIP steels, twins and ε-martensite are the primary deformation products.

Various authors examined the effect of SFE on the deformation products and mechanisms to understand the relationship between these factors. Generally, it was found that with low SFE, ε-martensite was produced and as the SFE increased, twinning occurred followed by dislocation glide at higher SFE values (Rémy 1976, Rémy 1977, Wang 2010). SFE – composition maps were also created to match up SFE to the appropriate deformation product at a specific temperature for a given alloy.

Near room temperature, Rémy and Pineau (Rémy 1976) observed the various deformation structures as a function of the austenite composition as seen in Figure 2.2a with ε-martensite production occurring at a SFE of approximately 10-15 mJ/m^2 and

twinning at 20 mJ/m^2, with a region where both twinning and ε-martensite were observed. The effect of temperature was also determined for a specific alloy (Figure 2.2b), with increasing temperature favouring dislocation cells and lower temperatures favouring ε-martensite (Rémy 1977). As temperature decreases, the free energy of the austenite to ε-martensite transition decreases, and thereby decreases the SFE, making ε-martensite formation more favourable.

SFE composition maps were made by other authors specifically for the Fe-Mn-C system with the SFE mapped as a function of the alloy manganese and carbon content (Allain 2004b, Scott 2005, Nakano 2010) and super-imposed with thermal and mechanical ε-martensite phase boundaries. The trends of Figure 2.3, Figure 2.4 and Figure 2.5 are in agreement in that with increasing SFE, dislocation glide is favourable versus twinning and ε-martensite production. At lower SFE, production of ε-martensite is more favourable over twinning and dislocation glide. It was also observed that by decreasing the content of one alloying element, the SFE decreases, but with decreasing the composition of one element while increasing another, the SFE remains constant. The compositional effect on the SFE and deformation products may not be as simple as the maps portray with various compositions having similar SFE, yet specific compositional break down and alloying element interaction was not considered.

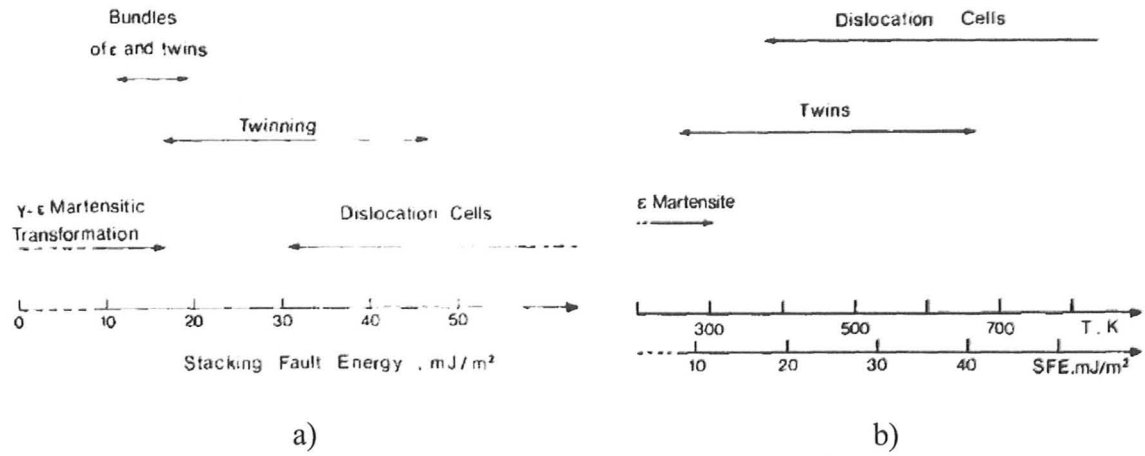

Figure 2.2 Deformation Structures as a Function of SFE a) at Room Temperature (Rémy 1976) b) as a Function of Temperature (Rémy 1977)

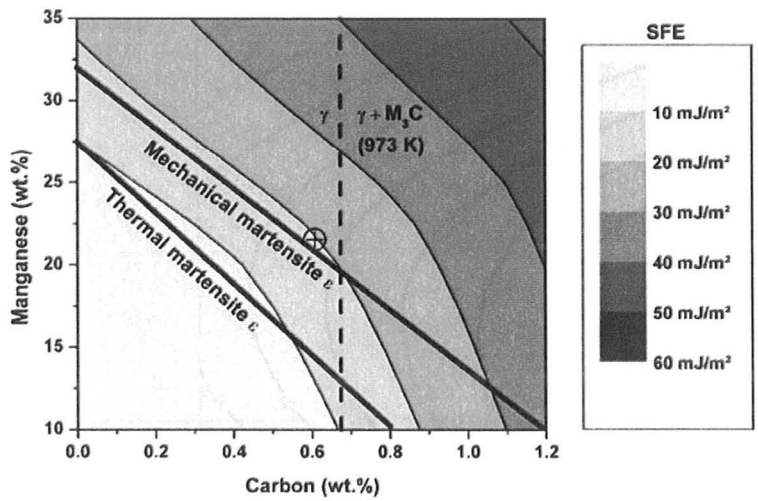

Figure 2.3 SFE Map Based on Carbon/Manganese (wt%) with ε-Martensite Limits (Allain 2004b)

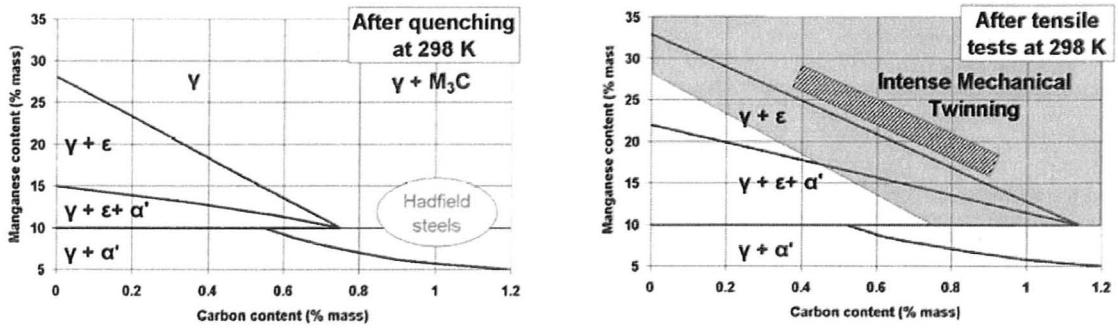

a) b)

Figure 2.4 Fe-Mn-C Phase Stability Diagram at 298K a) After Quenching b) After Tensile Testing (Scott 2005)

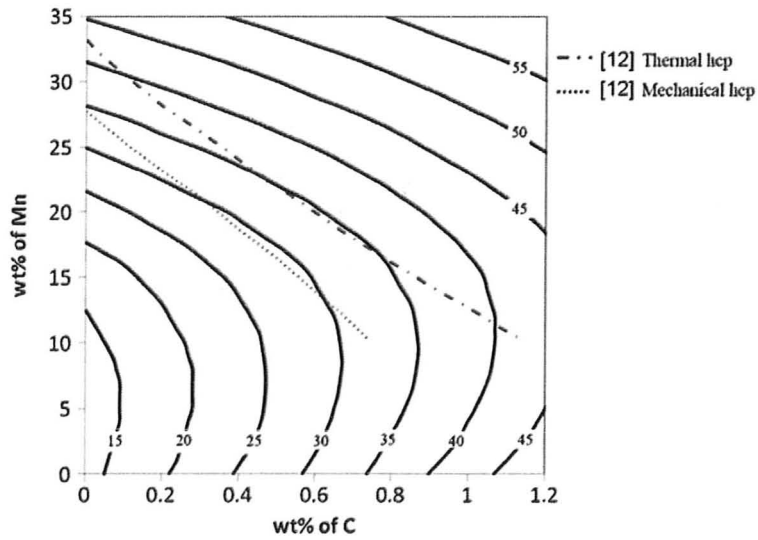

Figure 2.5 SFE Map with ε-Martensite Boundaries (Nakano 2010)

2.1.2. Twin Formation

The formation of a twin boundary causes a disruption in the stacking sequence and shears the lattice as a mirror image of itself. Within the high-Mn austenite matrix, the stacking sequence changes from ABCABC to ABCBAC with a twin formed on the K_1 composition plane. The changed stacking sequence is visualized in Figure 2.6a with a

mirror image about the line PQ and the crystal structure before and after twinning seen in Figure 2.6b with the atoms being sheared to the left (Kelly 1970). If Shockley partial dislocations moved on every {111} plane (similar to inserting a crystal plane), an extrinsic stacking fault is observed, leading to a twin stacking sequence (Olson 1976a). As the twin formation changes the crystallography and not the chemical composition of the structure, twinning is not a diffusion-driven phase transformation. In the case of high-Mn TWIP steels, the creation of twins is often regarded as a type of phase transformation with the twins and parent matrix both being austenite.

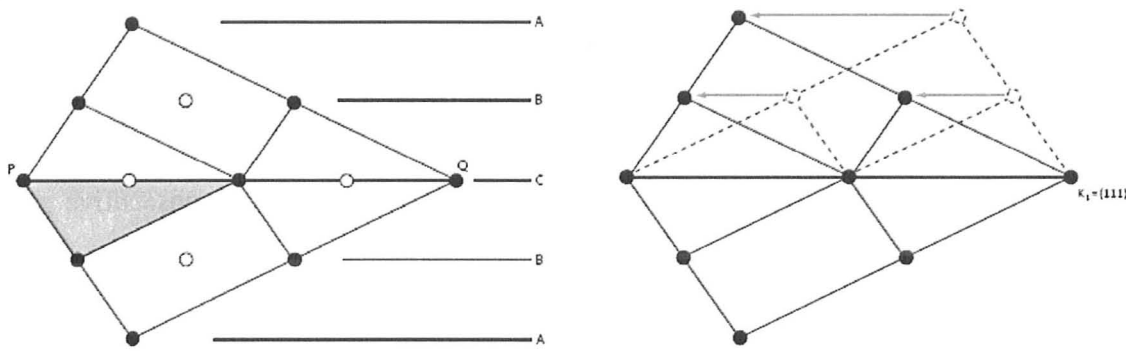

a) b)

Figure 2.6 Twin Nucleation a) Stacking Sequence b) Crystal Structure Before and After Twinning (Kelly 1970)

One model for twin nucleation focuses on the movement of partial dislocations. As a twin is defined within a matrix with a twin-matrix interface, a shape change imposes an elastic strain field on this interface (Figure 2.7a), with dislocations representing the strain field (Figure 2.7b). When the twin is sufficiently thin, the stress experienced can be represented by a dislocation pile-up as seen in Figure 2.7c (Kelly 1970).

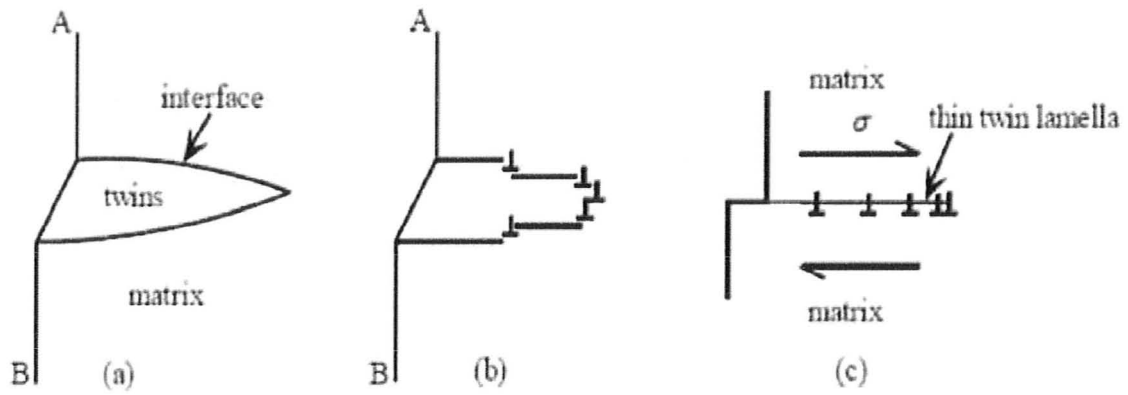

Figure 2.7 Twin Nucleation Dislocation Model a) Twin-Matrix Interface b) Dislocation Representing Strain Field c) Thin Twin Dislocation Model (Kelly 1970)

Another model for twin nucleation is the pole mechanism model where a fault embryo is extended in the fault plane and intersects with forest dislocations. If the forest dislocations contain a Burgers vector normal to the fault plane and the dislocations are strongly pinned, it may act as a pole for dislocations movement on consecutive planes (Olson 1976b, Kelly 1970, Idrissi 2010).

2.1.3. ε-Martensite Formation

ε-Martensite is created from the parent austenite phase with a diffusionless transformation. This phase transformation in high-Mn steels changes the crystallography from FCC-austenite to HCP-ε-martensite with the chemical composition remaining unchanged. Partial dislocations move on every other close packed plane, which is equal to removing a plane, leading to an intrinsic stacking fault with the HCP-ε-martensite stacking sequence as shown in Figure 2.8 (Olson 1976a, Olson 1976b, Bracke 2006).

Mechanical or strain-induced ε-martensite was found to grow by one type of Shockley partial dislocation multiplication on the close-packed plane. High resolution

electron microscopy analysis on the structure of ε-martensite in Figure 2.9 revealed an ε-martensite plate to contain thin platelets of ε-martensite within layers of austenite. The ε-martensite plates appear to be separated by thin layers of austenite (Putaux 1996).

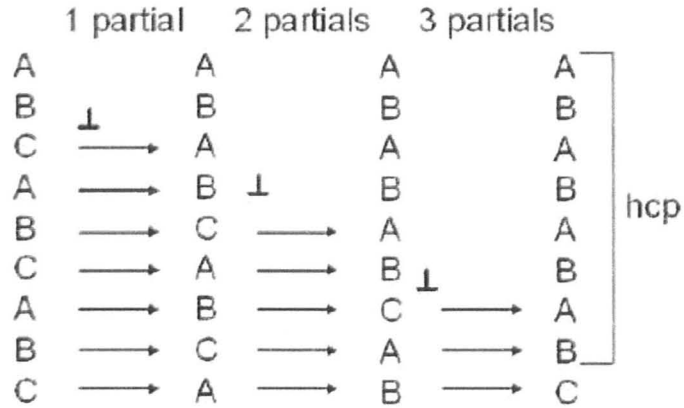

Figure 2.8 Stacking Sequence in HCP ε-Martensite Nucleation (Bracke 2006)

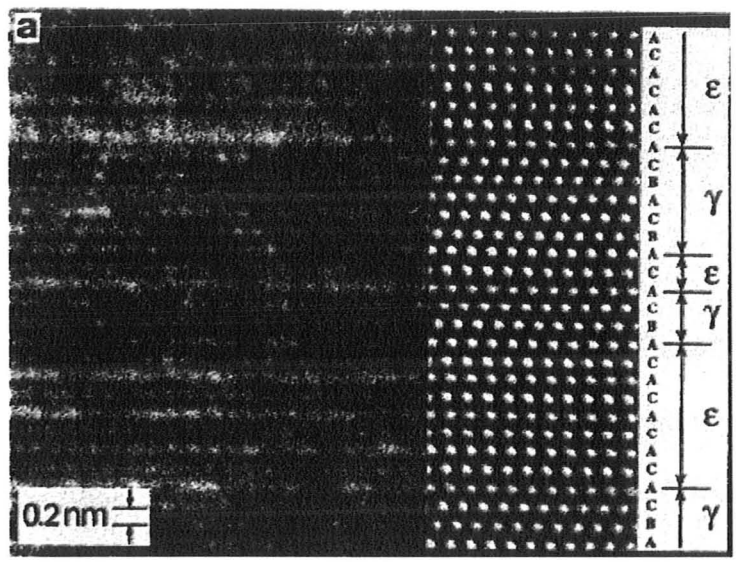

Figure 2.9 HREM of Layered Structure of ε-Martensite with Processed Imaged Inset on Right Assuming Atoms are White (Putaux 1996)

2.2 Work Hardening

The work hardening in FCC alloys is generally considered to derive from isotropic and kinematic hardening contributions. The isotropic strain hardening considers the work hardening behaviour where upon the mechanical behaviour is strain path independent, whereas kinematic hardening is strain path dependent. The effect of strain-induced deformation products (twins or ε-martensite) on work hardening is usually manifested in the kinematic hardening contribution by taking into account the effect of internal stresses developing in the matrix arising from the deformation products. With the various contributions to work hardening, the overall flow stress, σ_{total}, is a combination of the initial yield strength σ_{yield}, isotropic hardening $\sigma_{isotropic}$ and kinematic hardening $\sigma_{kinematic}$ per Equation 2.3 (Bate 1986). A detailed examination of isotropic and kinematic hardening is performed to discuss the factors involving the work hardening and measurement methods.

$$\sigma_{total} = \sigma_{yield} + \sigma_{isotropic} + \sigma_{kinematic} \tag{2.3}$$

2.2.1. Isotropic Strain Hardening

Isotropic strain hardening is the non-directional contribution from dislocation storage processes and Kocks and Mecking (Kocks 2003) have provided a detailed analysis of strain hardening in FCC alloys considering only isotropic hardening. With different stages of isotropic hardening defined, the Kocks - Mecking model mainly addresses stage III hardening, which is strongly dependant on the material and the SFE. The model suggests that the main hardening mechanism is the combination of two

processes, dislocation accumulation and dislocation annihilation (also known as dynamic recovery). Dislocation accumulation is the process where mobile dislocations are stored or accumulate within the material during deformation, adding to the overall strain hardening by impeding the movement of other dislocations. Dislocation annihilation describes the rearrangement of these mobile dislocations during deformation in a matter which increases the mobility of glissile dislocation, thereby detracting from strain hardening. The net strain hardening is then a combination of the dislocation accumulation and storage minus the effect of dislocation annihilation (Kocks 2003).

The Voce law has also been used to describe work hardening in relation to the overall flow stress as seen in Equation 2.4, where θ is the work hardening rate ($\theta=d\sigma/d\varepsilon$), σ the flow stress, σ_v the scaling stress and θ_0 a constant that describes the maximum rate of work hardening. The effect of increasing temperature and strain rate on the Voce law can be seen in Figure 2.10 (Kocks 2003). By partial differentiation, the Voce law can be rearranged in the form of the flow stress and used to model the mechanical behaviour described in later chapters.

$$\boldsymbol{\theta = \theta_0\left(1-\frac{\sigma}{\sigma_v}\right)} \tag{2.4}$$

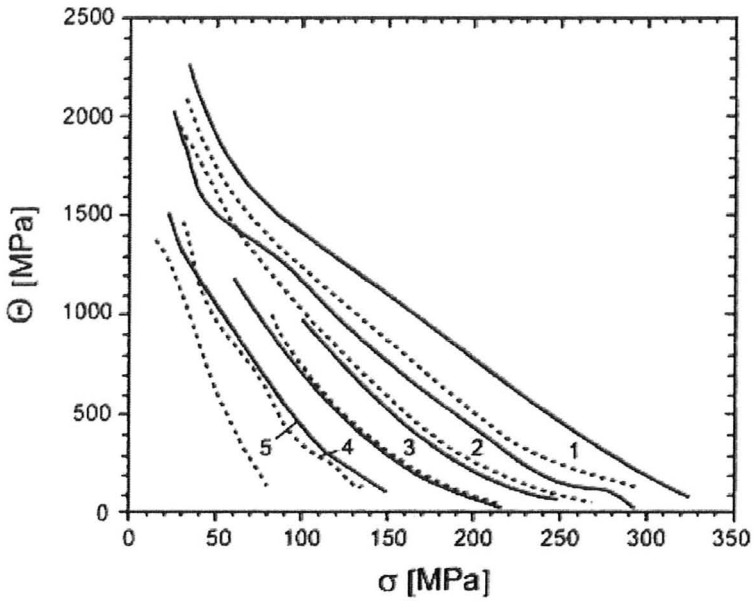

Figure 2.10 Effect of Temperature and Strain Rate for 1) RT 2) 100°C 3) 200°C 4) 300°C 5) 400°C and 1 s^{-1} Solid Line & 10e-4 s^{-1} Dashed Line in Cu-Polycrystals (Kocks 2003)

2.2.2. Kinematic Strain Hardening

The work hardening contribution related to the development of internal stresses is known as the kinematic strain hardening or Bauschinger effect. Internal stresses can often arise from deformation products or by hard particles in a soft matrix, similar to what is observed for strain-induced transformation products. With the presence of different phases, internal stresses arise from forward and reverse plastic flow and develop due to the incompatibility between parent and new phases and are often referred to as back stresses. Back stresses are commonly observed when changing the strain path from tension to compression, with a permanent softening observed versus the tensile or forward stress compared to the compression flow stress. A typical Bauschinger test is performed on cylindrical samples with forward or tensile loading followed by unloading

and reverse or compressive loading of the samples. The permanent softening and rounding of the reverse flow curve reflected into the tensile domain can be seen in Figure 2.11 (Sowerby 1979). In this case, the permanent softening or so-called Bauschinger effect is a measure of the kinematic hardening contribution to the overall flow stress.

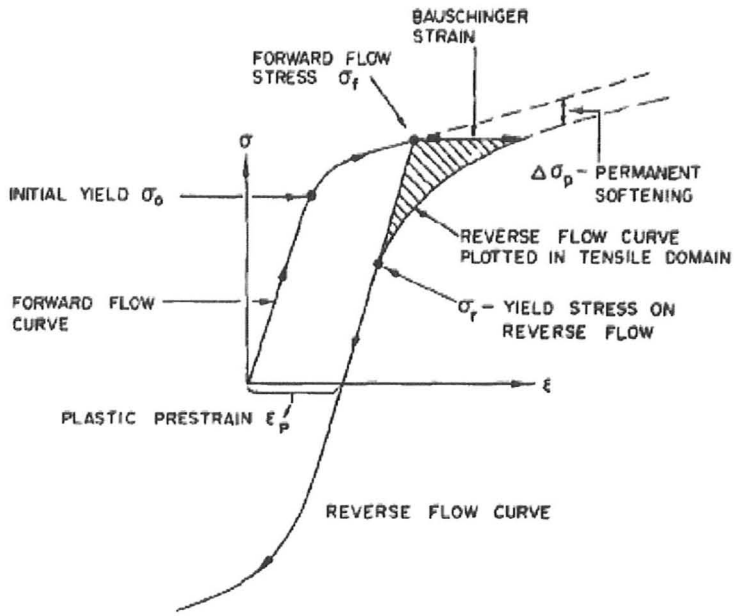

Figure 2.11 Typical Bauschinger Effect during Forward and Reverse Flow Test (Sowerby 1979)

With respect to transformable alloys and the strain-induced deformation products that arise in high-Mn steels, the kinematic hardening contribution accounts for a significant portion of the overall flow stress. The evolution of back stress as a function of strain was studied by Bouaziz et al. (Bouaziz 2008) for a Fe-22Mn-0.6C alloy and the kinematic hardening was seen to contribute up to half of the total flow stress (Figure 2.12). Strain-induced deformation products (twins and/or ε-martensite) were considered as boundaries for dislocation motion and added significantly to the kinematic hardening

due to their ability to continuously introduce new barriers and back stresses. Single crystal Hadfield steels were also examined for the effect of twinning and slip on the Bauschinger effect and twinning was found to have a larger Bauschinger effect compared to slip deformation (Karaman 2001).

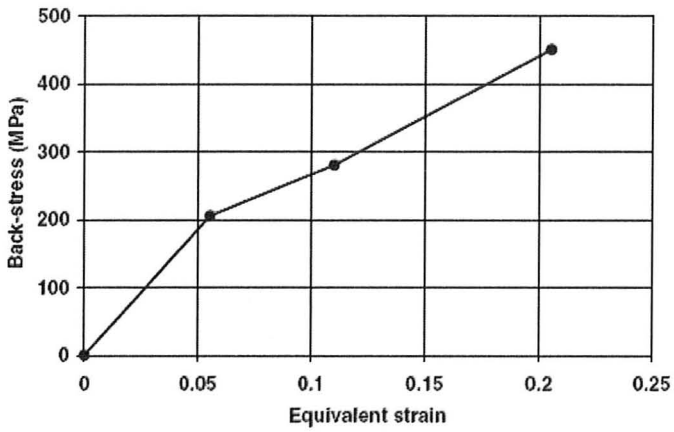

Figure 2.12 Back Stress Development as a Function of Strain (Bouaziz 2008)

2.3 TWIP Steels

One particular type of transformable steels are TWIP steels where twinning induced plasticity strengthens the alloy. Twin boundaries are created continuously within the microstructure to subdivide grains with twin boundaries acting as barriers for dislocation motion. The twins decrease the mean free path for dislocation movement by "refining" grain size per Figure 2.13. Grains are continually divided by mechanical twins during deformation and this is often referred to as the dynamic Hall-Petch effect and contributes to high strengths and ductilities. As the twins are being created upon straining, the Hall-Petch effect is not static but dynamic until twins are no longer produced (i.e. saturation). Numerous authors have discussed the TWIP effect specifically

within the Fe-Mn-C system with many advances being made in recent years (Rémy 1977, Grassel 2000, Karaman 2000a, 2000b, 2001, Bouaziz 2001, 2007, 2008, 2009, Frommeyer 2003, Allain 2004a, 2004b, 2004c, Scott 2005, Chen 2007, Liang 2009, De Cooman 2009, Gutierrez-Urrutia 2010, Idrissi 2009, 2010, Wang 2010) while others have discussed the effect of twinning on plasticity in other alloy compositions (Rémy 1976, 1981, Dastur 1981, Olson 1976a). The Fe-Mn-C system is of specific interest due to some alloys yielding tensile strengths of approximately 1200 MPa and large elongations to fracture ~70% (Allain 2004b).

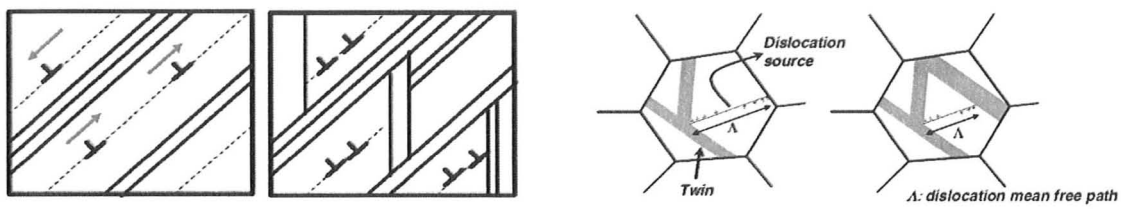

a) b)

Figure 2.13 Illustration of TWIP effect by a) Bouaziz and Embury (Bouaziz 2007) b) De Cooman et al. (DeCooman 2009)

2.4 TRIP Steels

TRIP steels are another type of transformable steels, where the strain-induced transformation induces plasticity and aids the overall strengthening. Within austenitic FCC alloys, and specifically the Fe-Mn-C system, austenite is transformed into ε-martensite during straining for the TRIP effect. Similar to the TWIP effect, the introduced ε-martensite phase acts as a barrier for dislocation motion and the new phase decreases the dislocation mean free path. It also introduces a large number of dislocations into the structure that contribute to the hardening. Another possible

transformed phase within the austenitic Fe-Mn-C system is the magnetic α′-martensite which is associated with low values of alloy SFE and will not be discussed at this time. Authors discussing the TRIP effect include Olson 1976a, 1976b, Rémy 1977, Frommeyer 2003, Grässel 2000, Liang 2008, 2009, Wang 2010, Bracke 2006, Lü 2010, Nagy 2004 and Bian 2009, with some specifically addressing the Fe-Mn-C system, while others discuss different alloy compositions. The TRIP effect is generally seen to provide a short term increase in work hardening rate which decreases quickly leading to early fracture, while the TWIP effect generally provides sustained high work hardening rates and allows for high elongations as shown in Figure 2.14. Depending on exact alloy compositions and the dominance of either the TWIP and TRIP effect, various strengths and ductilities were achieved.

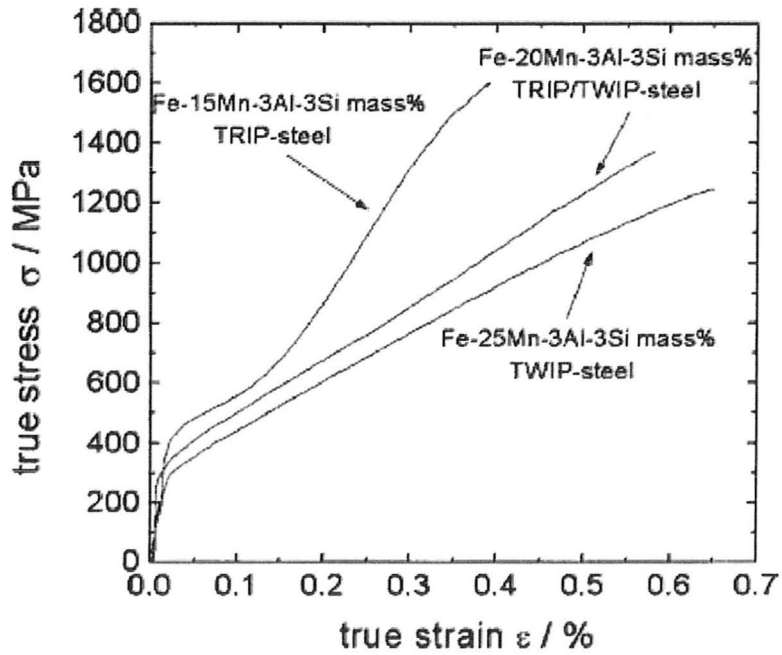

Figure 2.14 Comparison of True Stress – Strain for TRIP and TWIP Steels (Frommeyer 2003)

2.5 High Mn TWIP/TRIP Alloys

Some specific compositions of high-Mn TWIP / TRIP alloys are discussed in the section below to comment on work already done by other authors. The alloys discussed include Fe-30Mn, Fe-24Mn TRIP, Fe-22Mn-0.6C TWIP and Fe-22Mn-0.376C TWIP / TRIP.

2.5.1. Fe-30Mn Steel

This alloy displayed a fully austenitic as-annealed microstructure, seen by the EBSD phase map in Figure 2.15 with yellow indicating austenite and green as unindexable areas. The alloy had a SFE of 34.1 mJ/m^2 and deformed primarily by dislocation glide with mechanical twinning only observed near fracture, at around 0.30 true strain. TEM analysis of the unstrained and ε_t=0.20 microstructure (Figure 2.16) revealed equiaxed austenite grains with a well-developed dislocation cell structure and dense dislocation walls, respectively. The Fe-30Mn was of particular interest due to the lack of twinning prior to 0.30 true strain (Liang 2008), making the alloy an ideal example for an austenitic high-Mn alloy with no twinning. The alloy was used for comparison on the effect of twinning, ε-martensite and carbon content and was used by Bouaziz et al (Bouaziz 2009) to model the mechanical behaviour of an austenitic high-Mn alloy.

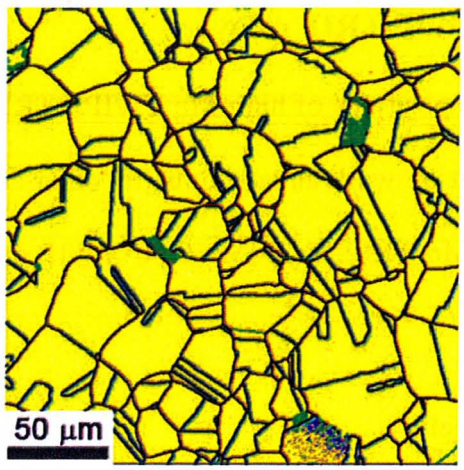

Figure 2.15 EBSD Phase Map of Fe-30Mn Annealed Microstructure (Liang 2008)

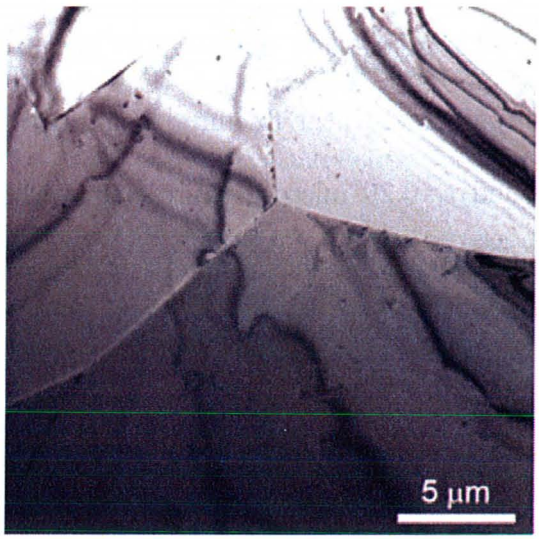

a) BF Image at ε_t=0.0

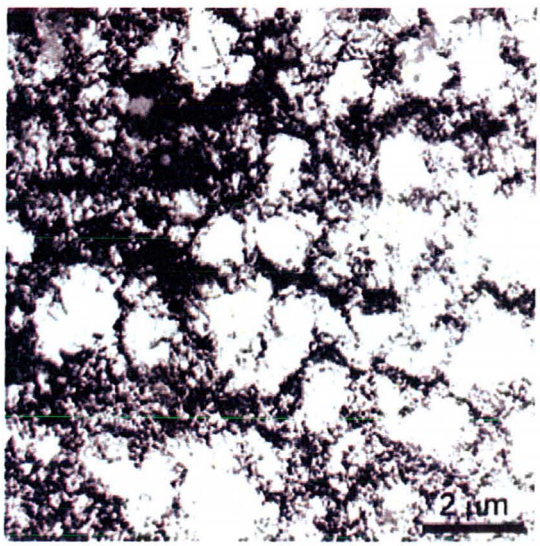

b) BF Image at ε_t=0.20

Figure 2.16 TEM Images of a) Annealed Microstructure and b) Well-Developed Cell Structures in Fe-30Mn Alloy (Liang 2008)

2.5.2. Fe-24Mn TRIP Steel

Fe-24Mn with no carbon was also analyzed by Liang (Liang 2008) via SEM micrographs, EBSD phase maps and TEM analysis. The lower manganese content as

compared to the Fe-30Mn, lowered the SFE to 27.9 mJ/m^2 and shifted the microstructure and deformation mechanism. A dual-phase microstructure was observed (Figure 2.17a) in the as-annealed condition with the EBSD phase map (Figure 2.17b) showing austenite grains (yellow) and ε-martensite plates (red).

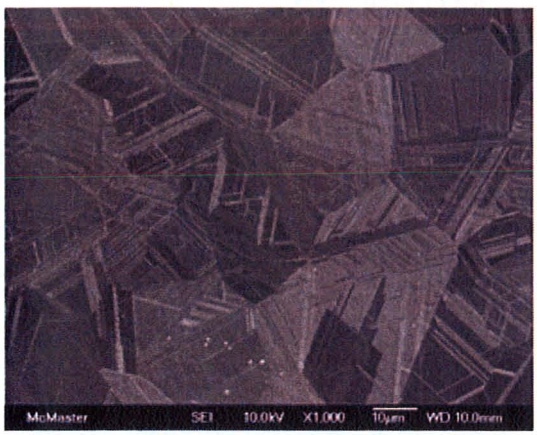

a) ε_t=0.0

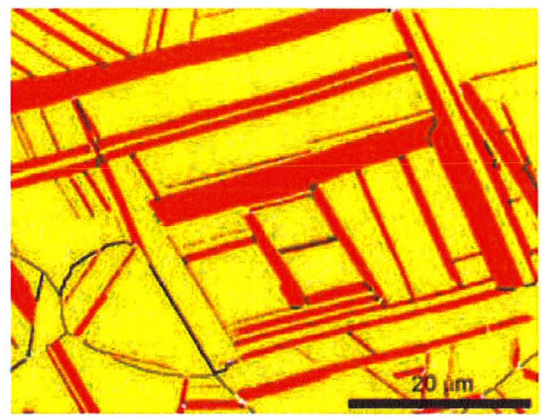

b) EBSD phase map at ε_t=0.0

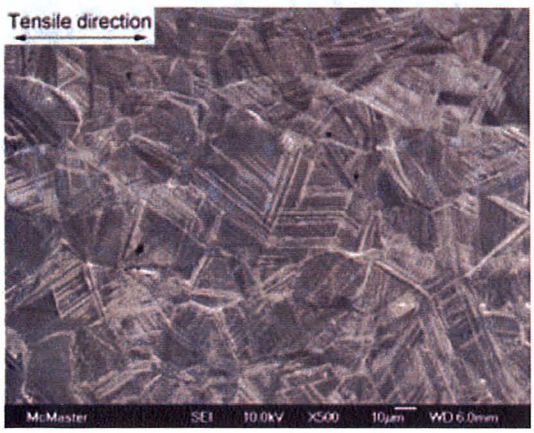

c) ε_t=0.05

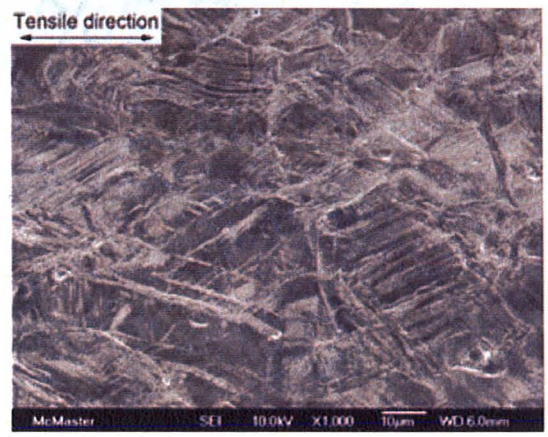

d) ε_t=0.30 (fracture)

Figure 2.17 Microstructural Evolution as a Function of Strain for Fe-24Mn (Liang 2008)

During deformation, production of ε-martensite increased until fracture seen by micrographs (Figure 2.17c-d) at various strain levels. TEM BF and DF images (Figure

2.18) of the microstructure revealed ε-martensite plates finely dispersed within austenite grains. The evolution of ε-martensite production as a function of applied strain in Figure 2.19 was compared for Fe-24Mn and Fe-30Mn with Fe-24Mn showing a significant increase in ε-martensite during straining. The Fe-30Mn alloy produced virtually no ε-martensite at low strain levels with ~10% at fracture (Liang 2008).

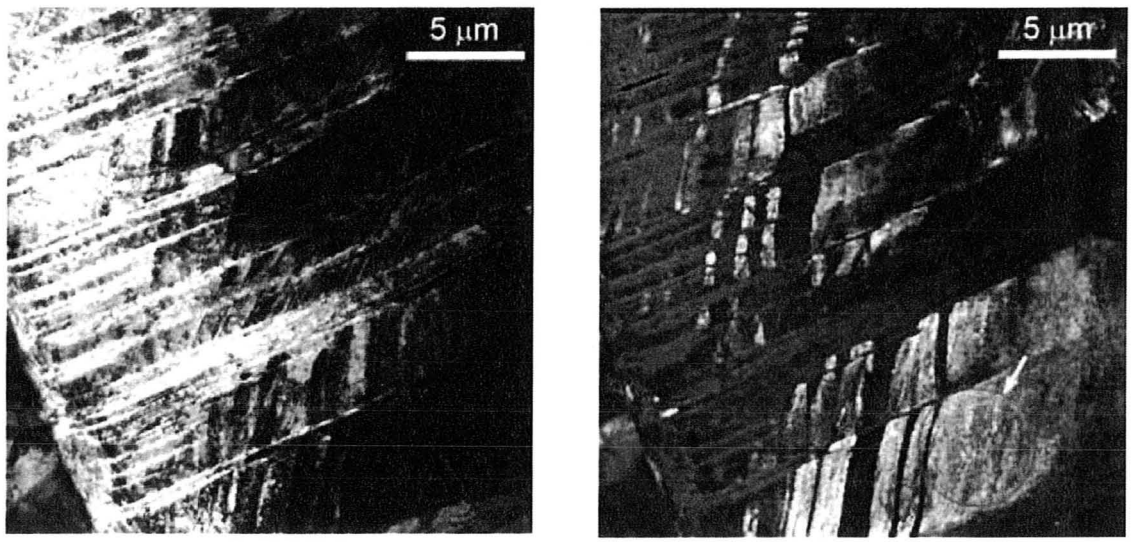

a) BF Image of ε-Martensite Plates b) DF Image of One ε-Martensite Plate

Figure 2.18 TEM Images of Fe-24Mn Alloy Microstructure at ε_t=0.20 (Liang 2008)

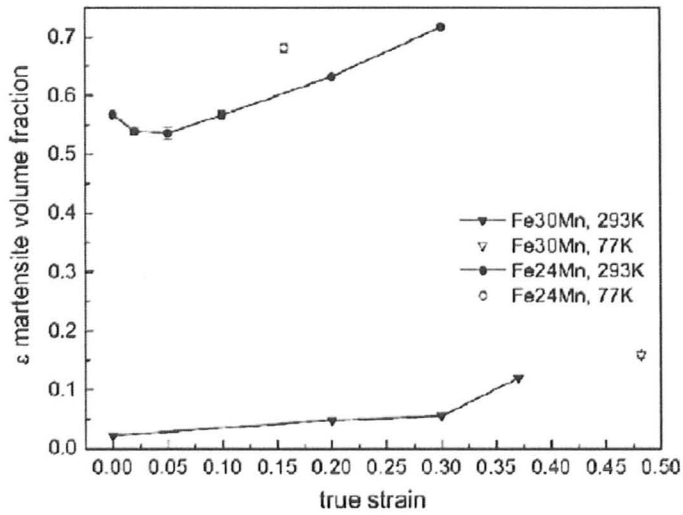

Figure 2.19 XRD ε-Martensite Phase Analysis for Fe-30Mn and Fe-24Mn (Liang 2008)

2.5.3. Fe-22Mn-0.6C TWIP Steel

Previous work has already been presented on the Fe-22Mn-0.6C TWIP steel (Bouaziz 2001, 2007, 2008, Allain 2004a 2004b 2004c, Scott 2005, Barbier 2008, Gutierrez-Urrutia 2010), containing discussion on both microstructural evolution and mechanical properties. The microstructural evolution of a Fe-22Mn-0.6C steel was observed with optical micrographs at various strain levels (Figure 2.20) revealing twins and grain boundaries (Allain 2004c). The unstrained microstructure revealed annealing twins with no visible deformation and mechanical twinning initiating from 0.18 until 0.34 true strain. Twins were activated within grains, blocked by grain boundaries and increased with strain (Allain 2004c).

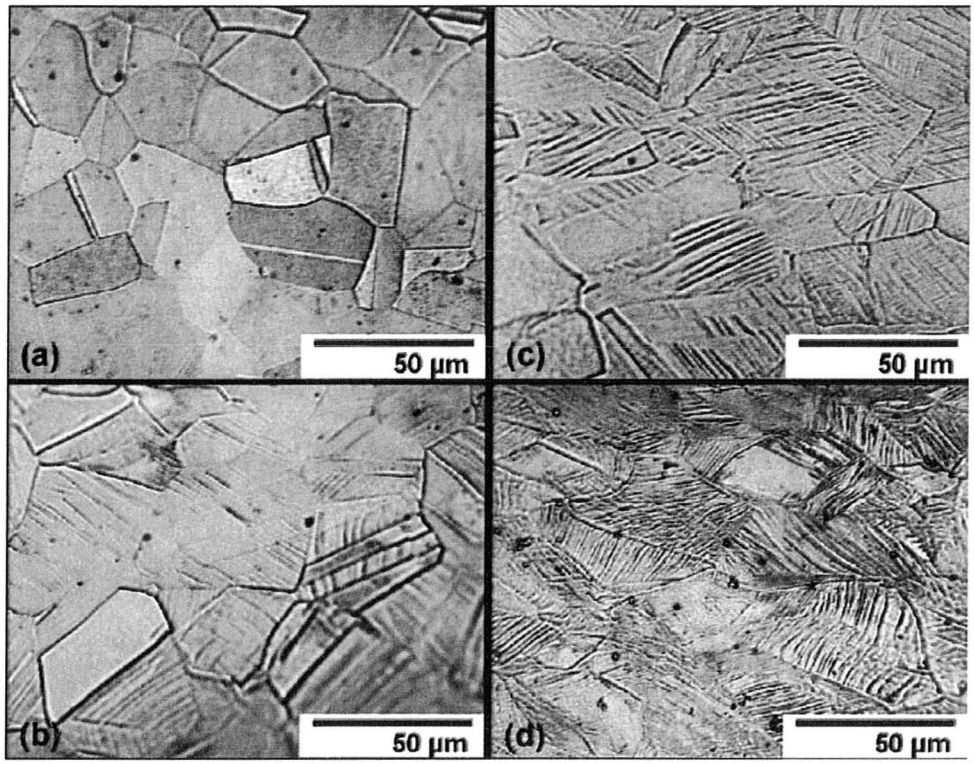

Figure 2.20 OM Revealing Grain Boundaries and Twins with Horizontal Tensile Direction at Various Strain Levels a) 0.0 b) 0.18 c) 0.26 d)0.34 (Allain 2004c)

The effect of temperature on the Fe-22Mn-0.6C alloy deformation microstructure was examined by Allain et al. and found to mainly depend on the SFE (Allain 2004b). As the temperature changed, the system thermodynamics were altered and the SFE changed, making different deformation products possible. As temperature decreased, the SFE was reduced resulting in the deformation mechanism shifting from dislocation glide and twinning to ε-martensite transformation (Allain 2004b).

The grain size dependence on mechanical properties was also examined for a Fe-22Mn-0.6C alloy where it was found that increasing grain size decreased the yield strength, as seen in Figure 2.21a. The slope of the true stress-strain curve remained

relatively constant with decreasing grain size. The smaller grained samples had a higher yield strength as described by the Hall-Petch equation, where the yield strength was inversely proportional to the root of the grain diameter (Equation 2.4) (Bouaziz 2008).

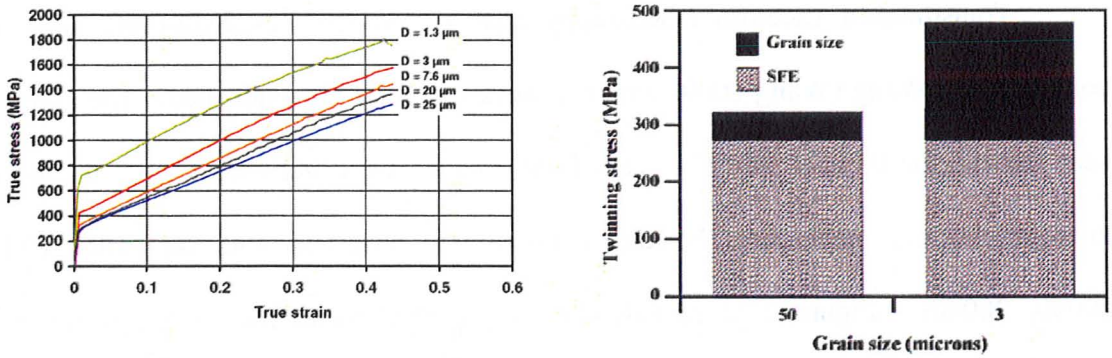

a) b)

Figure 2.21 Effect of Grain Size on a) Tensile Behaviour (Bouaziz 2008) b) Twinning Stress (Gutierrez-Urrutia 2010)

$$\sigma_Y = \sigma_0 + \frac{k}{\sqrt{d}} \tag{2.4}$$

An observation of Gutierrez-Urrutia et al. (Gutierrez-Urrutia 2010) was that grain refinement does not suppress deformation twinning or the TWIP effect. As grain size decreased to 3 µm, deformation transformation became more difficult but was not completely suppressed. Considering both SFE and grain size, and the effect on twinning (twinning stress), the smaller grain size had a higher twinning stress compared to the larger grain size samples (Figure 2.21b). The SFE contribution to the twinning stress was larger than their grain size factor to the twinning stress. Large grain sizes had a significantly smaller grain size contribution to the overall twinning stress and smaller

grain sizes had a twinning stress contribution similar to the SFE contribution (Gutierrez-Urrutia 2010).

2.5.3.1. TEM Analysis

Transmission Electron Microscopy analysis on the Fe-22Mn-0.6C alloy was conducted by Wang (Wang 2009) with the work currently not published. The alloy was heat treated for 0.5h at 950°C. The TEM images were consistent with the optical micrographs and mechanical behaviour previously observed with this alloy (Allain 2004b, 2004c). Figure 2.22 reveals the as-quenched austenitic microstructure with equiaxed grains. At 0.20 true strain, Figure 2.23 displays BF and DF images of the dislocation structure and mechanical twins. The BF images revealed dense cell dislocation structures developing with fine twins while the DF image highlights the fine twins within the structure. Cold rolling the alloy to 70% revealed a dense dislocation structure with two sets of twins activated, as seen in Figure 2.24. The DF images of the twin systems revealed a set of twins in one direction and another set of twins in another direction. The twinning observed by TEM analysis confirmed the mechanical behaviour and microstructural evolution contributing to the high strength and ductility in the Fe-22Mn-0.6C alloy.

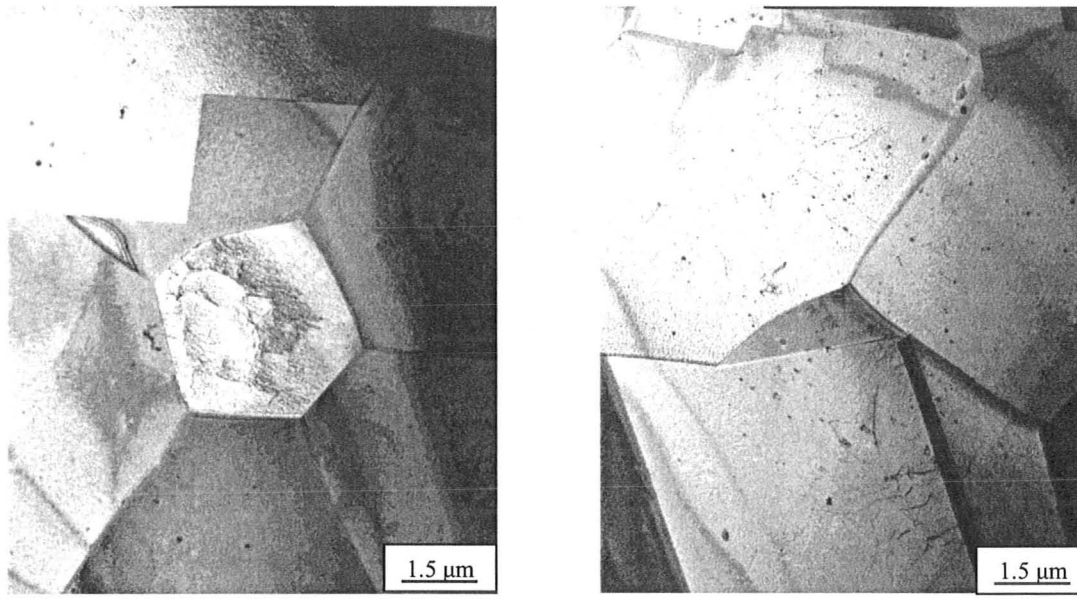

Figure 2.22 TEM Images of As-quenched Structure in Fe-22Mn-0.6C Alloy (Wang 2009)

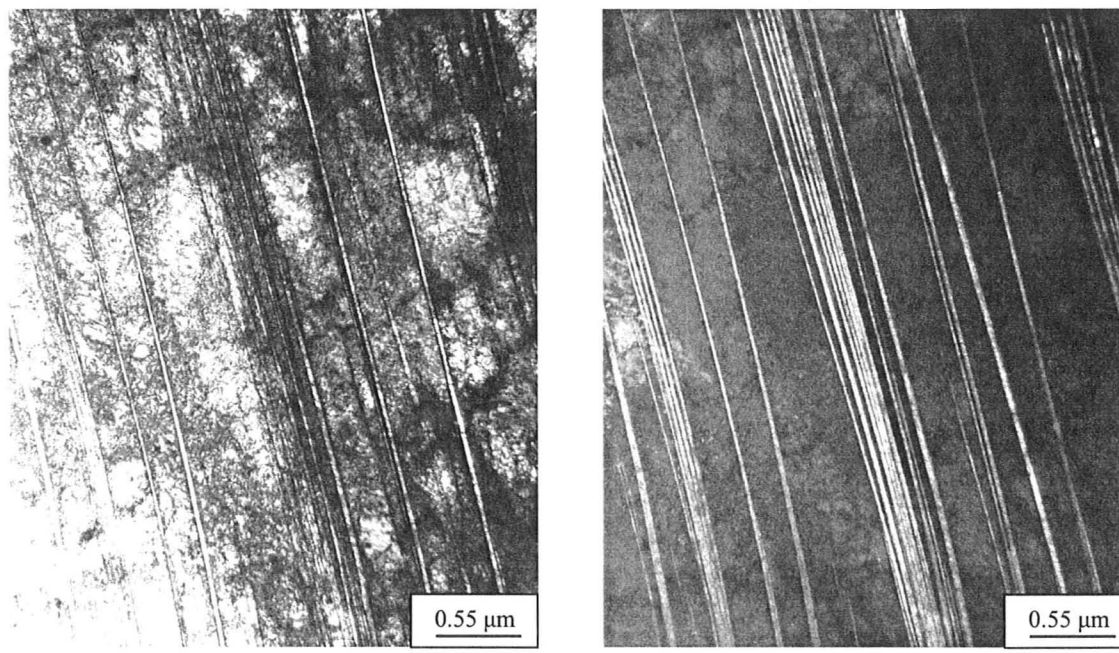

a) BF Image of Dislocation Structure b) DF Image of Twins

Figure 2.23 TEM Images of Microstructure in Fe-22Mn-0.6C Alloy at ε_t=0.20 (Wang 2009)

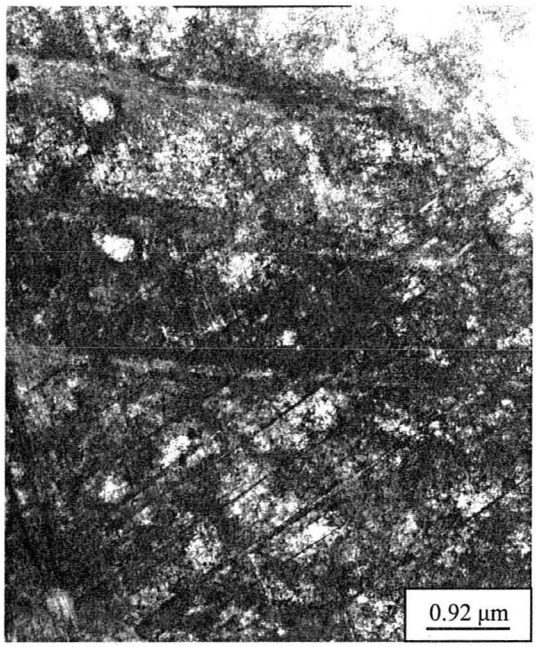

a) BF Image of 2 Sets of Twins, Deformation Bands and Dislocation Structure

b) DF Image of Twins (1 set)

c) DF Image of Twins (2nd set)

Figure 2.24 TEM Images of Microstructure in Fe-22Mn-0.6C Alloy Cold Rolled to 70% (Wang 2009)

2.5.4. Fe-22Mn-0.376C TWIP / TRIP Steel

An alloy studied by Lü et al. (Lü 2010) was Fe-22Mn-0.376C with a SFE of 32.6 mJ/m^2. The alloy deformed via dislocation slip, mechanical twinning and production of ε-martensite during deformation, with EBSD phase maps in Figure 2.25 displaying an austenite matrix, ε-martensite in blue and twin boundaries in red, as a function of applied strain. Both TWIP and TRIP effect were present in this alloy with a large amount of ε-martensite being produced at a strain of 0.51 (Lü 2010). The two effects made the alloy an interest of study with more factors contributing to work hardening (dislocation slip, twin formation and ε-martensite production).

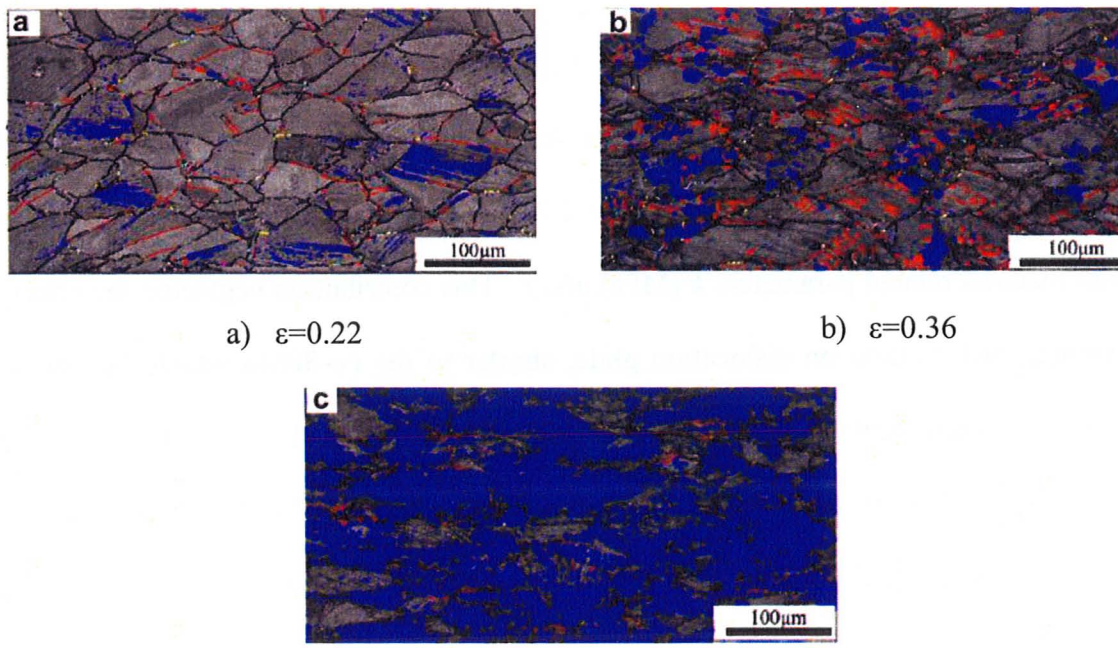

a) ε=0.22 b) ε=0.36

c) ε=0.51

Figure 2.25 EBSD Images of Fe-22Mn-0.376C Cold Rolled Samples at Various Strains (Lü 2010)

2.6 TWIP Model and the Effect of Chemical Composition

Bouaziz et al. (Bouaziz 2009) developed a semi-phenomenological model for the mechanical behaviour of TWIP alloys, looking at the different contributions that lead to high rates of work hardening in the high-Mn alloys. The overall flow stress was modeled with three contributions to the overall strength as seen in Equation 2.6. The yield stress (YS) proposed in the model followed Equation 2.7 with *C* and *Mn* in weight percents.

$$\sigma = YS + \sigma_1 + \sigma_2 \tag{2.6}$$

$$YS\ (MPa) = 228 + 187C - 2Mn \tag{2.7}$$

The first stress contribution (σ_1) was the flow stress of a fully austenitic matrix without the TWIP effect (only isotropic hardening) and is seen in Equation 2.8 to take the form of the Voce law discussed in Section 2.2.1. The variable ε represents the true strain with material related parameters *k* (MPa) and *f*. This contribution neglected the effect of twinning and focused on dislocation glide, similar to the Fe-30Mn which did not twin until very high strains. The second stress contribution (σ_2) reflected the dynamic composite effect of back stress development due to the TWIP effect (kinematic hardening) as seen in Equation 2.9, with *m* and *p* being dimensionless materials related parameters. The variable *m* was a function of the carbon and manganese content, displayed in Equation 2.10 with the parameter *z* defined in Equation 2.11. The model fit values of k = 2900 MPa, f = 4, and p = 1.75 with m being dependent on carbon and manganese contents (Bouaziz 2009).

$$\sigma_1 = k\left[\frac{1-\exp(-f\varepsilon)}{f}\right] \tag{2.8}$$

$$\sigma_2 = m\varepsilon^p \tag{2.9}$$

$$m = 60661z - 261874z^2 \tag{2.10}$$

$$z = \frac{C}{Mn-5} \tag{2.11}$$

Various high-Mn TWIP steels were examined and their experimental tensile behaviour modeled, as seen in Figure 2.26a, with all alloys deforming by twinning except for Fe-30Mn which was used as a reference for σ_1. The modeled and experimental comparison (Figure 2.26b) was seen to agree, with the experimental flow stress agreeing with the modeled data. The model stated that the chemical composition had a large effect on the tensile behaviour due to the TWIP effect (Bouaziz 2009). The serrations observed in Figure 2.26a were not considered in the model, as well as the effect of ε-martensite.

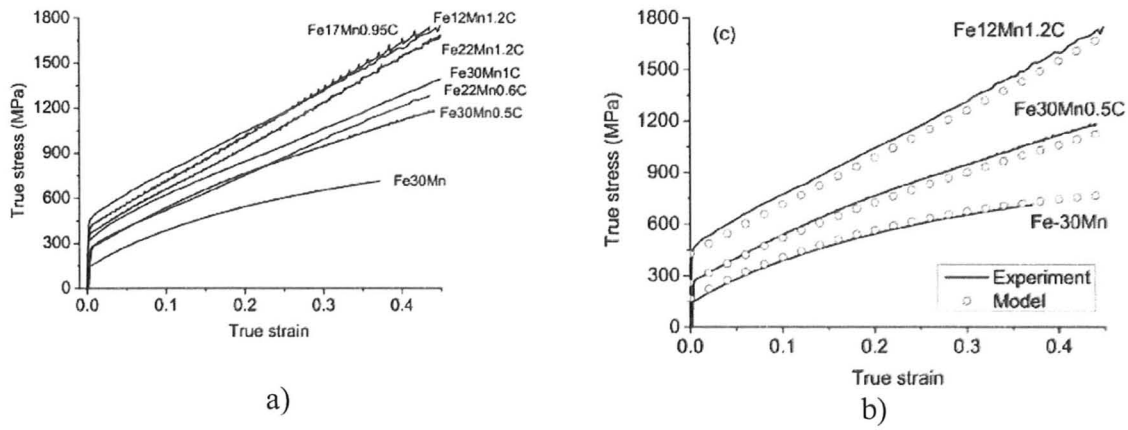

a) b)

Figure 2.26 Tensile Curves of Various TWIP Steels of a) Experimental Curves of Various Compositions b) Modeled and Experimental Comparison (Bouaziz 2009)

2.7 Iso-Work Model

Another model was developed by Bouaziz and Buessler (Bouaziz 2004) to consider the effect of another phase (i.e. ε-martensite) with the previous TWIP model not applicable to alloys displaying the TRIP effect. The iso-work model assumes that the incremental mechanical work is equal in all phases during deformation, as seen in Equation 2.12. This equates the work within the austenite to the work within the ε-martensite and the overall flow stress was modeled with these conditions (Bouaziz 2004). The Hollomon plastic law for stress was used in addition to the iso-work condition. This iso-work model was applied to Fe-24Mn by Liang (Liang 2008) to describe the mechanical properties of this alloy. The distribution of global and local stresses and strains were also analyzed by Liang (Liang 2008).

$$\sigma_\gamma d\varepsilon_\gamma = \sigma_\varepsilon d\varepsilon_\varepsilon \tag{2.12}$$

3. OBJECTIVES

The demand for stronger and safer automotive materials drives this current work to investigate the methods of achieving sustained rates of high work hardening in high-Mn TWIP / TRIP steels. Three alloys of Fe-22Mn-C are examined with 0.6 wt% carbon (0.6C), 0.4 wt% carbon (0.4C) and 0.2 wt% carbon (0.2C). By decreasing the carbon content, the SFE should decrease and the deformation mode shifted from TWIP to TRIP. The aim of this thesis is to examine and understand the microstructural evolution and mechanical properties of three Fe-22Mn-C steels with varying carbon content, after annealing and during deformation. Specifically, the following is examined:

1) The as-annealed microstructures for the initial phases.
2) The mechanical behaviour during deformation with ultimate tensile strength, uniform elongation, and yield strength.
3) Work hardening rates and kinematic hardening contributions.
4) Microstructural evolution during deformation with strain-induced phase transformations (twins, ε-martensite)
5) Phase characterization of ε-martensite produced during deformation.
6) Damage mechanisms involved in the fracture of the alloys.
7) Modeling the mechanical behaviour of the TWIP / TRIP alloys.
8) The effect of carbon content on the microstructural evolution and mechanical properties of TWIP/ TRIP alloys.

4. EXPERIMENTAL METHOD

This chapter will discuss the experimental set-up and testing conditions applied in the various experiments. The thermal and mechanical testing methods, chemical preparation, and materials characterization techniques will be addressed. Due to the sensitive nature of the experimental steel to strain induced transformation, close attention was paid to sample preparation in order to produce repeatable results.

4.1 Starting Material

The as-received Fe-22Mn-0.6C sheet steel was provided by ArcelorMittal Global Research in Metz, France. The cold-rolled steel was water-jet cut and analyzed using Glow Discharge Optical Emission Spectrometry (GDOES) for compositional analysis of all elements except carbon and sulphur. In addition to the GDOES results, a LECO® Carbon and Sulfur Combustion Analyzer was used to determine the carbon composition of the experimental alloys. The compositional analysis of the Fe-22Mn-0.6C steel can be seen in Table 4.1. In order to differentiate between the three experimental alloys, they will be referred to by their wt% carbon of 0.6C, 0.4C or 0.2C in the below text. The main alloying elements of manganese, chromium and silicon were determined based on the as-received 0.6C alloy, and were assumed to be consistent post-decarburization.

Table 4.1 Chemical Composition of Steel Alloys (wt%)

Alloy Name	C	Mn	Cr	Si
0.6C	0.5570	21.51	0.14	0.19
0.4C	0.3967			
0.2C	0.2533			

4.2 Heat Treatment and Decarburization

To examine the influence of carbon content on the properties of the experimental alloy, two other steels were created with lower carbon contents versus that of Fe-22Mn-0.6C alloy. The CO/CO_2 gas ratios needed to decarburize the 0.6C alloy to a carbon content of 0.4 and 0.2 weight percent were determined by calculating the carbon activity in the initial alloy compared with the desired alloy, and calculating the CO/CO_2 ratio for the correct composition. The activity calculation was performed using Thermo-Calc Software TCFE6 Database (Thermo-Calc) and Maple™ Mathematical Software was used to determine the length of time needed for decarburization, where the carbon activity was fixed on the steel surface and the time necessary to decarburize through the steel thickness calculated. From these calculations, a four hour decarburization at 1100°C was required to achieve a homogeneous 0.2 wt% carbon throughout the steel sheet. To maintain a consistent heat treatment through all three alloys, the four hour heat treatment at 1100°C in a tube furnace with the appropriate CO/CO_2 ratio, followed with an oil quench, was applied to all alloys. A tailored decarburization heat treatment was applied to the 0.6C alloy, to maintain the proper chemical composition in the existing alloy; in which the pre-cut tensile coupons were sealed into a quartz tube with helium prior to being placed in the furnace for 1100°C for four hours. To ensure uniform carbon concentration through all alloys, Vickers micro-hardness measurements through the cross-section of the steel were performed to confirm consistent hardness and uniform decarburization. The alloy CO/CO_2 gas ratios and heat treatments, are summarized below

in Table 4.2. A detailed explanation of the diffusion equations, conditions and Thermo-Calc conditions used to determine the CO/CO_2 can be seen in the Appendix (9.1 and 9.2).

Table 4.2 Decarburization and Heat Treatment Conditions

Alloy Name	CO/CO_2 Ratio	Heat Treatment
0.6C	-----	Sealed in quartz tube, 1100°C, 4 hours, oil quench
0.4C	27.74	1100°C, 4 hours, oil quench
0.2C	13.41	1100°C, 4 hours, oil quench

4.3 Mechanical Tensile Testing

An Instron 556 machine with a maximum load of 10kN was used for all tensile testing and all samples were tested at room temperature. Prior to tensile testing, the surface was cleaned of any surface carbon deposits arising from decarburization. A 100% extensometer was used for monotonic tensile tests, while a 40% extensometer was used for load-unload testing, where both were attached to the sample gauge. A cross head speed of 1 mm/min was used for all tests. Tests included monotonic tests to failure, interrupted tests, and load-unload (modified Bauschinger) tests with sample dimensions customized to best fit the machine and the extensometer as outlined in Figure 4.1. To prepare for chemical and materials characterization, a Struers® Accutome-2 cutter was used to section pieces of the tensile sample for materials characterization.

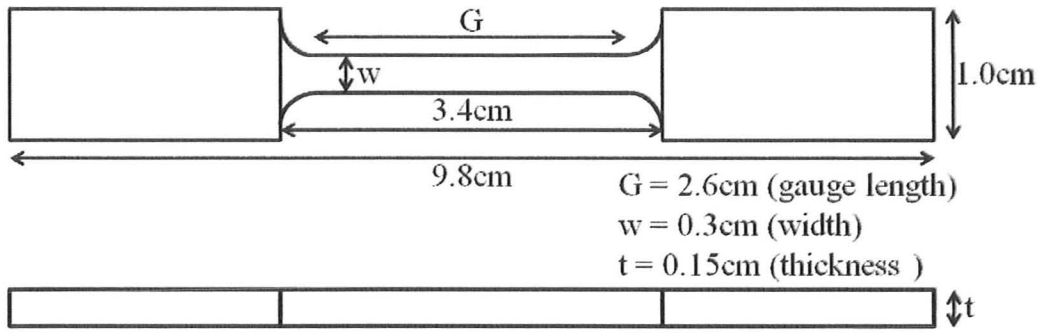

Figure 4.1 Tensile Sample Geometry

4.3.1. Monotonic Tensile Tests

These tests were used to examine the stress-strain behaviour to failure. Based on the data from this test, true stress-strain curves were plotted and various results determined, such as the sample uniform elongation, yield strength, ultimate tensile strength and fracture stress-strain. Fracture surfaces from these tests were viewed under the SEM to calculate the fracture area, in order to understand the post necking to fracture regime. From the true stress – strain plots, differential true stress-strain plots were made to examine the work hardening behaviour and the data was compared to the Considère's criterion (Equation 4.1) for the onset of plastic instability with σ_t and ε_t representing true stress and true strain, respectively.

$$\frac{d\sigma_t}{d\varepsilon_t} = .\sigma_t \tag{4.1}$$

4.3.2. Interrupted Tensile Tests

Interrupted tests were performed for true strain values of 0.02, 0.05, 0.10, 0.20 and 0.30 for all alloys to examine microstructural evolution as a function of strain. By

performing this test, twin and ε-martensite formation were examined for a better understanding of the deformation behaviour and to determine the phase transformation kinetics as a function of applied strain. The samples were unloaded at the specified true strain and were mounted for characterization using SEM imaging, quantitative XRD phase characterization, EBSD phase mapping and TEM analysis.

4.3.3. Load-Unload Tensile Tests

Traditional Bauschinger tests to examine the backstress accumulation are performed on cylindrical samples, where tension and compression are applied to the samples. Due to the inability to do conventional Bauschinger tests on sheet steel due to the buckling of flat samples, load-unload tensile tests were performed as a substitute, where the flow stress was taken as a sum of the yield strength, and both isotropic and kinematic hardening components, (Equation 4.2). The sample was loaded until it reached the pre-set true strain value, followed by unloading to 100N and reloading, creating load-unload cycles. The pre-set true strain unloading cycles occurred at 0.02, 0.05, 0.10, 0.20 and 0.30, matching the interrupted true strain values with a typical load-unload test seen in Figure 4.2.

$$\sigma_{total} = \sigma_{YS} + \sigma_{iso} + \sigma_{kin} \tag{4.2}$$

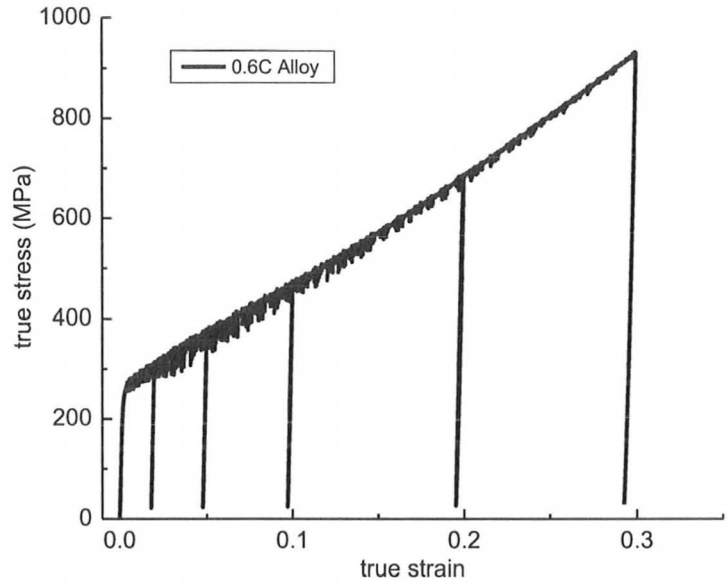

Figure 4.2 Sample Load-Unload Test

Figure 4.3 demonstrates that the unloading curve is not perfectly aligned with the elastic line, i.e. reverse plastic flow occurs from back stresses. The forward stress (σ_F) was the true stress value at the point of unloading, while the reverse stress (σ_R) was taken as the intersection of the elastic unloading line with a 0.01% offset to the unloading curve (Figure 4.3). As mentioned previously by Spencer (Spencer 2004) the 0.01% offset value affected the magnitude of the back stress value but does not affect the trend, so keeping the offset value consistent for all measurements yields the appropriate trends. The back stress (σ_B or kinematic hardening) was then calculated using Equation 4.3, by taking the sum of the absolute values of the forward and reverse stress and diving by 2 (Spencer 2004). This was done because of the directionality of the forward and reverse stress arising from the modified Bauschinger test.

$$\sigma_B = \frac{|\sigma_F| + |\sigma_R|}{2} \tag{4.3}$$

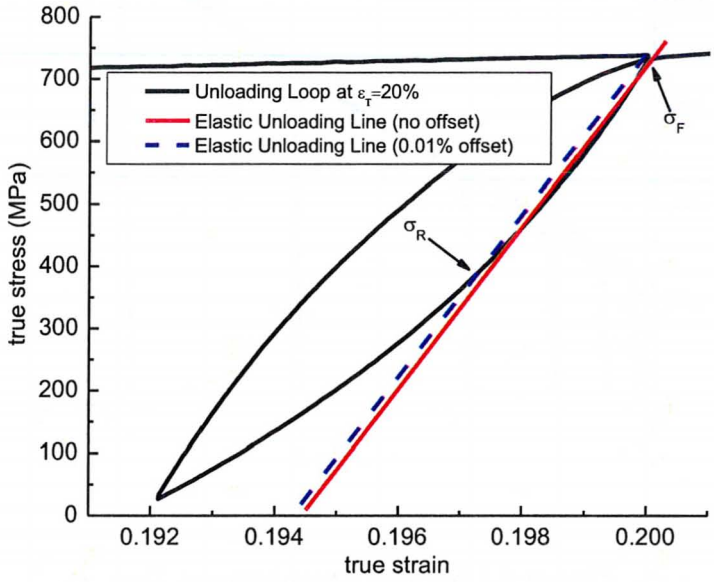

Figure 4.3 Bauschinger Unloading Loop Behaviour

4.4 Fracture Analysis

Fracture analysis was performed to gain a better understanding of the effect of the damage processes and fracture modes as a function of alloy composition. The fracture surface was viewed under the SEM. The dimensions of the fracture surface were also measured using both OM and SEM in order to calculate an approximate fracture stress and strain. A sample fracture surface is seen in Figure 4.4 with the area calculated using North Eclipse v. 6.0 imaging software. By taking the initial area (A_0) and calculating the final area (A_f), with the load at fracture (L_f), a true fracture strain (ε_f) and true fracture stress (σ_f) can be calculated from Equation 4.4 and Equation 4.5.

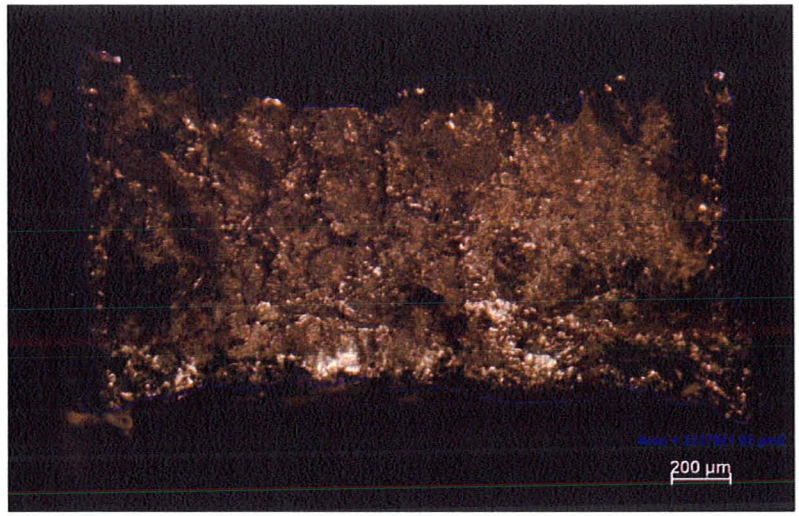

Figure 4.4 OM Image of Fracture Surface Calculation

$$\sigma_f = \frac{L_f}{A_f} \tag{4.4}$$

$$\varepsilon_f = \ln\left(\frac{A_0}{A_f}\right) \tag{4.5}$$

4.5 Metallographic Sample Preparation

4.5.1. Cutting and Mounting

Tensile samples were made by Electron Discharge Machining (EDM) to ensure low deformation and damage on the edges, thereby avoiding any strain induced phase transformations within the samples. Cut sections were mounted in a standard metallographic mount. Depending on the analysis required, the mounting technique was tailored to the requirements, with cold mounting used to avoid compressive forces in the hot mounting press. Detailed description of mounting conditions can be seen in the Appendix (9.3).

4.5.2. Polishing

Samples were polished using Struers® Automatic Polisher which helped maintain a consistent applied load and direction in polishing. Samples were polished prior to SEM imaging, XRD analysis and electropolishing for EBSD. Careful sample cleaning and rinsing of the sample holder was done with ethanol between each step to avoid any oxidation on surface. Due to the high sensitivity of the alloy to water, samples were rinsed quickly, dried and use of water avoided at later stages. Samples were also checked with the optical microscope between stages to ensure the polishing procedure was effective. The polishing procedure followed is outlined in the Appendix (9.4).

4.5.3. Etching

To reveal the microstructure of the polished surface for imaging, a 5% Nital room temperature etchant was used, with cleaning and rinsing done with ethanol. A typical etched microstructure can be seen in Figure 4.5 and consisted of uniform grains and annealing twins. Detailed etching procedure is outlined in the Appendix (9.5).

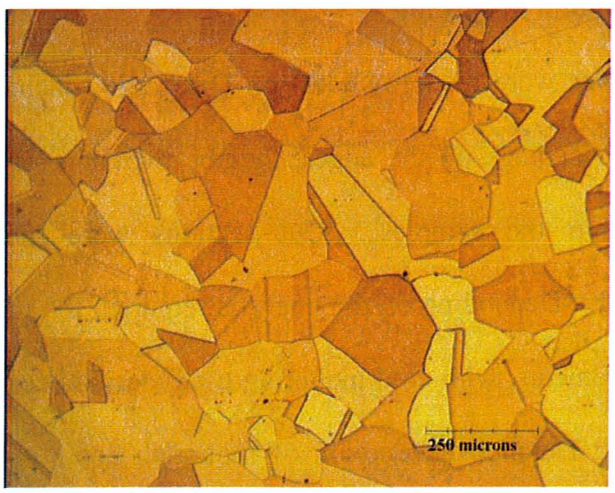

Figure 4.5 Etched Initial Microstructure of 0.4C Alloy

4.5.4. Electropolishing

For effective diffraction pattern indexing, electropolishing was used prior to EBSD analysis. Electropolishing revealed a strain free surface, which was not possible with mechanical polishing. Samples were pre-polished and demounted from the resin mount in pure acetone. The electropolishing electrolyte solution comprised 10% perchloric acid dissolved in High Purity Liquid Chromatography (HPLC) methanol which was chilled in an ice bath in order to yield more consistent results. Careful attention was paid to mixing the perchloric acid in HPLC methanol as the mixing reaction is exothermic, for which the solution temperature was constantly monitored and maintained below 30°C. A Struers® Polectrol Electrolytic Polishing and Etching apparatus was used and attached to a cold water circulation which ran through the machine. Samples were polished for 30 seconds to 1 minute, at a voltage of 45V and were rinsed quickly with water followed by rinsing with ethanol, and rapid drying using a warm air steam. Viewing under an optical microscope was done after each polishing to assess whether the polished surface was adequate for EBSD analysis. With very careful preparation and polishing, the results from electropolishing yielded acceptable indexing rates.

4.5.5. TEM Sample Preparation

Use of the Transmission Electron Microscope (TEM) required special sample preparation with all TEM work done on the Philips® CM 12 STEM/TEM by Dr. Xiang Wang. To prepare samples for analysis, samples were first thinned and finely polished to yield foils of approximately 80 μm thickness. Discs of 3 mm diameter were cut using a Gatan® mechanical foil punch to make the TEM foils. Foils were then electropolished

with a twin-jet polisher using an electrolyte solution of 10% perchloric acid in HPLC methanol. A Struers Tenu-Pol5 Controller Unit was used with a voltage of 38 V for approximately 45 seconds with the electrolyte cooled by a dry ice and methanol bath. This method was the same procedure used by Liang (Liang 2008).

4.6 Materials Characterization Techniques

Various materials characterization techniques were applied to the samples to best analyze and understand material behaviour. Each technique chosen was for a specific purpose in order to reveal relevant information. Optical Microscopy (OM) was used as preliminary analysis and on-going check to ensure proper polishing and sample preparation. Scanning Electron Microscopy (SEM) was used to image the microstructure as a function of applied strain as well as phase mapping with Electron BackScattered Diffraction (EBSD). X-ray Diffraction (XRD) was applied to quantitatively determine the amounts of austenite and ε-martensite as a function of plastic deformation. Transmission Electron Microscopy (TEM) techniques were used to examine the dislocation cell structure, the interaction of ε-martensite platelets, twins and stacking faults. The various conditions and applications used in each technique are discussed in the following sections.

4.6.1. Scanning Electron Microscopy (SEM)

Secondary electron imaging was used to characterize the microstructure as a function of carbon content and true strain, as well as the fracture surfaces. A small beam size, working distance of 6-10 mm and an acceleration voltage of 10-15keV were used

throughout the study using the JEOL JSM-7000F FEG-SEM (Field Emission Gun – Scaning Electron Microscope). However, due to the phase transformations that exist in the alloys being of the same composition but of different crystallography, secondary electron imaging was unable to differentiate between twinning and ε-martensite formation. In order to differentiate between twin and ε-martensite formation, EBSD was performed and the conditions on the SEM were altered versus those described above.

4.6.2. Electron BackScattered Diffraction (EBSD)

For phase mapping of twins, austenite and ε-martensite, EBSD was used to determine the distribution of phases in the microstructure based on crystallography. The conditions applied during EBSD were: medium beam size, working distance of 18.4mm, acceleration voltage of 20 keV, detector distance of 185.7 mm, and sample tilt at 70° using the same JEOL JSM-7000F FEG-SEM with the "Flamenco" HKL Channel 5 program. Depending on the surface conditions of the sample, the step size was varied from 0.1-0.3 μm. The conditions were set to maximize the indexing of the Kikuchi patterns.

The HKL software package "Tango" was used to analyze the data and to obtain phase maps. The phase map displayed various phases in different colours with the parent austenite phase (FCC) assigned to red, ε-martensite (HCP) in blue and twin boundaries highlighted in yellow, with {111} as the twinning plane and a misorientation angle of 60° with an allowable deviation of 5°.

4.6.3. Transmission Electron Microscope (TEM)

Transmission Electron Microscopy (TEM) analysis was performed to look at the dislocation cell structures, ε-martensite platelets, twins and stacking fault interactions in the deformed specimen. A Philips® CM 12 STEM/TEM was used by Dr. Xiang Wang for this analysis. The conditions chosen were to optimize viewing of the microstructural features with beam energy of 120 kV and electron wave length of 0.0337 Å. Bright Field (BF), Dark Field (DF) imaging as well as limited selected area diffraction (SAD) analysis was performed.

4.6.4. X-Ray Diffraction (XRD)

X-ray Diffraction (XRD) analysis was performed at Proto Manufacturing Limited on the Proto LXRD machine to quantitatively determine the amounts of ε-martensite. The LXRD machine used a chromium target with an average Kα line of 2.291 Å using a voltage and current of 30.0 kV and 25.0 mA, respectively. The three-peak method was used with a collection time of one second with 50 exposures, and a large rectangular aperture of 2 by 5 mm to achieve better results for random grain orientation distributions. These specifications were chosen by the Proto Manufacturing Ltd operator and an image of the set-up can be seen in Figure 4.6.

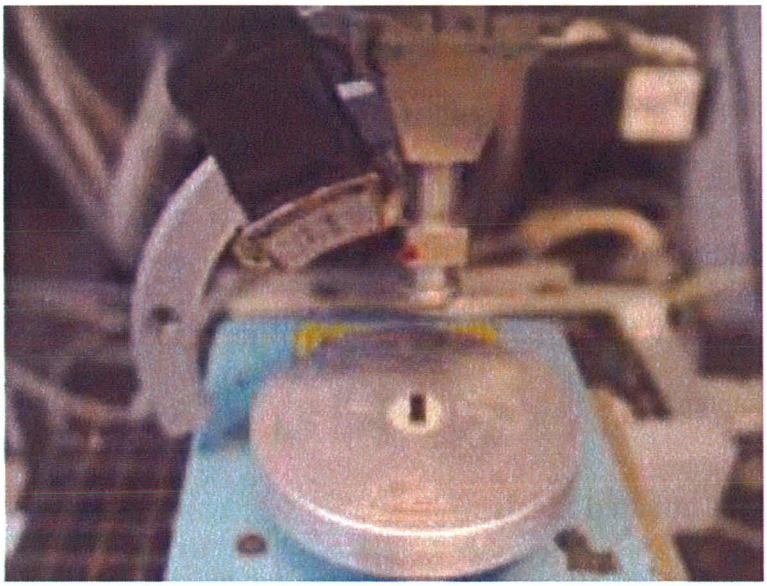

Figure 4.6 XRD Set Up by Proto LXRD Machine

5. RESULTS

This chapter presents the results of the experiments performed for all alloys. The as-annealed microstructure and mechanical properties for all alloys are first presented, followed by additional observations of microstructural evolution, fracture modes and TEM analysis of the 0.6C, 0.4C and 0.2C alloys. A detailed discussion of the results can be found in Chapter 6.

5.1 As-Annealed Steels

The experimental alloys were heat treated following the method mentioned in Chapter 3, and images of the as-annealed microstructure were taken with SEM secondary electron imaging and EBSD phase maps acquired as shown in Figure 5.1, Figure 5.2, and Figure 5.3, for the 0.6C, 0.4C and 0.2C alloys, respectively. The EBSD images mapped austenite in red, ε-martensite in blue and twins in yellow for all alloys. These initial micrographs were used as a point of reference when comparing the alloys and the effect of deformation. The 0.6C initial microstructure as seen in Figure 5.1 showed equiaxed grains with annealing twins and an average grain size of 150 μm. The microstructure of this alloy predicted by its SFE (Nakano 2010, Allain 2004b) was expected to be fully austenitic with no deformation or phase transition products (twins or ε-martensite) and mechanical twinning would occur upon deformation. The EBSD phase map confirmed an austenitic microstructure, verifying the prediction concerning the initial microstructure.

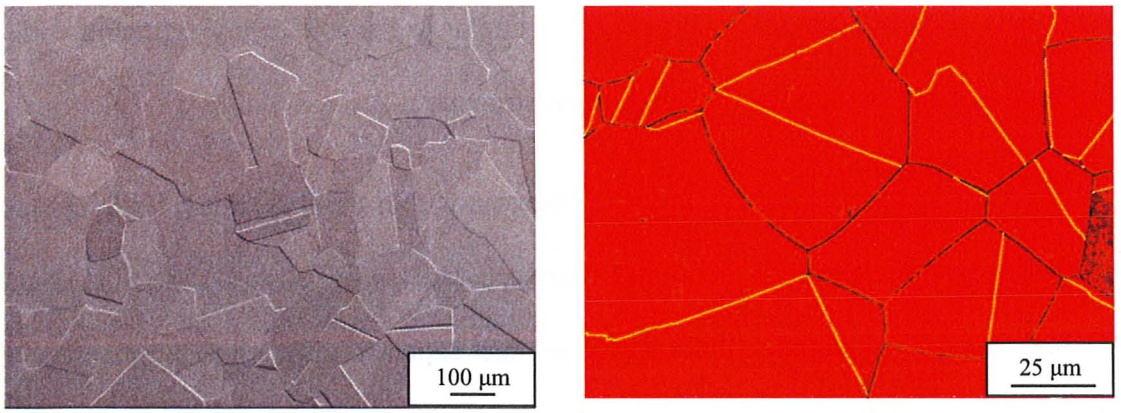

a) Annealed Microstructure b) EBSD Phase Map

Figure 5.1 Annealed Microstructure of 0.6C Alloy

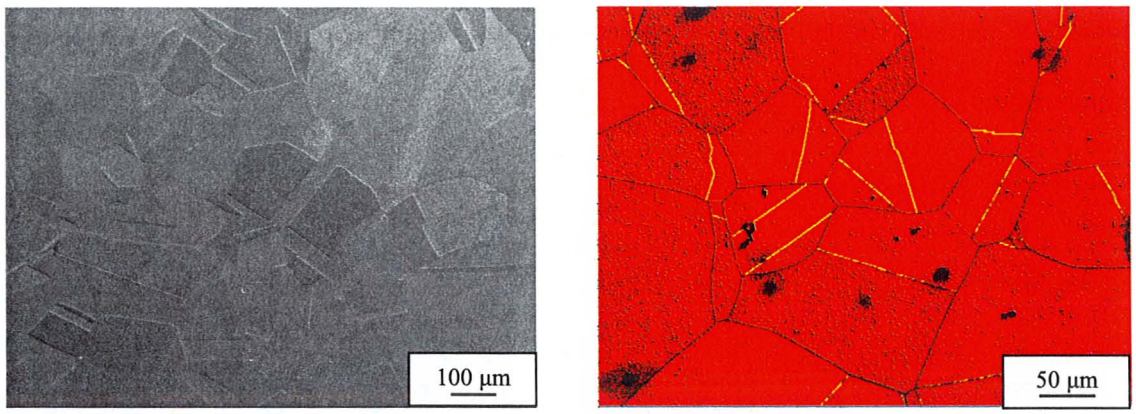

a) Annealed Microstructure b) EBSD Phase Map

Figure 5.2 Annealed Microstructure of 0.4C Alloy

The 0.4C microstructure shown in Figure 5.2a revealed equiaxed grains averaging 135 µm in size, annealing twins, and an initial single austenite phase. With predictions from the SFE (Nakano 2010, Allain 2004b), this alloy was considered to contain a parent austenite phase with possible production of both mechanical twins and ε-martensite as deformation products, resulting in a dual phase microstructure and dual TWIP/TRIP behaviour. From the initial EBSD observations (Figure 5.2b), there was no presence of ε-

martensite with an austenitic microstructure similar to the 0.6C alloy, agreeing with the predictions made concerning the initial microstructure.

A dual phase microstructure was observed within the 0.2C alloy, with regions of austenite and ε-martensite in the initial microstructure, as predicted by the SFE (Nakano 2010, Allain 2004b) with the deformation product expected to be ε-martensite. The dual phase microstructure seen in Figure 5.3 displayed grains of austenite with platelets of ε-martensite intersecting and subdividing austenite grains, similar to the structure observed in Liang's Fe-24Mn alloy (Liang 2008). This microstructure was different from that observed for the higher carbon content alloys, which comprised of a single phase microstructure.

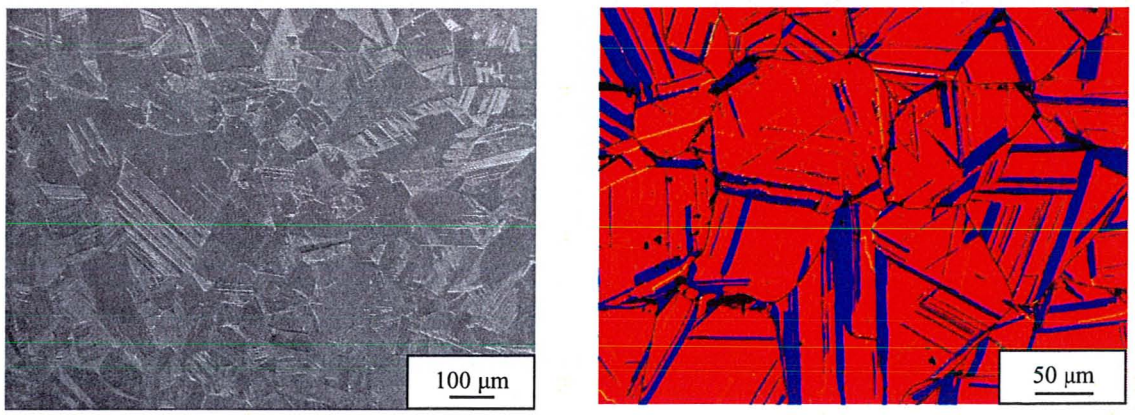

a) Annealed Microstructure b) EBSD Phase Map

Figure 5.3 Annealed Microstructure of 0.2C Alloy

5.2 Mechanical Properties

5.2.1. Monotonic Tensile Behaviour to Fracture

Monotonic tensile tests to fracture were performed at room temperature for all alloys. A minimum of three tests were performed to assess the consistency of the results. As noted before, small changes in the heat treatment could have altered the carbon content and affected the mechanical behaviour. For the 0.6C and 0.4C alloys, a consistent mechanical response was achieved. For the 0.2C alloy, a small variation in mechanical response was observed, likely due to the inconsistent carbon content. Typical true stress - strain curves were plotted for each alloy and can be seen below.

Figure 5.4 displays the tensile behaviour of the 0.6 alloy with the true tensile curve showing an average yield strength (YS) of 260 MPa, average ultimate tensile strength (UTS) equalling 1407 MPa and an average uniform elongation of 0.53. After approximately 0.10 tensile deformation, there was a change in the flow stress slope, possibly due to the production of deformation products.

The mechanical response of the 0.4C alloy resulted in an average YS of 245 MPa, an average UTS of 1040 MPa, and an average uniform elongation of 0.40 true strain from Figure 5.5. The YS, UTS and uniform elongation were significantly lower compared to the 0.6C alloy with a similar slope change after 0.10 true strain due to production of deformation products.

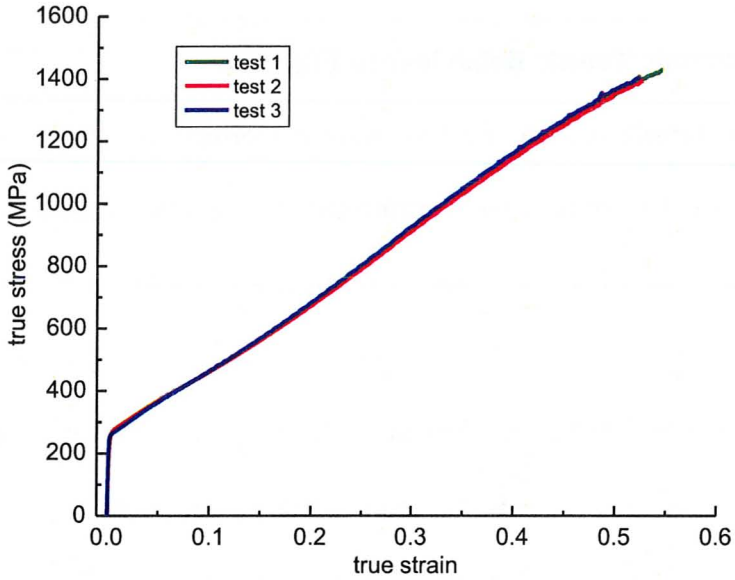

Figure 5.4 True Stress – Strain Tensile Behaviour for 0.6C Alloy

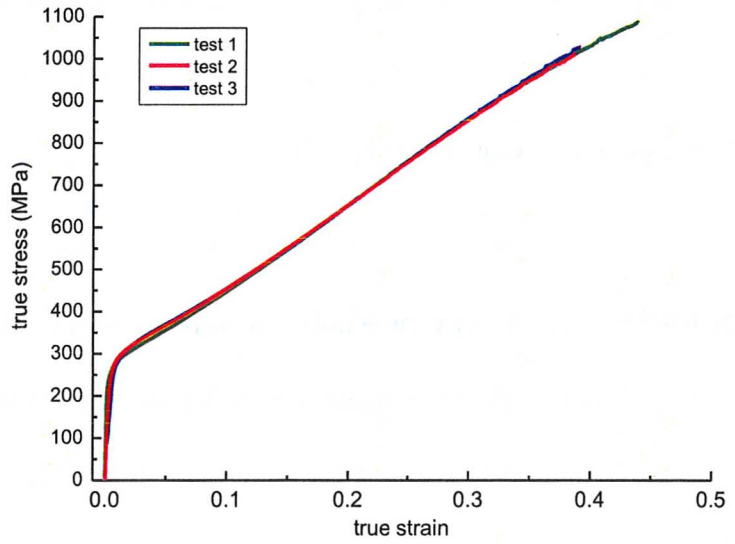

Figure 5.5 True Stress - Strain Tensile Behaviour for 0.4C Alloy

The monotonic tensile behaviour to fracture for the 0.2C alloy displayed a true YS averaging 212 MPa, an average UTS of 1009 MPa and an average uniform elongation of 32%, as seen in Figure 5.6. The mechanical response of this alloy was not similar to the 0.6C and 0.4C alloy, because of the initial dual phase microstructure and deformation products formed. Due to the presence of ε-martensite in the alloy, and the transformation of the softer austenite to a harder ε-martensite phase, the strength of this alloy was higher and the ductility lower compared to the other two alloys.

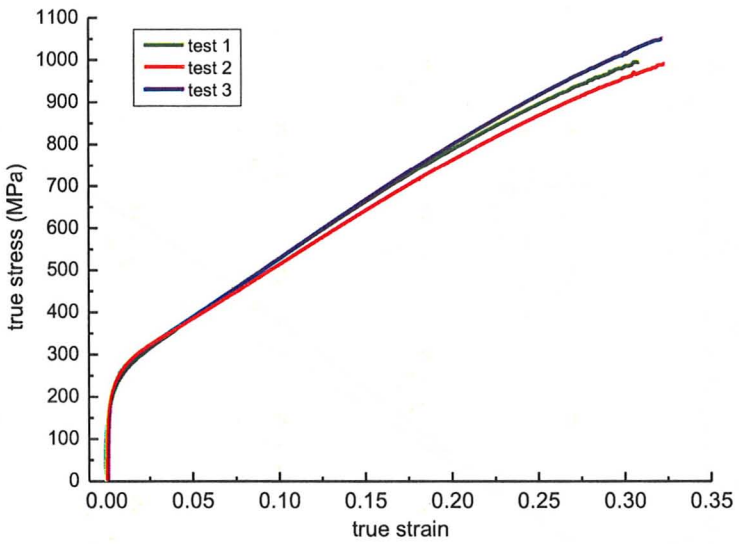

Figure 5.6 True Stress - Strain Tensile Behaviour for 0.2C Alloy

A comparison of the alloys and their representative mechanical properties is seen in Table 5.1 with YS, UTS and uniform elongation calculated from the true stress – strain curve. A representative curve for each alloy was used for comparison of their true stress – strain response and can be seen in Figure 5.7. The 0.6C alloy displayed the highest

strength and uniform elongation. The 0.2C and 0.4C alloy showed similar strength with the 0.4C alloy reaching a higher uniform elongation. The curves displayed in Figure 5.7 will be used in further discussions and represents each alloy's monotonic flow curves.

Table 5.1 Alloy True Mechanical Properties Comparison

Alloy	YS (MPa)	UTS (MPa)	Uniform Elongation (%)
0.6C	260	1407	53
0.4C	245	1040	40
0.2C	212	1009	32

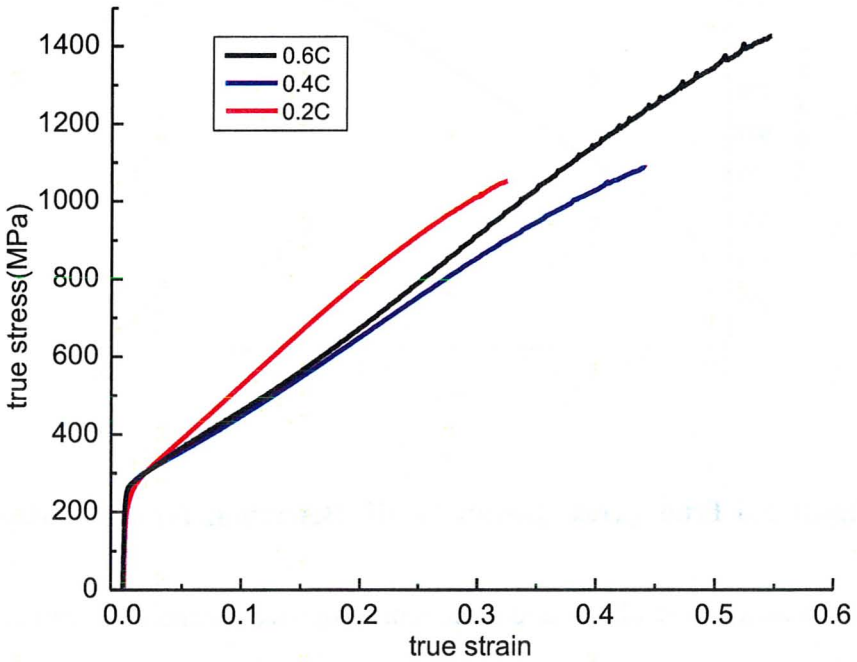

Figure 5.7 Tensile Behaviour (True Stress - Strain) for All Alloys

5.2.2. Work Hardening Response

The work hardening response was examined by taking the derivative of the plastic flow curve ($d\sigma_t/d\varepsilon_t$) vs. σ_t, to examine the rate at which the material work hardened. The onset of plastic instability by the Considère criterion was used to determine the value of uniform elongation for each alloy. This was computed by overlaying a $d\sigma/d\varepsilon = \sigma_t$ line along with the work hardening curve to determine the stress at the intersection. The serrations seen in the upper region of the monotonic tensile curve for the 0.6C and 0.4 C alloys led to large fluctuations in the derivatives and these were filtered using a 5 point averaging scheme to decrease the fluctuations. The resulting work hardening curves are seen in Figure 5.8, where the serrations for the 0.6C and 0.4C alloy can be seen to be significant despite the use of the filter.

The 0.6C and 0.4C alloy work hardening rates decreased rapidly during initial deformation and after a strain of ~0.10, the work hardening rate started to increase, as a result of the onset of twinning. The 0.6C alloy exhibited a larger uniform elongation than the 0.4C alloy, with a larger region of high work hardening rate values before fracture. The consistently higher work hardening values observed is commonly seen for TWIP alloys (Bouaziz 2009). The dual-phase 0.2C alloy showed a higher initial work hardening rate versus the 0.6C and 0.4C alloys and displayed a slight increase with plastic deformation before becoming relatively constant, prior to decreasing to failure. The exhibited behaviour was characteristic of a TRIP alloy for the 0.2C alloy (Liang 2008).

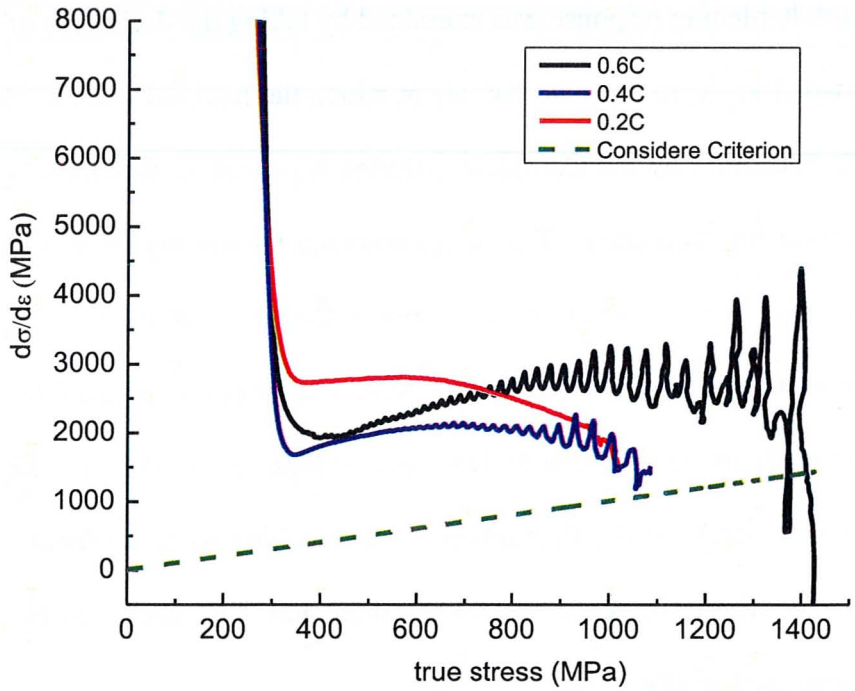

Figure 5.8 Work Hardening Behaviour for All Alloys

5.2.3. Kinematic Hardening

Load-unload or modified Bauschinger tests were performed to calculate the contribution of kinematic hardening to the overall flow stress as a function of deformation of true strain values of 0.02, 0.05, 0.10, 0.20, and 0.30. Due to the extensometer limitations mentioned previously, the maximum true strain reached was 0.30. The calculated back stress was dependent on the offset value chosen, so it is important to consider the trends in the back stress rather than the numerical values themselves. The load-unload data versus ε_t was overlaid with the monotonic tensile data and confirmed the consistency in the work hardening behaviour, shown for the 0.6C alloy in Figure 5.9, with

the same consistency true for the 0.4C and 0.2C alloys. The kinematic hardening was seen to contribute significantly to the overall flow stress indicating that the interaction of dislocations with the deformation products represents a major contribution to the hardening of the alloys. The response for the true strains observed (0 to ε_t=0.30) and the hardening response for ε_t>0.30 was not explored.

For the 0.6C alloy, from the SFE estimations, these deformation products were predicted to be mechanical twins and this was later confirmed with EBSD phase maps. The calculated kinematic hardening response shown in Figure 5.10 for the 0.6C alloy displayed a large portion of the flow stress to the kinematic hardening.

The 0.4C alloy kinematic hardening trend was similar to the 0.6C with a significant portion of kinematic hardening contributing to the total flow stress. The calculated back stress for the 0.4C alloy, displayed in Figure 5.11, revealed the back stress possibly beginning to saturate for $\varepsilon_t > 0.30$ due to a limited amount of deformation products within this alloy. This will be further discussed after XRD and EBSD analysis.

The 0.2C alloy displayed a kinematic hardening response per Figure 5.12 with the curve displaying a different trend compared with the other two alloys. The 0.2C began to turn over (saturate), and contributed less to the overall flow stress with back stress values increasing at a lower rate, indicating that the deformation products produced had a reduced contribution to the work hardening and were becoming saturated with dislocations prior to 0.30 true strain.

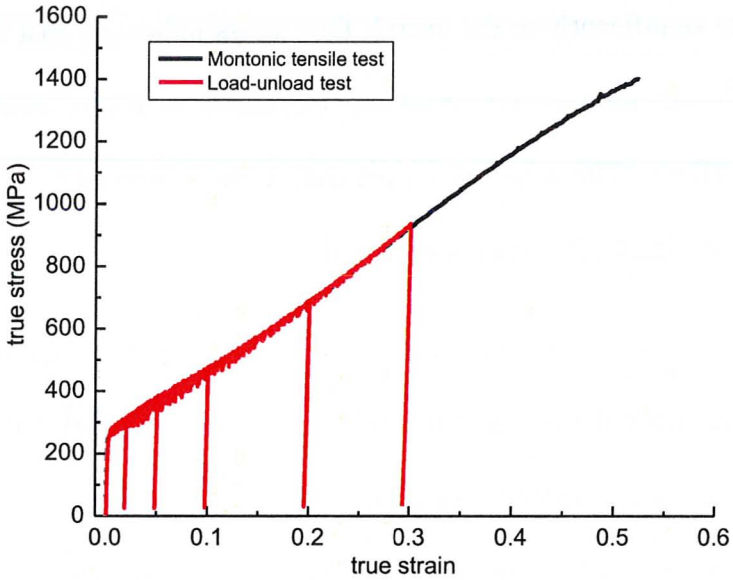

Figure 5.9 Overlay of Load-Unload Test and Monotonic Tensile Test for 0.6C Alloy

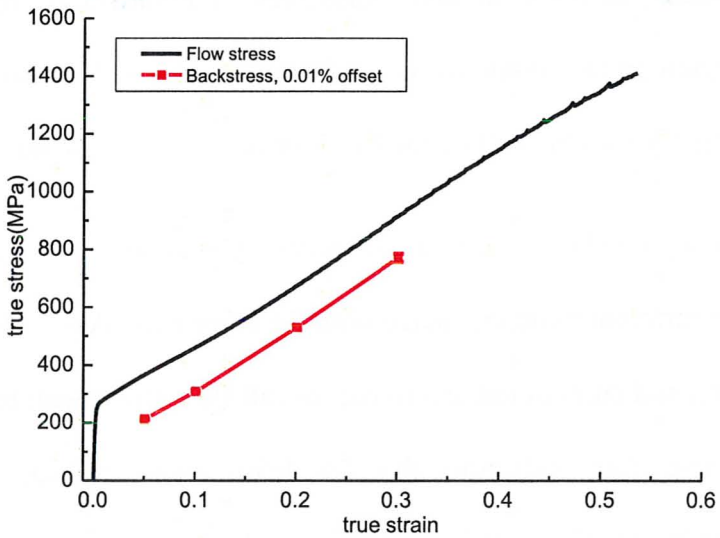

Figure 5.10 Back Stress Development in 0.6C Alloy

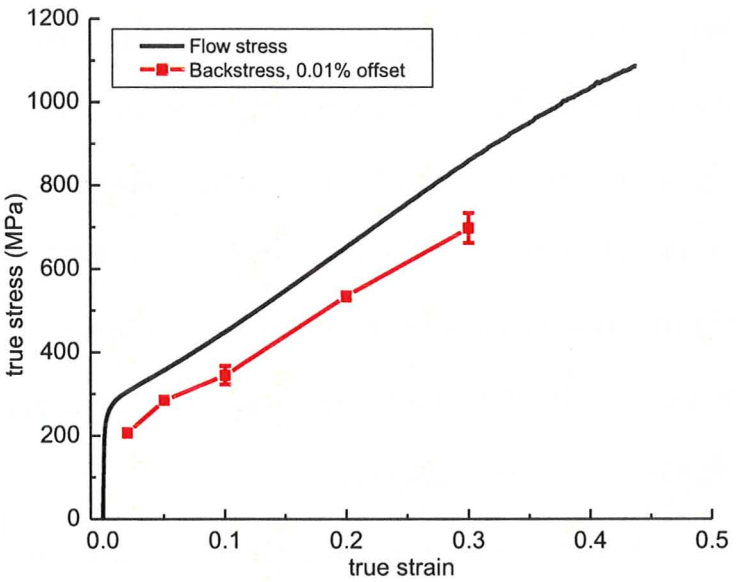

Figure 5.11 Back Stress Development in 0.4C Alloy

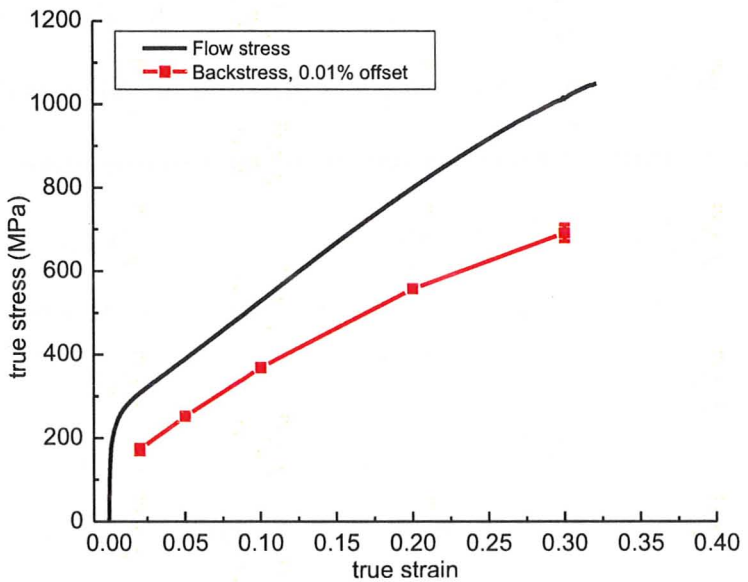

Figure 5.12 Back Stress Development in 0.2C Alloy

5.2.4. XRD Phase Analysis

To confirm the presence of ε-martensite in the deformed microstructures, XRD analysis was performed on all alloys as a function of plastic strain, measuring amounts of austenite and ε-martensite. A plot of ε-martensite volume percentages as a function of true strain for all the alloys is shown in Figure 5.13. The 0.6C alloy displayed no significant amount of ε-martensite, with the microstructure being comprised solely of austenite. This further confirmed the TRIP deformation mechanism did not occur within the 0.6C alloy, resulting in a single austenite phase.

For the 0.4C alloy, the alloy initially contained a small amount of ε-martensite, which increased with tensile strain, and saturated at around 0.20 true strain with approximately 12% ε-martensite. The SFE data had predicted the formation of ε-martensite as a deformation product, although at relatively low strains the amounts of ε-martensite in the 0.4C and 0.6C alloys was below the detection limit. After approximately 0.10 true strain, ε-martensite was present in the alloy (TRIP mechanism), with production of ε-martensite seen between 0.10 and 0.20 true strain. The production of ε-martensite correlated well with the work hardening data (Figure 5.8) and the kinematic hardening trend (Figure 5.11), with an increase in the work hardening until 650MPa or 0.20 true strain. The kinematic hardening contribution showed the back stress beginning to turn over at ε_t>0.20, linking to the saturation of ε-martensite.

The 0.2C alloy contained both austenite and ε-martensite, as predicted by the SFE and confirmed by images of the as-annealed microstructure. XRD analysis revealed approximately 7% ε-martensite within the as-annealed microstructure with the amount

increasing with deformation to 0.10 true strain and was approximately constant at 40% until fracture. The work hardening data of the 0.2C alloy revealed a constant work hardening rate until 500 MPa corresponding to 0.10 true strain, where the production of ε-martensite stopped. In relation to the kinematic hardening response (Figure 5.12), the back stress started turning over at ε_t>0.10, which was the strain where ε-martensite production stopped, linking the production of ε-martensite or deformation products to a decreasing contribution of kinematic hardening to the overall flow stress.

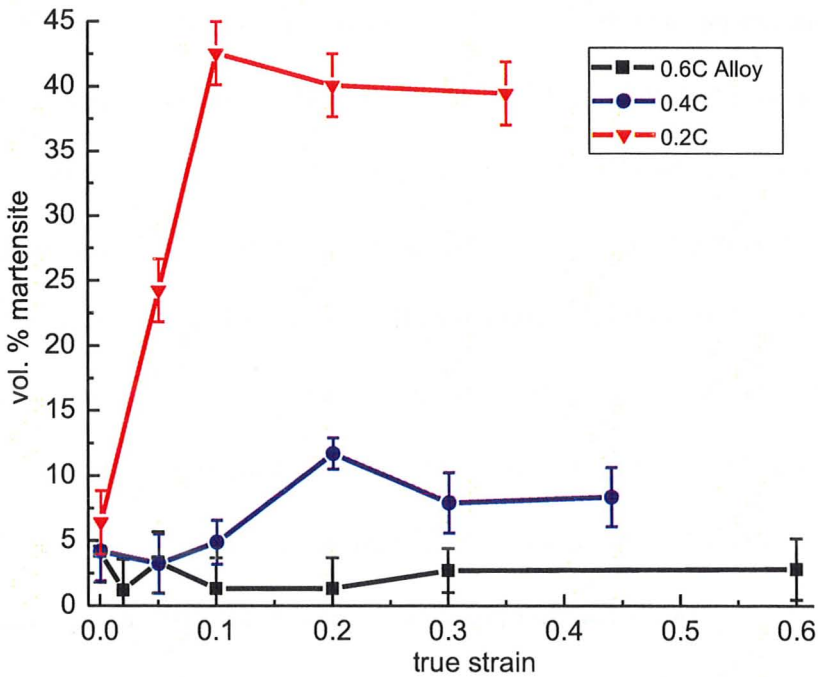

Figure 5.13 XRD ε-Martensite Phase Analysis for All Alloys

5.3 0.6C Alloy Microstructural Evolution vs. Strain

The following section presents more detailed results of the 0.6C alloy including the interrupted tensile tests examining microstructural evolution, EBSD phase analysis as a function of strain, and fracture analysis. From these results, the general behaviour of the 0.6 alloy was determined.

5.3.1. SEM Observations

Interrupted tensile tests were performed at room temperature to observe the microstructural evolution as a function of deformation, by examining the amounts of austenite, ε-martensite, and twin boundaries in the deformed microstructure. Samples were unloaded at ε_t of 0.05, 0.10, 0.20, 0.30, and fracture, similar to the modified Bauschinger tests, and SEM micrograph images and EBSD phase maps taken. Figure 5.14a-f shows the microstructural evolution as a function of strain, with the tensile direction being the horizontal direction for all images. Initially (Figure 5.14a), uniform austenite grains (confirmed through Figure 5.1b) were seen with annealing twins and no deformation products. After 0.05 tensile deformation, initiation of deformation products was observed within the microstructure (white circles in Figure 5.14b) which terminated at grain boundaries. Transformation products were not uniform throughout the sample, with minimal observed transformation products in isolated grains. By increasing deformation to 0.10 true strain, similar results were seen with portions of the microstructure exhibiting transformation (white circles in Figure 5.14c). Reaching higher true strains of 0.20, as shown in Figure 5.14d, a different microstructure was observed, with uniform regions of transformation throughout the alloy. The striations or

deformation products, which were most likely twin boundaries, occurred in all grains and stopped at grain boundaries. The difference between the micrographs at 0.10 and 0.20 true strain indicate the on-set of significant twin formation at ε_t=0.10 – 0.20. Reaching a strain of 0.30, Figure 5.14e shows uniform transformation in the sample with grains appearing elongated in the tensile direction (horizontal direction). At fracture (0.53) the microstructure in Figure 5.14f revealed highly deformed grains with transformation products throughout the sample. Grains were found to be elongated in the tensile direction with striations following the tensile direction, terminating at grain boundaries. The fractured microstructure exhibited void formation along striations and boundaries, highlighted by the white circle in the lower portion of the micrograph.

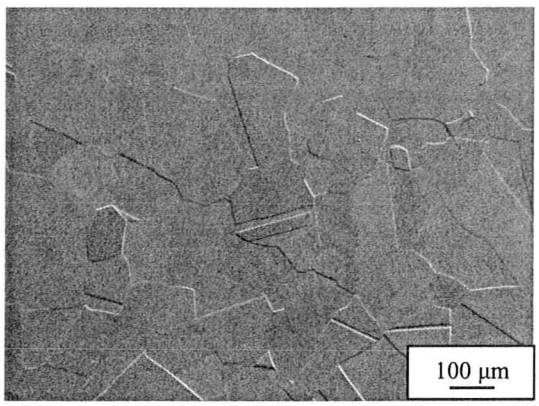

a) Annealed Microstructure, ε_t=0.0

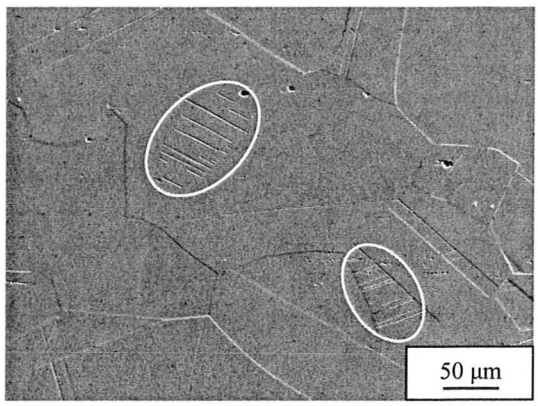

b) ε_t=0.05

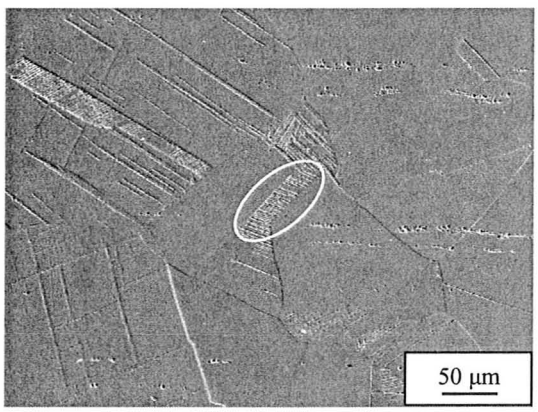

c) ε_t=0.10

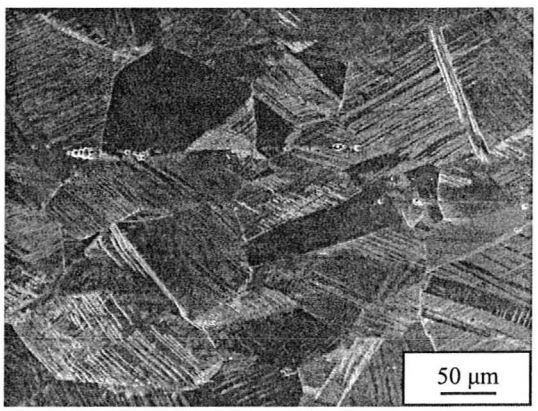

d) ε_t=0.20

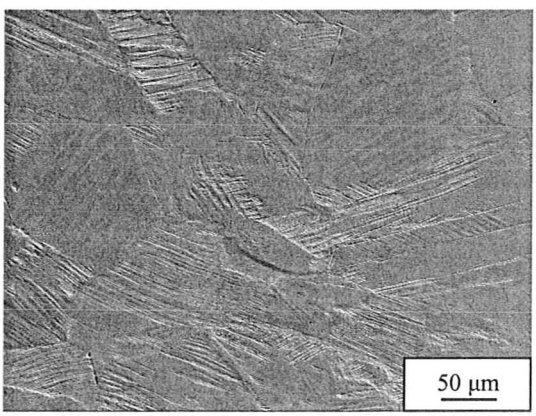

e) ε_t=0.30

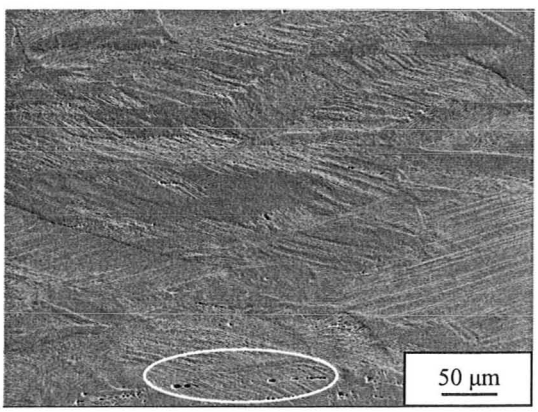

f) Fractured Microstructure, ε_t=0.53

Figure 5.14 SEM Microstructural Evolution as a Function of Strain for 0.6C Alloy

5.3.2. EBSD Phase Maps

Using the interrupted tensile test samples and the microstructural images from secondary electron imaging, EBSD analysis was performed to confirm the phases present and the deformation mechanism within the alloys. From the SFE predictions, the deformation mechanism was expected to be a combination of dislocation glide and twinning. SEM microstructural evaluation revealed an initial austenite matrix with deformation products developing as strain increased. Using the conditions outlined in the previous section, phase maps were made. The as-annealed microstructure, Figure 5.1b, revealed a uniform austenite microstructure with annealing twins and large grains. As true strain reached 0.10 (Figure 5.15a), the austenite matrix contained deformation twins within some grains in various directions. At ε_t= 0.20 (Figure 5.15b), the phase map revealed significant deformation twinning in isolated grains with twins stopping at grain boundaries. Increasing strain further (ε_t=0.30, Figure 5.15c), increased twinning was observed throughout the microstructure. At fracture, (Figure 5.15d) the phase map revealed significant transformation in the microstructure with most striations highlighted as twin boundaries. When comparing Figure 5.14f and Figure 5.15d, the striations observed in the microstructure were indexed as twins and would be further indexed had not the surface been so damaged. By comparing the EBSD phase maps at various true strains, the deformation mechanism, for the 0.6C alloy was found to be dislocation glide and mechanical twinning. This was further confirmed by the XRD data (Figure 5.13) which showed no significant ε-martensite transformation in this alloy.

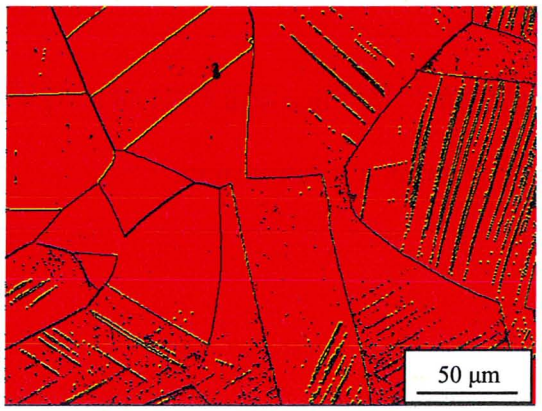

a) ε_t=0.10

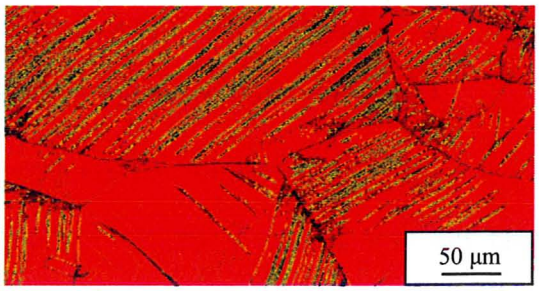

b) ε_t=0.20

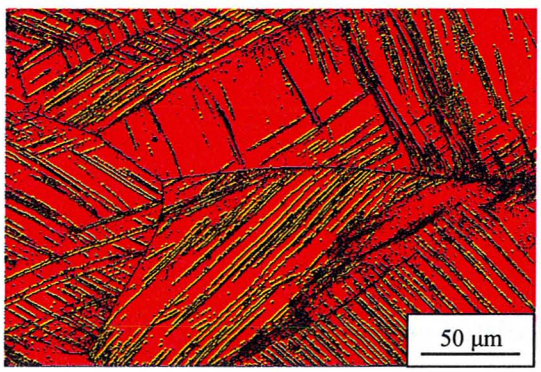

c) ε_t=0.30

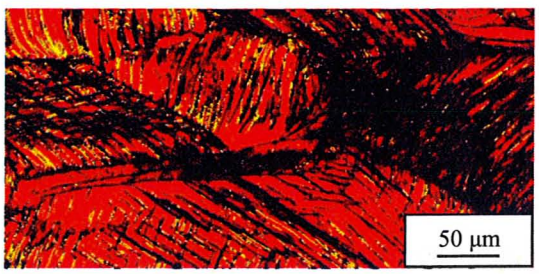

d) ε_t=0.53

Figure 5.15 EBSD Phase Mapping of Microstructure for 0.6C Alloy (Step Size 0.1-0.3 μm)

5.4 0.4C Alloy Microstructural Evolution vs. Strain

This alloy was similar to the 0.6C alloy with an initial austenitic microstructure and similar initial monotonic tensile behaviour. The microstructural evolution as a function of strain via secondary electron imaging and EBSD phase maps will be discussed in this section. TEM analysis will also be presented.

5.4.1. SEM Observations

Interrupted tensile tests were performed on the 0.4C alloy to evaluate the microstructural evolution as a function of strain. Samples were unloaded at similar strains as the 0.6C alloy and the same characterization techniques applied. The microstructural evolution as a function of deformation revealed similar features to the 0.6C alloy, as seen in Figure 5.16a-d. The annealed microstructure in Figure 5.16a showed uniform grains of a single austenite phase with some annealing twins. As true strain reached 0.10, deformation products were evident in many grains (Figure 5.16b). The grains had not yet been elongated in the tensile direction (horizontal direction) and some grains appear un-transformed. At strains of 0.30, grains appeared slightly elongated in the tensile direction and the majority of grains containing deformation products (Figure 5.16c). At fracture, the microstructure observed in Figure 5.16d was highly deformed with grain elongation and multiple striations in the grains. The deformations products observed were predicted to be a combination of mechanical twins and ε-martensite. The striations were found to intersect each other and terminate at grain boundaries. EBSD phase maps were taken to understand deformation behaviour of this alloy because of the possibility of both twinning and ε-martensite deformation products.

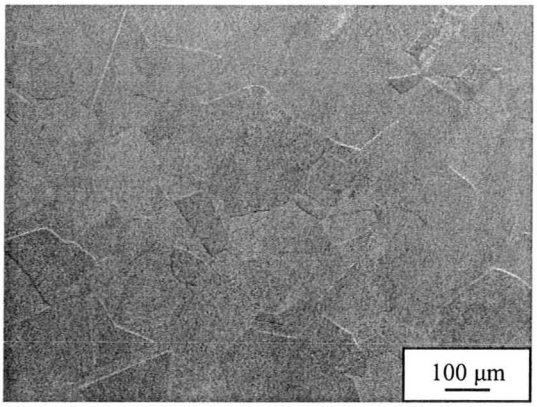

a) Annealed Microstructure, ε_t=0.0

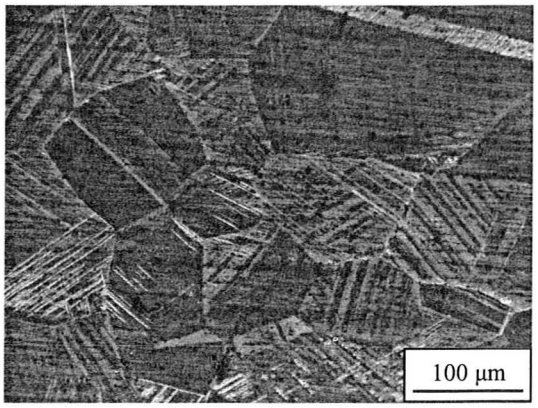

b) ε_t=0.10

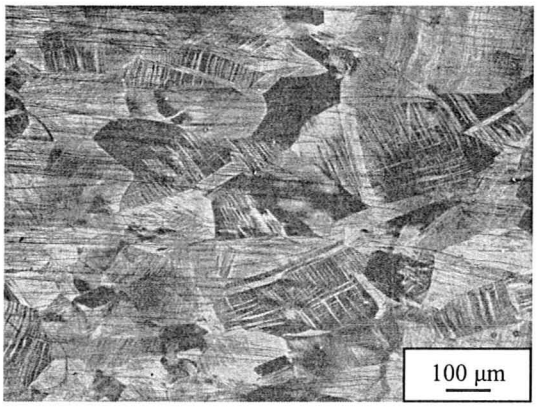

c) ε_t=0.30

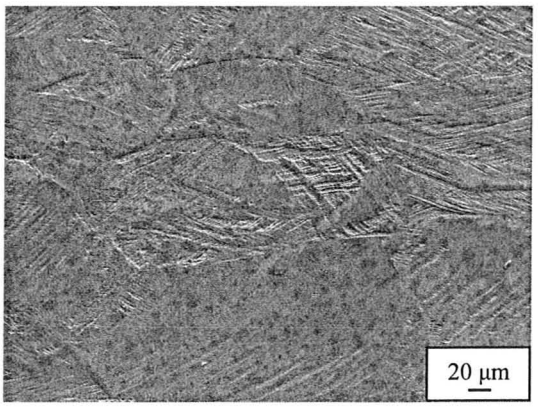

d) Fractured Microstructure, ε_t=0.44

Figure 5.16 SEM Microstructural Evolution as a Function of Strain for 0.4C Alloy

5.4.2. EBSD Phase Maps

From the microstructural information observed with the interrupted tensile tests, the complete deformation mechanism remained unknown within the 0.4C alloy, with knowledge of ε-martensite (TRIP effect) from XRD analysis. In order to distinguish between twinning and ε-martensite, EBSD phase maps were made to characterize the alloy at various stages of deformation. As was the case for the 0.6C alloy, the annealed microstructure was fully austenitic with annealing twins, as shown in Figure 5.2, with

randomly orientated grains and no significant ε-martensite detected. As 0.10 true strain was reached, (Figure 5.17a) the initiation of mechanical twins with a small portion of ε-martensite was detected in the lower right region of the phase map. Comparing this phase map with Figure 5.16b, the primary deformation products observed were identified as mechanical twins. Reaching true strains of 0.30, Figure 5.17b displayed the parent austenite phase with more mechanical twinning throughout the grains. Areas of ε-martensite were observed in the lower right corner of the phase map, although more was expected per the XRD data. At the point of fracture (ε_t=0.44), the phase map was expected to reveal a similar structure to the map displayed for 0.30 true strain, as the XRD analysis concluding that no further production of ε-martensite after 0.20 true strain. The fracture phase map (Figure 5.17c) displayed an austenite matrix with twins and little ε-martensite. From these phase maps, the deformation products comprised mainly of mechanical twins with a slight production of ε-martensite. The amount of ε-martensite in the phase maps did appear in the same quantities as XRD analysis revealed. However, this may be due to the limited number of grains examined by EBSD.

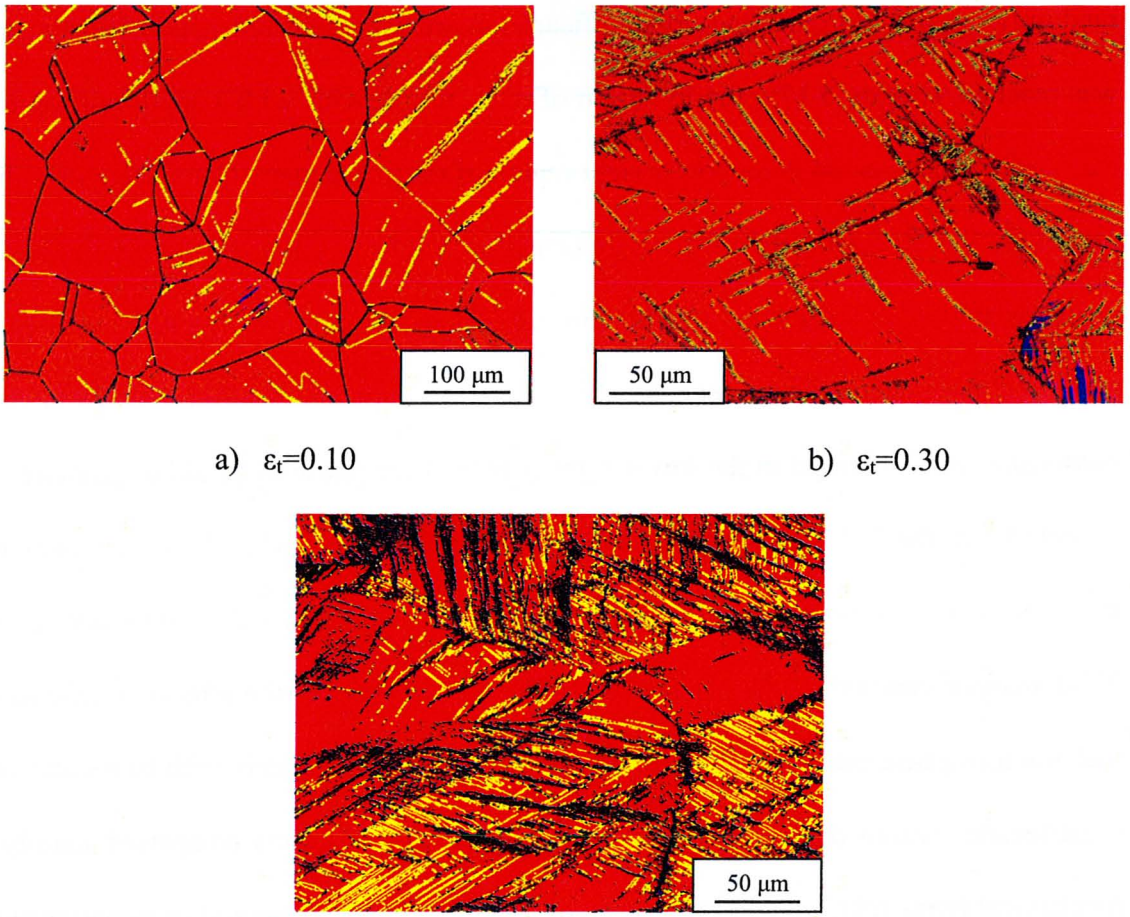

a) ε_t=0.10 b) ε_t=0.30

c) ε_t=0.44 (fracture)

Figure 5.17 EBSD Phase Mapping of Microstructure for 0.4C Alloy

5.4.3. TEM Analysis

Transmission Electron Microscopy was used to analyze the fine scale microstructure of the 0.4C alloy as a function of plastic strain. From the tensile behaviour, SEM micrographs and EBSD phase maps, a TWIP/TRIP deformation mechanism was observed. The TEM analysis observed the dislocation cell structure, dislocation and stacking fault (SF) interaction, deformation bands, twins and ε-martensite. The 0.4C alloy deformed at 0.10 true strain, from EBSD phase maps and XRD analysis,

comprised striations of annealing and mechanical twins with an estimated 5% ε-martensite. In terms of the dislocation structure, bright field (BF) images revealed a cellular structure with dislocation bands and stacking fault interactions, seen in Figure 5.18a. Dislocations were abundant and stacking faults were seen to interact with the cellular dislocation structure. At a true strain of 0.10 deformation bands were observed within the microstructure (Figure 5.18b-c). For the sample seen in Figure 5.18c, the overall structure consisted of stacking faults interacting with dislocations in a cellular structure. When examining for twins and ε-martensite, few twins were found and ε-martensite was not observed within the sampled area. Dark field images revealed a dominant austenite phase with the cellular dislocation structure seen in Figure 5.19a, while Figure 5.19b displayed a thin twin. Overall at ε_t=0.10, the microstructure consisted of a cellular dislocation structure with intersecting deformation bands and stacking faults, with a few twin boundaries in a parent austenite matrix.

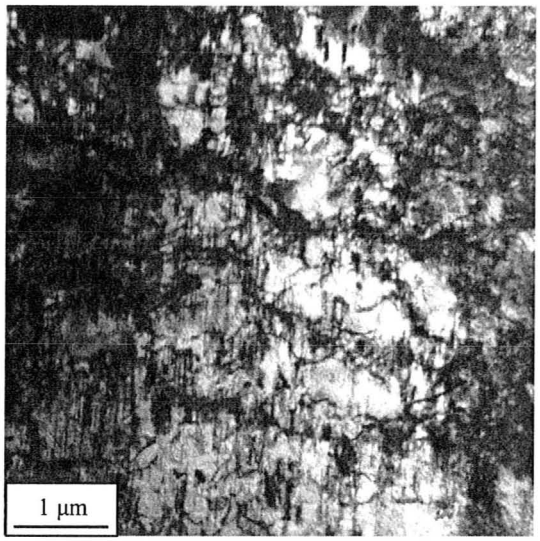

a) Dislocation Cell Structure

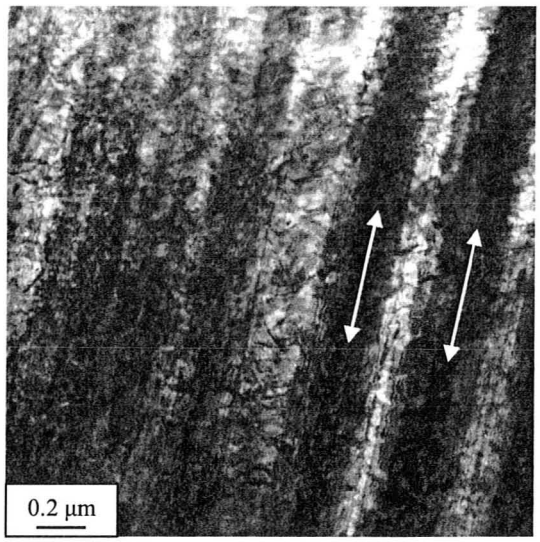

b) Deformation Bands

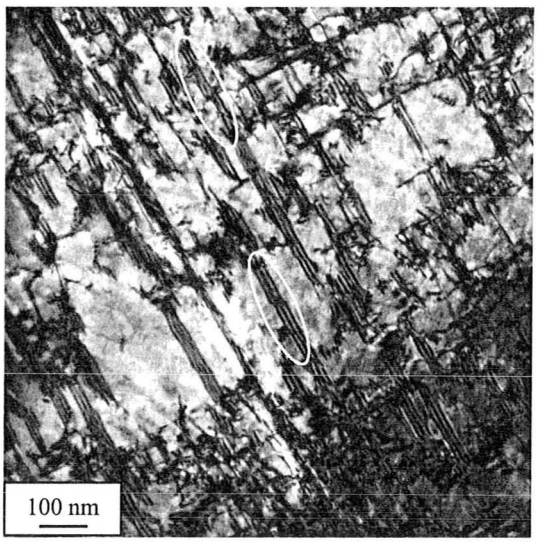

c) Dislocation – SF Interaction

Figure 5.18 TEM BF Images of Deformation Bands and SFs at ε_t=0.10 for 0.4C Alloy

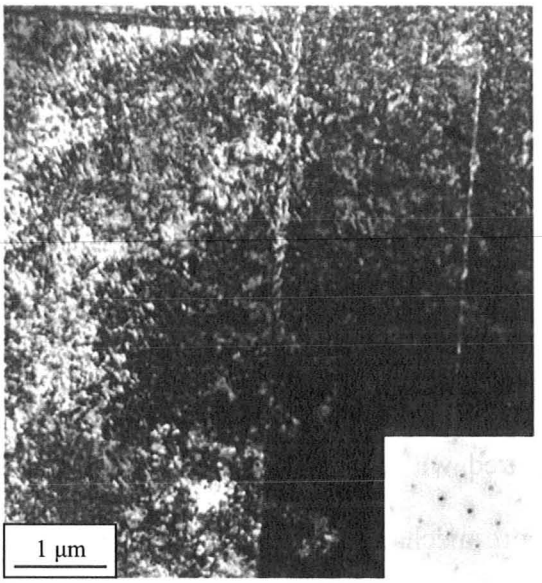

a) BF Image

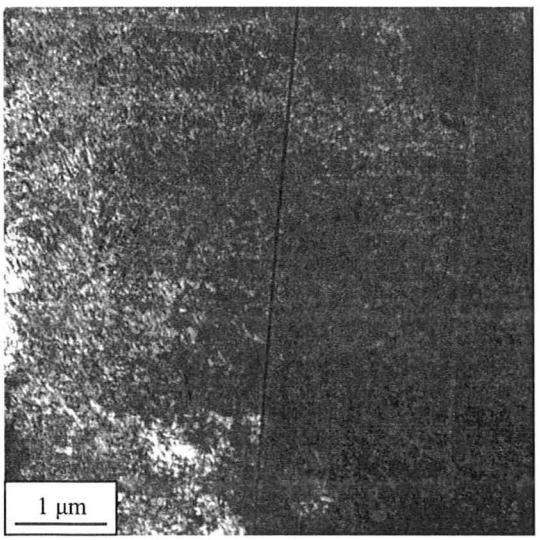

b) DF Image - Austenite Phase

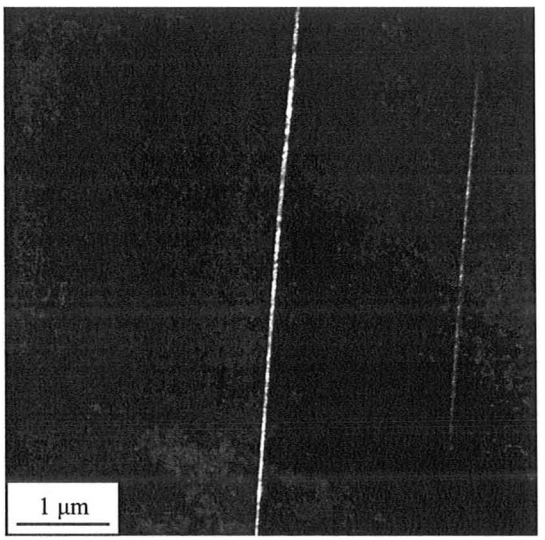

c) DF Image - Twin Boundary

Figure 5.19 TEM BF- DF Images of Austenite and Twin at ε_t=0.10 for 0.4C Alloy

As true strain was increased to 0.30, EBSD phase maps (Figure 5.17c) revealed numerous deformation products with the largest portion being twin boundaries with approximately 10% ε-martensite from XRD analysis (Figure 5.13). TEM analysis

revealed more detailed information on the dislocation microstructure at this higher strain level. The cellular dislocation structure was still observed (Figure 5.20) with higher dislocation density compared to images at the ε_t=0.10. A TEM composite image (Figure 5.21) was made by overlaying various images and showed two sets of interacting deformation bands at ε_t=0.30. Using dark field imaging, the bright field image of Figure 5.22a revealed a heavily deformed structure with both austenite and fine twins (Figure 5.22b-c). When compared with the ε_t=0.10 microstructure (Figure 5.19), the ε_t=0.30 showed significantly more mechanical twins which was consistent with the EBSD maps (Figure 5.17) where mechanical twinning was seen to increase with applied strain. The parent austenite phase continually created mechanical twins and no significant ε-martensite was observed within the TEM sample area.

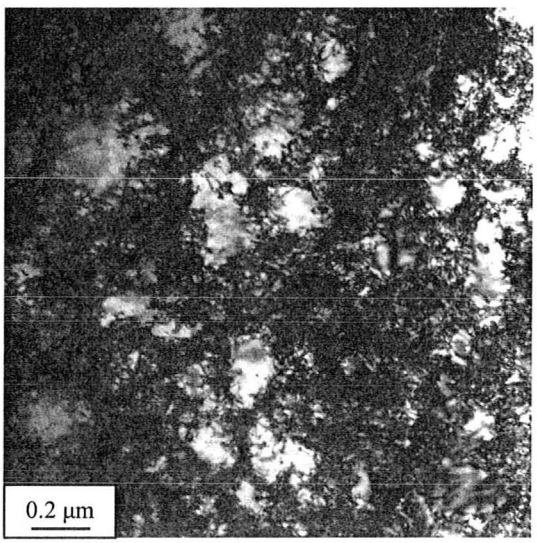

Figure 5.20 TEM BF Image of Dislocation Cell Structure at ε_t=0.30 for 0.4C Alloy

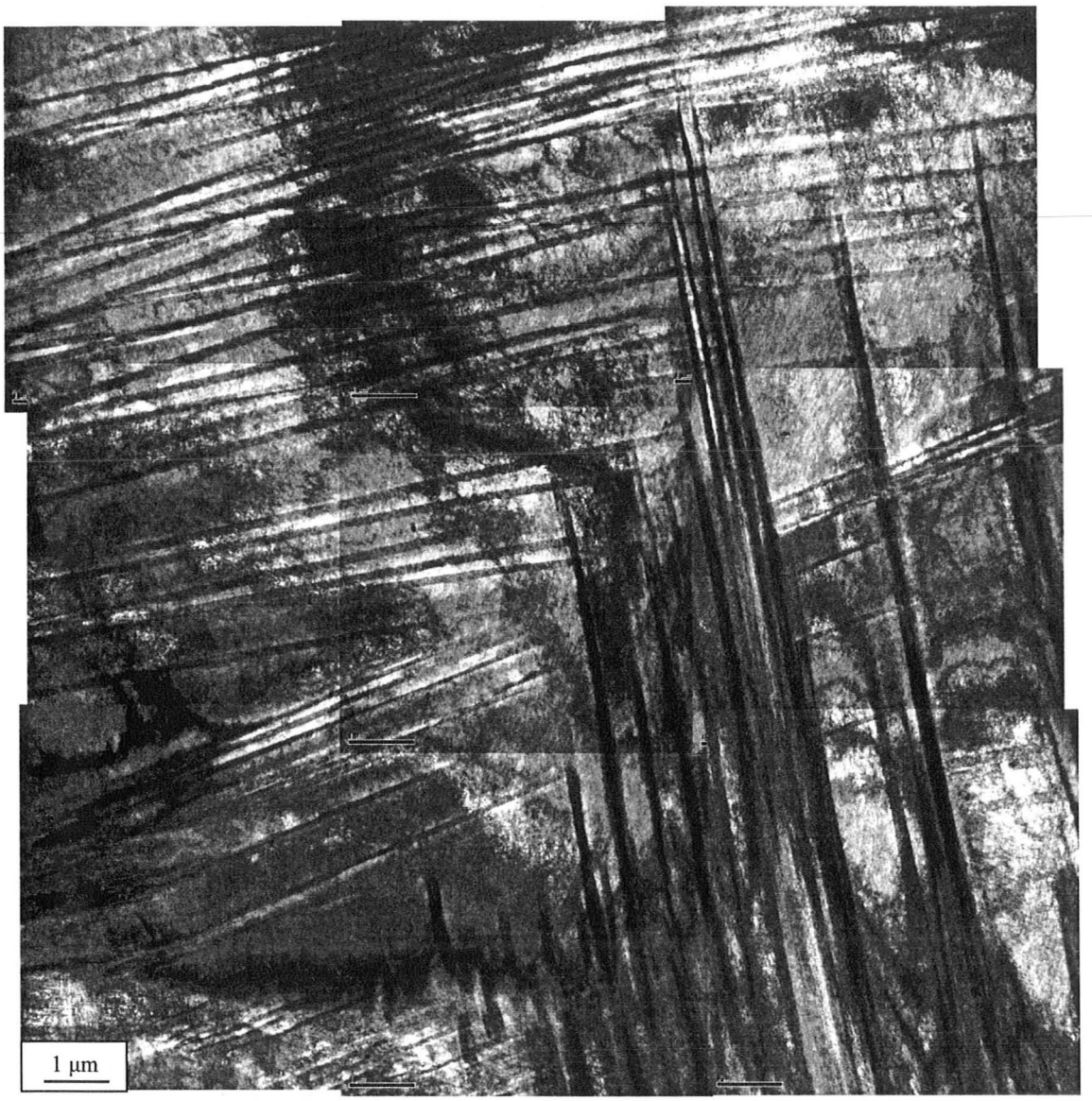

Figure 5.21 TEM Composite BF Image of Intersecting Deformation Bands at ε_t=0.30 for 0.4C Alloy

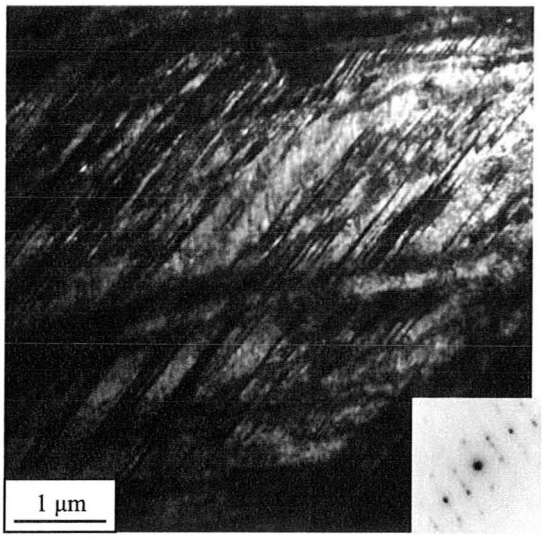

a) BF Image of Deformed Grain

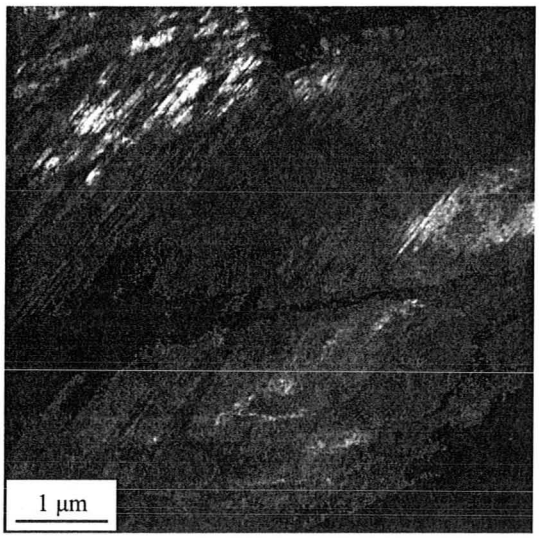

b) DF Image of Austenite Phase

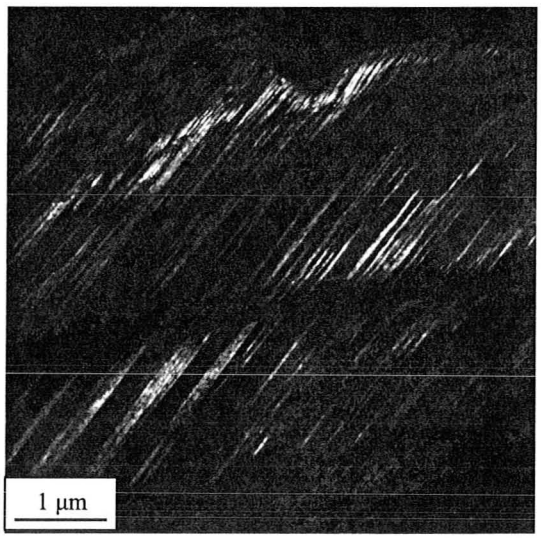

c) DF Image of Twins

Figure 5.22 TEM Image of Deformed Microstructure at ε_t=0.30 for 0.4C Alloy

5.5 0.2C Alloy Microstructural Evolution vs. Strain

This section will present the results from the experiments performed on the 0.2C alloy. Microstructural evolution as a function of strain was analyzed and microstructural images, EBSD phase maps, and TEM analysis will be presented to reveal information on the deformation mechanisms and microstructural development of this alloy.

5.5.1. SEM Observations

The microstructural evolution as a function of true strain for the 0.2C alloy was observed by SEM at various strain values to determine the progression of transformation products and phases as well as regions of deformation. The microstructural evolution seen in Figure 5.23a-d revealed significant transformation during deformation and when compared with the XRD analysis (Figure 5.13), most of transformation products were ε-martensite. Initially (Figure 5.23a) the microstructure consisted of a dual phase microstructure of austenite and ε-martensite. As 0.10 true strain was reached, deformation products were evident in most grains (Figure 5.23b), and stopped at grain boundaries. There was some interaction between different transformation products within the grains. At ε_t=0.33 (fracture), the microstructure observed in Figure 5.23c-d showed heavily deformed grains with transformation products consuming all grains. Various sets of transformation products were seen to overlap each other and grain boundaries were difficult to distinguish.

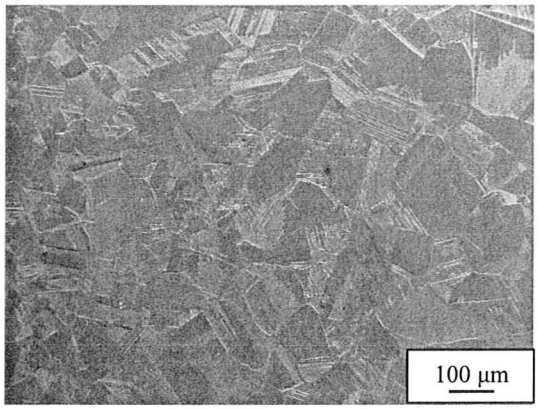

a) Annealed Microstructure, ε_t=0.0

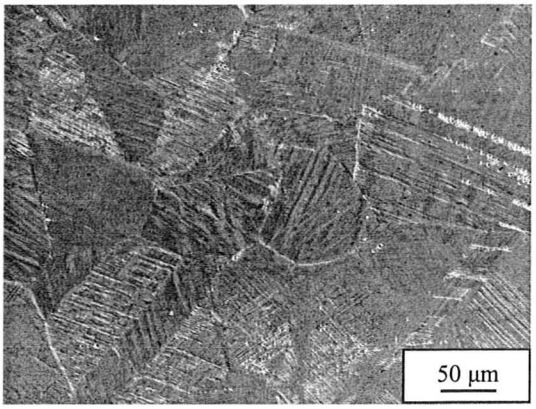

b) ε_t=0.10

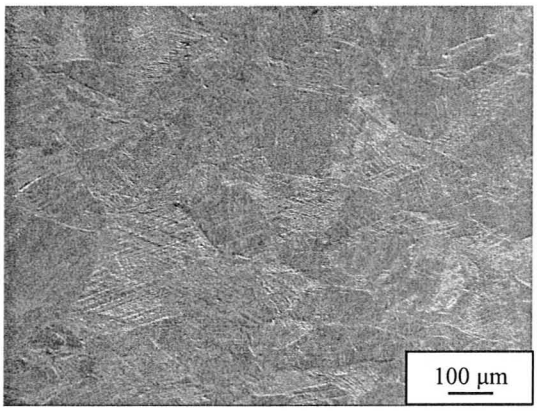

c) Fracture Microstructure, ε_t=0.33

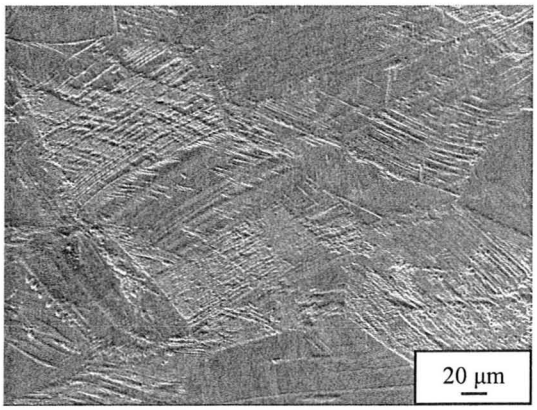

d) Magnified View of ε_f=0.33

Figure 5.23 SEM Microstructural Evolution as a Function of Strain for 0.2C Alloy

5.5.2. EBSD Phase Maps

With the microstructural images showing information on the microstructural evolution versus strain, EBSD phase maps were made to determine the identity of deformation products. The as-annealed microstructure of the 0.2C alloy previously viewed in Figure 5.3, contained an austenite matrix, thermal ε-martensite and annealing twins. As ε_t=0.05 (Figure 5.24a), ε-martensite platelets were transformed from the austenite matrix and occurred in random orientations with annealing twins still evident.

Figure 5.24b shows the phase map at 0.10 true strain for the 0.2C alloy, with a significant increase in the amounts of ε-martensite being observed, with large platelets intersecting other ε-martensite plates. As higher levels of deformation were reached at 0.20 true strain, (Figure 5.24c) large portions of austenite were transformed to ε-martensite with whole grains of ε-martensite. At fracture, shown in Figure 5.24d, the microstructure contained larger amounts of ε-martensite with regions of austenite. A few annealing twins were observed within the various maps and were not seen to increase as a function of strain. The EBSD phase maps correlated with the XRD data (Figure 5.13), where the production of ε-martensite began at low strain levels. A significant amount of ε-martensite was produced as true strain reached 0.10 and further ε-martensite was produced as true strains reached 0.30 and fracture. XRD revealed a consistent or small increase in the amount of ε-martensite from ε_t=0.10 to fracture, which was not detected to the same degree with the phase maps. From EBSD analysis alone, the maps could not quantify the amounts of austenite and ε-martensite as the chosen mapping area may not have been representative of the entire sample, as would be the case for XRD. From both the EBSD phase maps and the XRD data, the primary mode of deformation within the 0.2C alloy was the production of ε-martensite, resulting in a TRIP alloy.

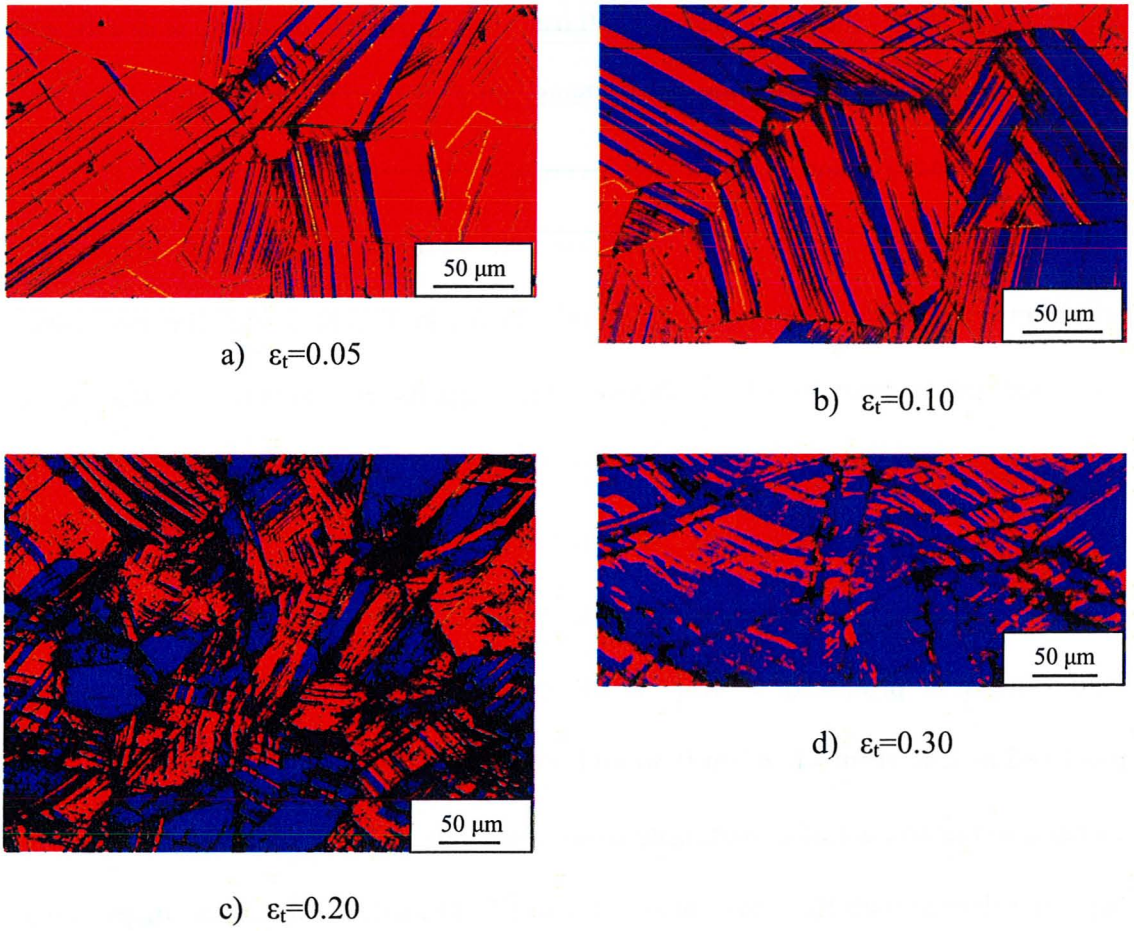

a) ε_t=0.05

b) ε_t=0.10

c) ε_t=0.20

d) ε_t=0.30

Figure 5.24 EBSD Phase Mapping of Microstructure for 0.2C Alloy

5.5.3. TEM Analysis

The microstructure was analyzed using the TEM with BF and DF images to observe dislocation, SFs, austenite, and ε-martensite interactions. With the 0.2C alloy consisting of austenite and ε-martensite, the dislocation interaction was not similar to the 0.4C TEM observations and previous results on the 0.6C alloy. At 0.05 true strain, dislocations and SF overlap were observed as shown in Figure 5.25a. Interaction between deformation bands, SFs and ε-martensite was also observed at this low deformation, (Figure 5.25b), where ε-martensite and deformation bands ran vertically and stacking

faults were found between the bands. From BF and DF imaging, Figure 5.26a-c revealed finely dispersed ε-martensite platelets within an austenite matrix at 0.05 true strain. Figure 5.26a shows the BF image of the deformed grain, Figure 5.26b showed the DF image of the austenite regions and Figure 5.26c, revealed the fine ε-martensite between the regions of austenite.

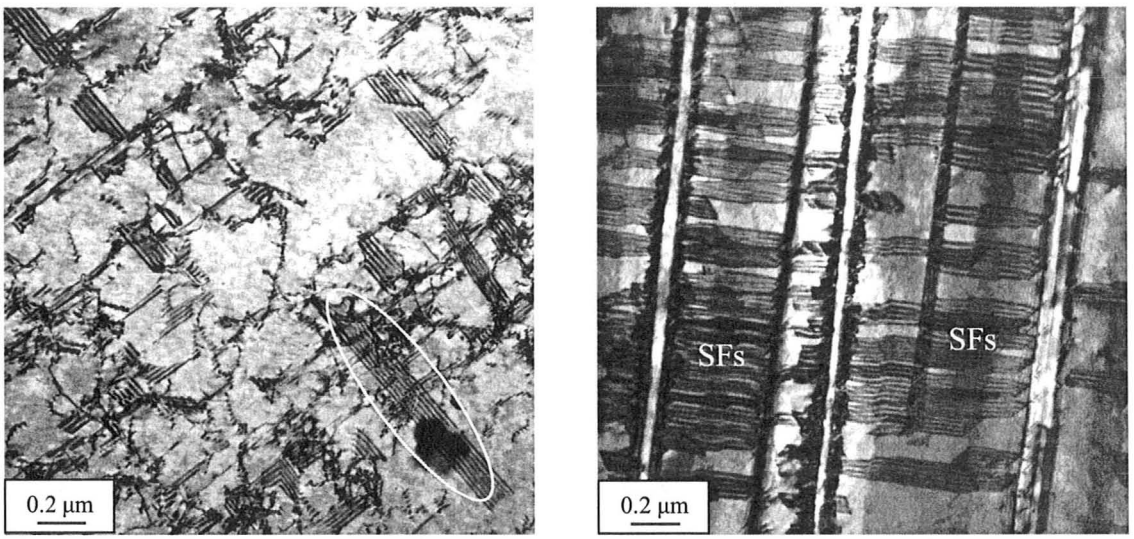

a) Dislocation – SF Interaction b) SF- ε-martensite Interaction

Figure 5.25 BF Dislocation, SF and ε-Martensite Interaction for ε_t=0.05 for 0.2C Alloy

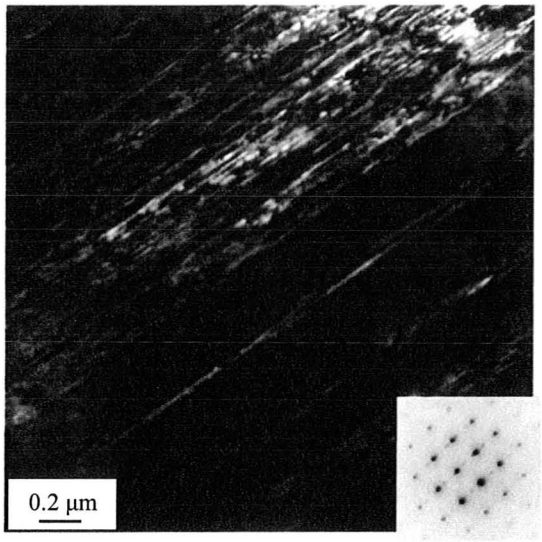

a) BF Image of Deformed Grain

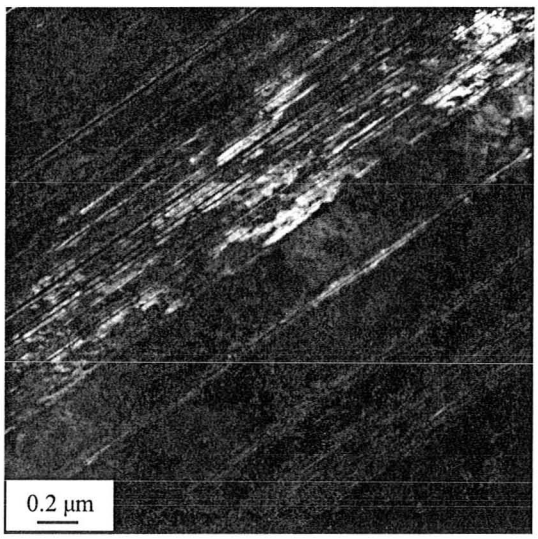

b) DF Image of Austenite Phase

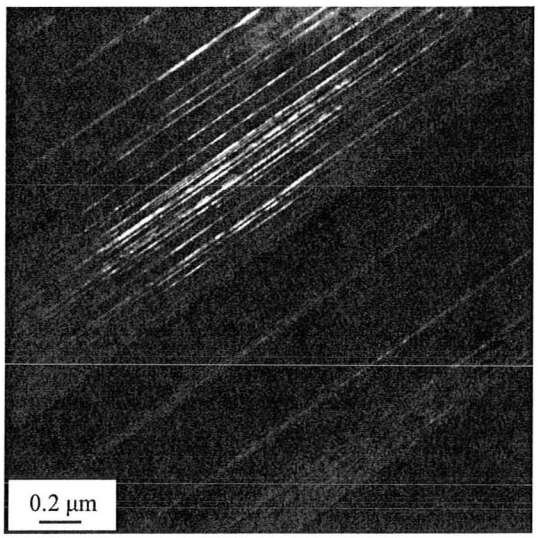

c) DF Image of ε-martensite

Figure 5.26 TEM Image of Deformed Microstructure at ε_t=0.05 for 0.2C Alloy

At 0.20 true strain; the microstructure revealed more regions of ε-martensite with intersection between platelets and bent ε-martensite platelets. The interaction between ε-martensite platelets is seen in Figure 5.27a, with ε-martensite plates in one direction

intersecting plates in another direction. This was also observed in Figure 5.27b where ε-martensite plates were found in different directions with bent sections. The bent sections were probably the result of dislocations traveling through the ε-martensite, shearing the ε-martensite and creating bent sections. Bent ε-martensite was also observed by Liang (Liang 2008) for the Fe-24Mn alloy. Thin plates of ε-martensite were seen to exist between regions of austenite as observed by Figure 5.28a-c, where the BF image displayed bent platelets and DF images of austenite and ε-martensite thinly distributed within the austenite.

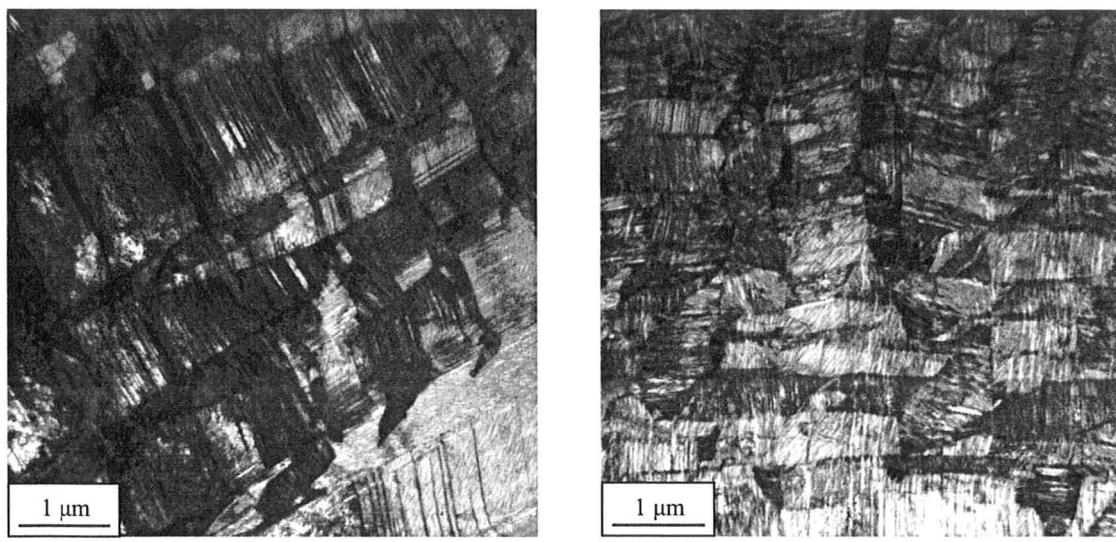

a) ε-Martensite Interaction b) Bent ε-Martensite

Figure 5.27 TEM BF Image of ε-Martensite Interaction at ε_t=0.20 for 0.2C Alloy

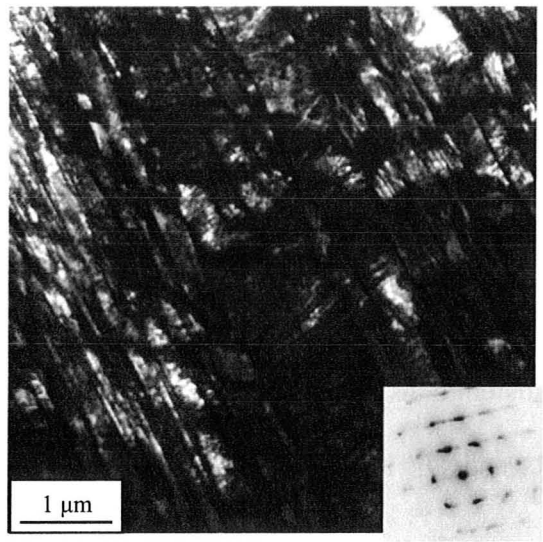

a) BF Image of Deformed Microstructure with Bent Platelets

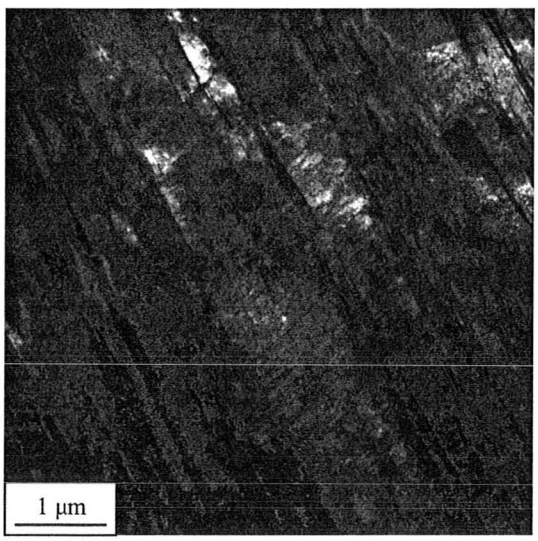

b) DF Image of Austenite Phase

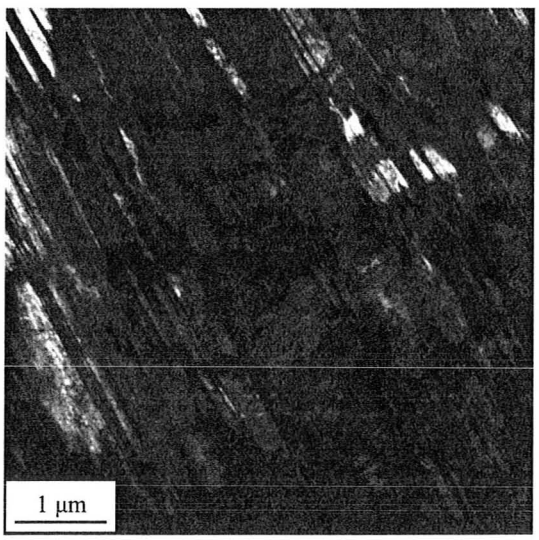

c) DF Image of Bent ε-Martensite

Figure 5.28 TEM Image of Deformed Microstructure at ε_t=0.20 for 0.2C Alloy

5.6 Fracture

From the monotonic tensile test to fracture, the fracture surface area and load at fracture were used to calculate the fracture stress and strain, which were then plotted alongside the corresponding true stress - strain curves in Figure 5.29. The connection between the point of uniform elongation and fracture stress – strain were connected with a dotted line for analysis purposes only. The 0.6C alloy exhibited the highest fracture strength and strain when compared with the other two alloys. For this alloy, the average fracture stress was 2074 MPa, and the approximate fracture strain being 0.93.

The 0.4C fracture stress was 1248 MPa and fracture strain 0.60, (a 20% post-uniform elongation). When compared with the other alloys, it was observed that the 0.4C alloy had a lower fracture stress and strain than the 0.6C alloy and a higher fracture stress and strain than the 0.2C alloy.

Fracture stress and strain was calculated and plotted for the 0.2C alloy, with the TRIP alloy having a 3% post-uniform elongation and fracture stress averaging 1075 MPa. The presence of softer austenite and harder ε-martensite, likely led to a more brittle failure compared to the ductile 0.4C and 0.6C alloys.

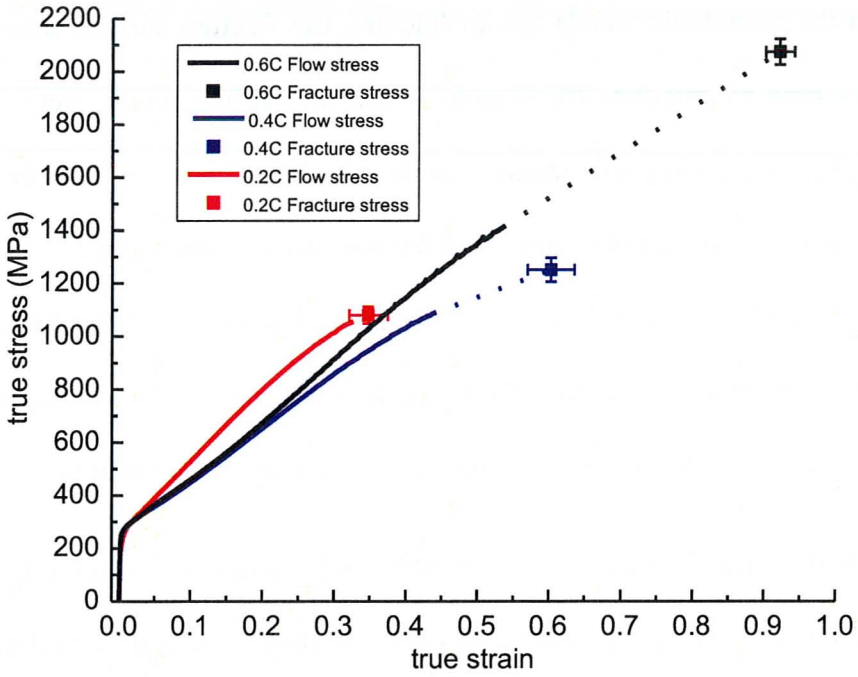

Figure 5.29 Fracture Stress - Strain for All Alloys

5.6.1. 0.6C Alloy

SEM micrographs were taken of the fractured thickness section to understand the damage mechanism. Figure 5.30a shows the necked fracture region with elongated grains, and a visibly deformed microstructure with twins. A magnified version (Figure 5.30b) revealed the region below the fracture surface. Triaxial tension in the necked region resulted in the presence of voids along striations in the necked region and was a factor in the failure of the 0.6C alloy. Other features observed in Figure 5.30a-b displayed grain boundary separation and decohesion of inclusions in the uniform elongation region, making them damage initiation sites.

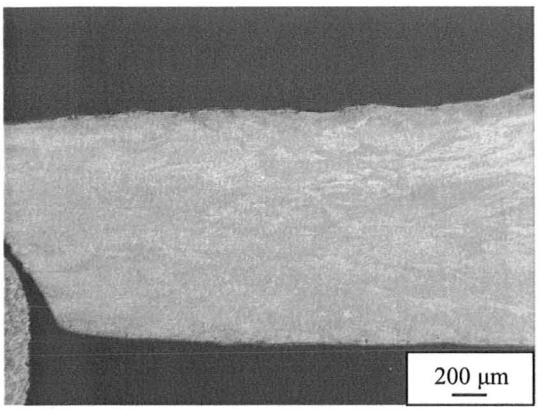

a) Necked region

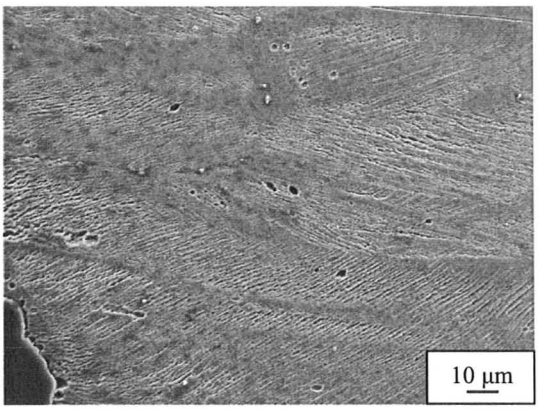

b) Magnified Image of Necked Region

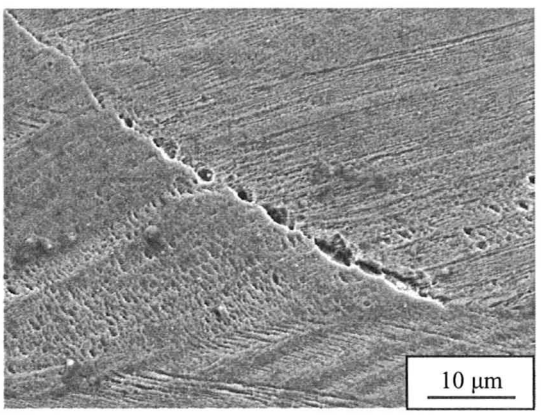

c) Grain Boundary Separation

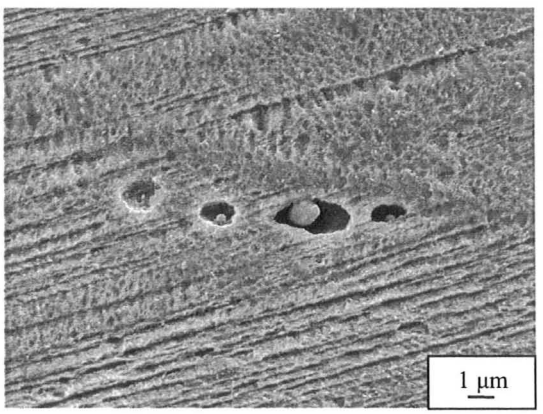

d) Voids and Decohesion of Inclusions

Figure 5.30 SEM Fracture Features in 0.6C Alloy

The fracture surface (Figure 5.31) was examined to observe features that were present in this region of highly concentrated stress and determine the main damage mechanism. The fracture surface showed classic cup-cone features, void formation and decohesion of inclusions which indicated a ductile fracture mechanism. Voids observed in Figure 5.30b were still present in Figure 5.31 with other features also prominent such as a few micro-cracks and ductile cup-cone marks. Dislocation pile ups concentrated

large stress at the grain boundaries and this led to grain boundary decohesion as the main damage mechanism within the 0.6C alloy.

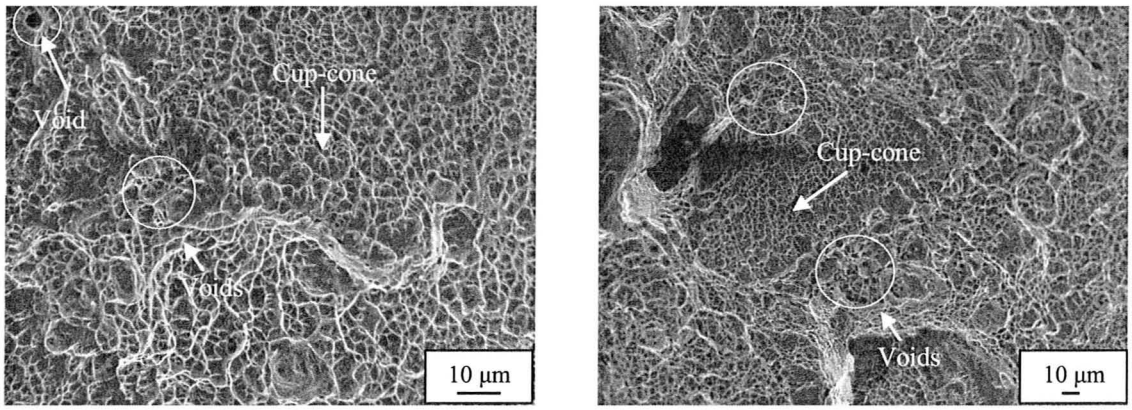

Figure 5.31 SEM Fracture Surface Cup-Cone Morphology and Voids in 0.6 Alloy

5.6.2. 0.4C Alloy

The fracture specimen was sectioned in the longitudinal direction to determine which fracture features would be dominant in this alloy with a knowledge of the deformation products and phases, i.e. austenite, ε-martensite and twin boundaries. The necked region within the sample (Figure 5.32a-b) revealed significant deformation, elongated grains and high angle ductile fracture. Another feature observed was the separation along a striation at either an ε-martensite platelet or a twin boundary, Figure 5.32c shows void formation along a specific striation. The boundary separation arose from dislocation pile-up at boundaries or twins and led to weak regions of high stress, and initiation sites for failure. Figure 5.32d revealed void formation and decohesion of inclusions, similar to that observed for the 0.6C fracture microstructure.

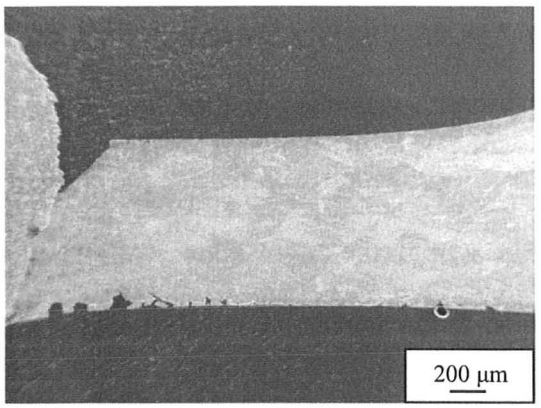

a) Necked Region

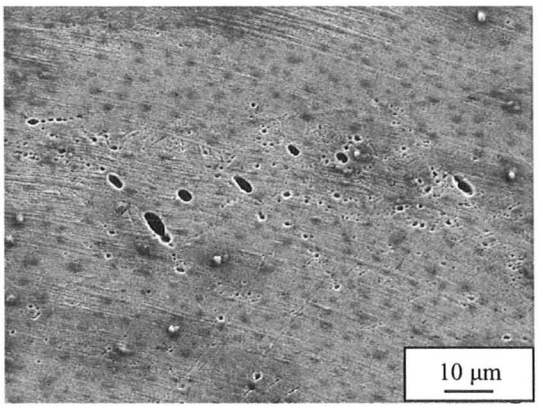

b) Magnified Image of Necked Region

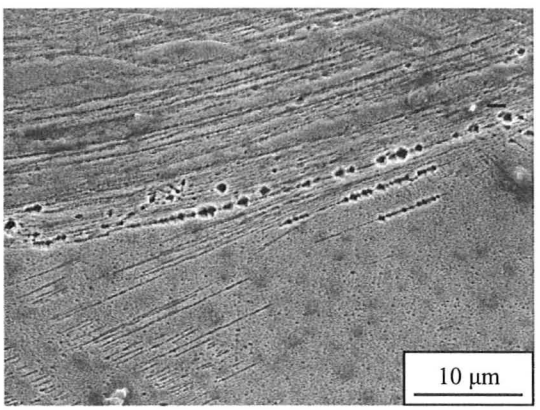

c) Separation along a Striation

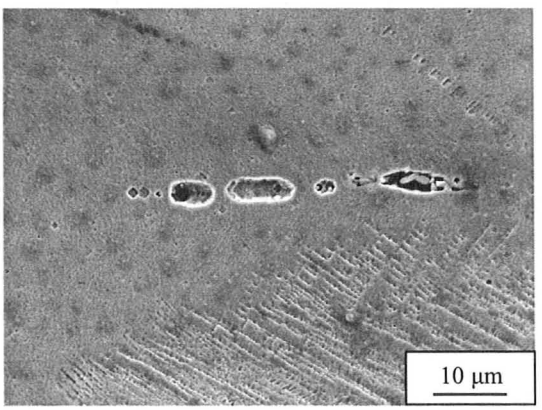

d) Void and Decohesion of Inclusions

Figure 5.32 SEM Fracture Features in 0.4C Alloy

With a post-uniform elongation of 20%, the fracture was considered relatively ductile so the failed fracture surface was examined to confirm this. Void formation and cup-cone features (Figure 5.33a-b) were found to be predominant on the surface and these features were indicators of ductile fracture. Regions of cleavage failure and micro-cracks in Figure 5.33c-d, were also observed giving rise to regions of brittle failure. These features agreed with the presence of a hard ε-martensite phase found from XRD analysis. With the small presence of ε-martensite found from XRD and EBSD analysis, the fracture

stress - strain (Figure 5.29) of the 0.4C alloy was significantly lower than the 0.6C of a similar microstructure. The presence of ε-martensite was seen to decrease the fracture stress – strain, as well as act as a region of stress localization, and limited the strength of the material. The likely damage mechanism within the 0.4C alloy would be void nucleation at ε-martensite plate interfaces, similar to the damage events observed by other TRIP alloys (Liang 2008).

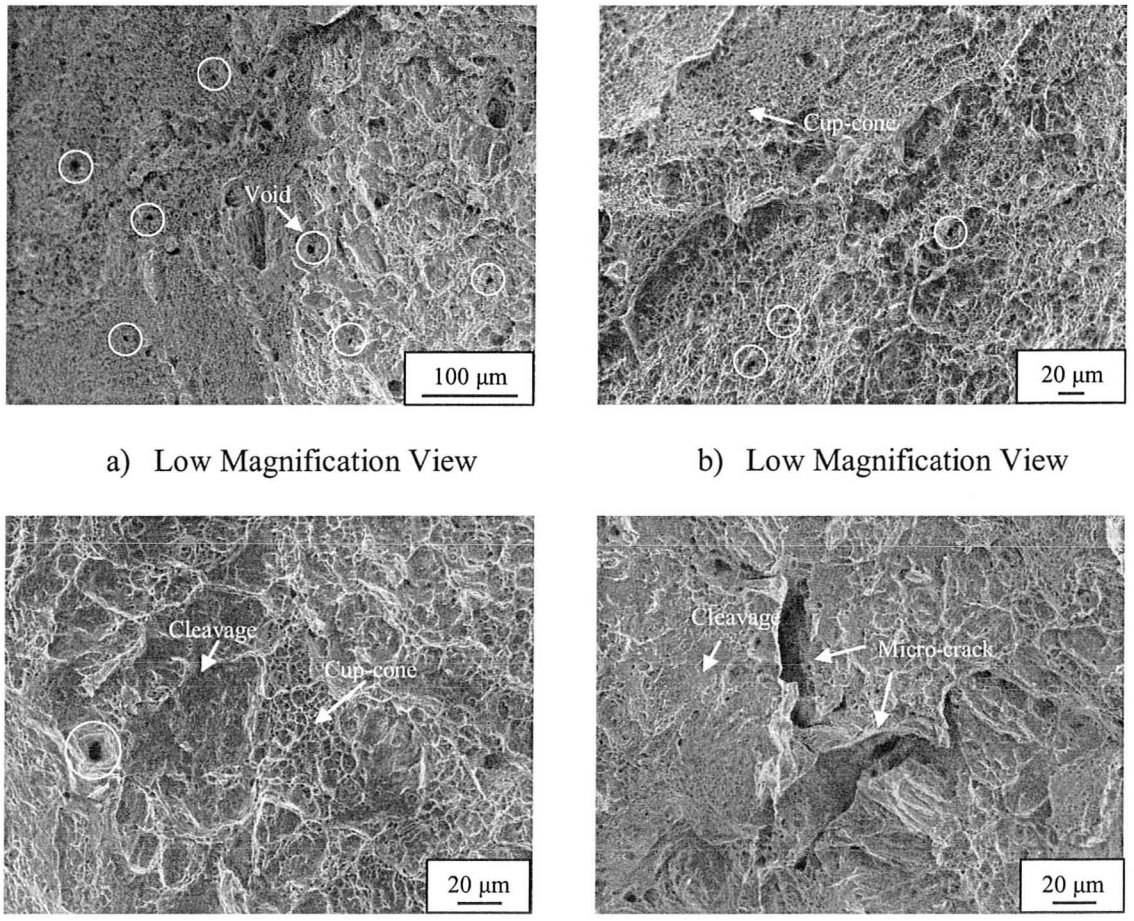

a) Low Magnification View

b) Low Magnification View

c) Higher Magnification View

d) Micro-crack

Figure 5.33 SEM Fracture Surface in 0.4C Alloy

5.6.3. 0.2C Alloy

Damage features that lead to failure in the 0.2C alloy was analyzed with interface separation being evident in Figure 5.34a, with the deformation products separating from the parent matrix. The boundaries of deformation products and the parent austenite matrix were regions of localized stress and led to void coalescence and boundary separation. Voids were also observed in this region with Figure 5.34b displaying void coalescence, as well as large regions of deformation. Grain boundaries became less defined as deformation increased to fracture with various striations and voids present in the microstructure (Figure 5.34c-d). From XRD analysis (Figure 5.13) and EBSD maps (Figure 5.24), ε-martensite was the primary transformation product and was seen to occupy large amounts of the microstructure at fracture. The striations and platelets observed in Figure 5.34c-d were a result of void formation occurring at the intersection of ε-martensite platelets with the austenite matrix.

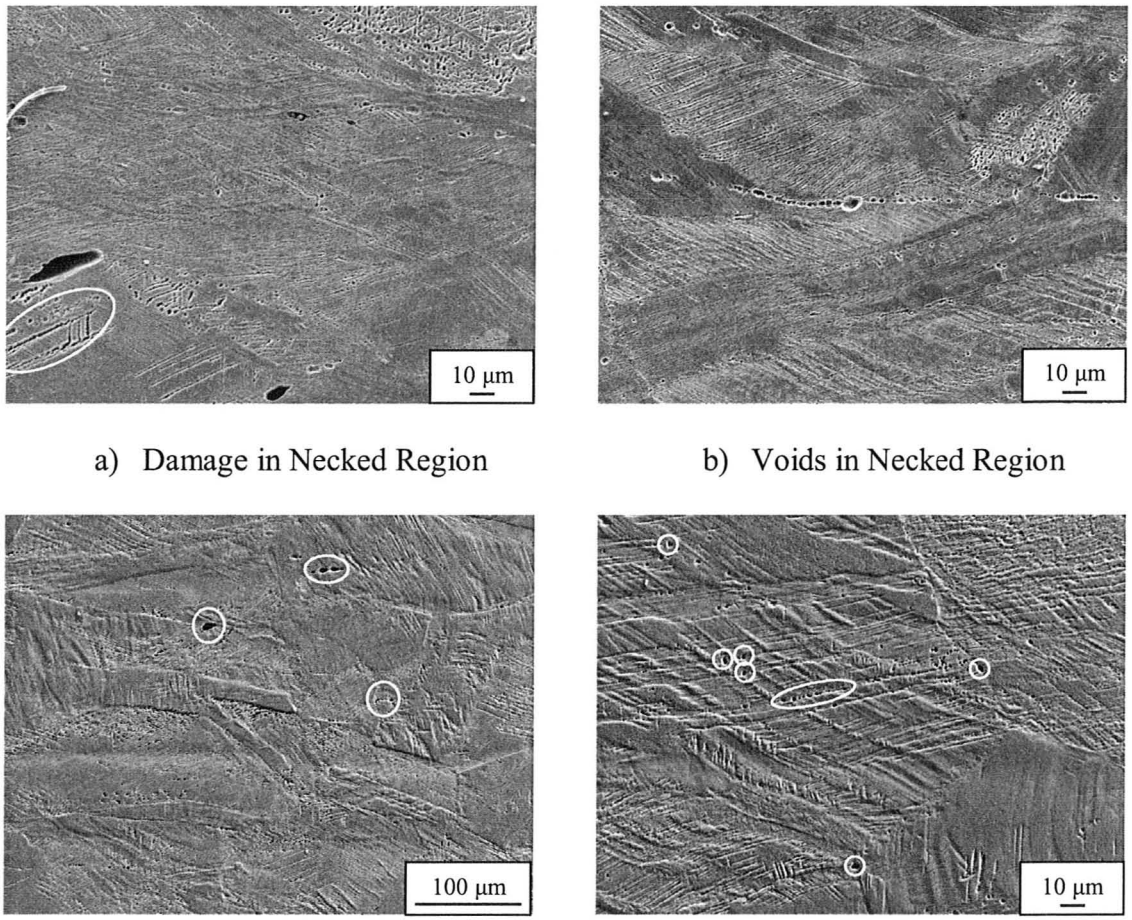

a) Damage in Necked Region

b) Voids in Necked Region

c) Microstructural Damage

d) Voids in Fracture Microstructure

Figure 5.34 SEM Fracture Features in 0.2C Alloy

The fracture surface was also examined in the 0.2C alloy and Figure 5.35a-d displays various features found on the surface, with micro-cracks, voids, cup-cone dimples and cleavage failure. When compared with the other more ductile alloys, a noticeable difference in this fracture surface was the amount of cleavage failure. The 0.2C alloy showed more cleavage regions compared to the 0.4C and 0.6C alloys and these regions indicated more brittle failure. With the dominance of the ε-martensite transformation product, interface separation between platelets or grains of ε-martensite

and austenite would lead to a more brittle fracture. Interface or grain boundary separation was the main damage mechanism, with the presence of ε-martensite leading to areas of brittle fracture.

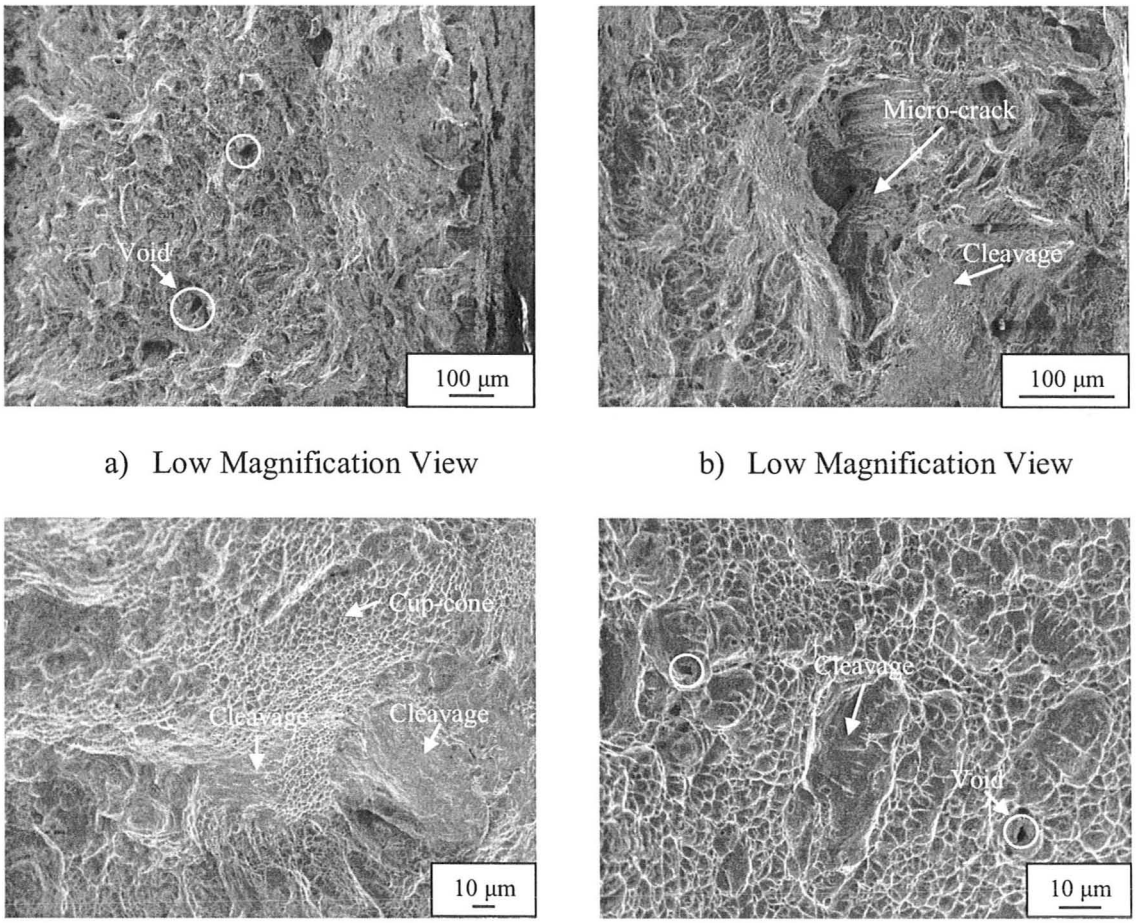

a) Low Magnification View

b) Low Magnification View

c) Higher Magnification View

d) Higher Magnification View

Figure 5.35 SEM Fracture Surface in 0.2C Alloy

6. DISCUSSION

This chapter discusses the mechanical property and microstructural evolution findings of the 0.6C, 0.4C and 0.2C alloys. Each alloy is first summarized and discussed in detail before proceeding to general discussions on various effects (such as carbon content), comparisons and the modeling of mechanical behaviour.

6.1 0.6C Alloy Summary and Analysis

The various experiments conducted to examine the 0.6C alloy revealed an austenite matrix and annealing twins (Figure 5.1) for the undeformed microstructure, with TEM analysis of a similar Fe-22Mn-0.6C alloy by Wang (Wang 2009) revealing a similar austenite microstructure (Figure 2.22). The SFE phase prediction by Allain et al. (Allain 2004b) with SFE = 37.2 mJ/m^2 (Nakano 2010) was correct in predicting an initial austenite matrix, and deformation by combined dislocation glide and mechanical twinning. Upon deformation, mechanical twins were produced as transformation products, as seen by the EBSD phase maps (Figure 5.15). XRD analysis (Figure 5.13) revealed no initial presence of ε-martensite and no significant ε-martensite production during tensile deformation, consistent with the EBSD phase mapping. TEM observations at 0.20 true strain by Wang (Wang 2009) revealed the structure seen in Figure 2.23 with BF and DF images containing mechanical twins dispersed throughout the matrix and dislocation network cells. Twins were finely dispersed within the microstructure with many micro-twins observed, correlating with the microstructure observed and EBSD maps in Figure 5.16 and Figure 5.17, respectively. The alloy used by Wang was identical in composition to the present alloy with a different annealing treatment, yet produced

results that matched the microstructural evolution seen by the 0.6C alloy. The 0.6C alloy was classified as typical TWIP steel and this microstructural evolution was consistent with observations by previous authors with the same alloy composition (Allain 2004a, Allain 2004b, Barbier 2009, Gutierrez-Urrutia 2010, Hamada 2010, Scott 2005).

Linking the microstructural evolution with the mechanical behaviour of this alloy, the 0.6C alloy exhibited high strength and ductility reaching a UTS of 1407 MPa and maximum true uniform elongation of ~0.53. The work hardening curve (Figure 5.8) exhibited an increase at 415 MPa (~0.10 true strain) due to the onset of twinning, with the introduction of new dislocation barriers which inhibited dislocation movement and dynamically refined the grain size. An onset of twinning was also seen by Bouaziz et al. (Bouaziz 2008) for Fe-22Mn-0.6C at 550 MPa (~0.10 true strain).

The increase in work hardening was observed from 415 MPa until approximately 1000 MPa (~0.34 true strain) and was attributed to significant mechanical twinning within this range of true strain. The onset of mechanical twinning allowed kinematic hardening (Figure 5.10) to contribute significantly to the overall flow stress. At stresses greater than 1000 MPa (~0.34 true strain), the work hardening rate remained relatively constant up to fracture. The further production of twin boundaries did not benefit the work hardening due to the higher dislocation density in the structure, making the introduced barriers less effective. The structure was saturated with dislocations and subsequent twin formation was not as beneficial to the work hardening rate, similar to TEM analysis of a 70% cold-rolled Fe-22-0.6C alloy by Wang (Wang 2009) which revealed a dense dislocation structure. The kinematic hardening trend past 0.30 true

strain was not explored but would be expected to taper off at 0.34 true strain in overall flow stress contribution, due to microstructural saturation.

An interesting feature of the stress-strain curve of the present alloy is the observation of striations in both the tensile and work hardening plots. These have been previously observed by other authors discussing TWIP alloys (Allain 2004a, Allain 2004c, Grassel 2000, Chen 2007, De Cooman 2009) and are often not commented on or discussed in-depth. The majority of authors attributed the serrations to the Portevin-LeChatelier (PLC) effect with a negative strain rate sensitivity, or dynamic strain aging (DSA). DSA is an aging process related to the fast movement of solute atoms during deformation, with the dislocation velocity similar to solute mobility (Dastur 1981). Within high-Mn TWIP steels, C-Mn pairs may reorient themselves and pin the dislocation. The pinned dislocation increases the local stress before the dislocation breaks down, causing the serrations and PLC effect (Chen 2007, Kim 2009, De Cooman 2009). From these serrations, large fluctuations were observed in the work hardening rate until fracture.

The fracture of the 0.6C alloy resulted in a 40% post-uniform elongation with the maximum uniform elongation being 53% (Figure 5.29), indicating ductile failure. The steady ability to create twins allowed the microstructure to continually introduce barriers for dislocation motion, increasing the strength and delaying the onset of necking. Another benefit in this alloy was the lack of ε-martensite which would limit the ductility. From observing the fracture features and examining the fracture surface (Figure 5.31), a highly ductile fracture was observed with a highly necked region and dominant cup-cone

features. Twin and grain boundaries acted as stress concentrators due to dislocation accumulation along the boundary lines. The concentrated stress at these sites created grain boundary separation and was the critical damage event.

6.2 0.4C Alloy Summary and Analysis

The microstructural evolution of the 0.4C alloy during deformation was observed and analyzed. Initially, the microstructure contained austenite with annealing twins (Figure 5.2) as predicted by SFE phase maps (SFE = 33.4 mJ/m^2). As deformation began, EBSD phase maps revealed mechanical twins and strain-induced ε-martensite within the microstructure (Figure 5.17), with the volume fraction of deformation products increasing with increased strain. XRD analysis supported these findings with ε-martensite production at low strains, which saturated at 0.20 true strain (Figure 5.13). The largest amount of ε-martensite was produced between 0.10 and 0.20 true strain. Deformation products (twins and ε-martensite) were seen to initiate at ~415 MPa or 0.10 true strain. TEM analysis revealed dislocation accumulation and stacking faults within the structure and fine dislocation networks. The microstructure at fracture contained both mechanical twins and ε-martensite as deformation products, indicating the deformation mechanism as both TWIP and TRIP, agreeing with the SFE predictions for the deformation products within the 0.4C alloy. The 0.4C alloy was similar in composition to Lü's Fe-22 wt%Mn-0.376 wt%C alloy (Lü 2010) with a calculated SFE of 32.6 mJ/m^2, with Lü's alloy being cold-rolled and producing larger amounts of ε-martensite. Twinning was less evident in Lü's alloy than the 0.4C alloy, with ε-martensite production being dominant. Both alloys displayed TWIP and TRIP effects.

The mechanical properties of the 0.4C alloy were lower in total strength and ductility compared to the 0.6C alloy, with an average UTS of 1040 MPa and uniform elongation of ~0.40. An increase in work hardening (Figure 5.8) was observed at 360 MPa (~0.06 true strain) until 670 MPa (~0.20 true strain) due to the formation of deformation products, correlating well with XRD data on the production of ε-martensite from 0.10 to 0.20 true strain (Figure 5.13) and mechanical twinning observed by EBSD phase maps at 0.10 true strain (Figure 5.17). Both twins and ε-martensite acted as barriers for dislocation motion, decreased the mean free path, thus increasing the work hardening rate. Serrations were also observed in the tensile behaviour of the 0.4C alloy with fewer serrations compared with the 0.6C alloy. The lower carbon content in the 0.4C alloy decreased the C-Mn interaction and the DSA effect.

Once a true stress of 670 MPa (~0.20 true strain) was reached, the work hardening decreased continually until fracture, with the alloy unable to create effective barriers for preventing dislocation motion. Correlating with the microstructure at 0.20 true strain, the XRD analysis revealed ε-martensite saturation with no additional ε-martensite produced after 0.20 true strain. The kinematic hardening (Figure 5.11) was seen to contribute significantly to the overall flow stress and began saturating at 0.20 true strain. With the back stress trend for ε_t>0.30 not explored, the thought was that the kinematic hardening contribution would begin saturating in relation to the overall flow stress. Mechanical twins were still being created after 0.20 true strain (Figure 5.17), with the saturation of ε-martensite after 0.20 true strain.

The 0.4C and 0.6C alloy were similar in initial microstructure and both underwent mechanical twinning upon deformation. The 0.4C alloy produced ε-martensite at strains between 0.10 and 0.20 and saturation was observed at 0.20 true strain. The kinematic hardening contribution was limited with γ-ε interfaces acting as stress concentrators. Twins however, have a better ability to block dislocation motion and have a greater kinematic hardening potential, allowing the alloy to sustain higher work hardening rates. With the presence of ε-martensite within the 0.4C alloy, the work hardening rate was reduced due to dislocation accumulation at the γ-ε interface versus the 0.6C alloy only containing twins.

Failure analysis in this alloy yielded a 20% post uniform elongation (Figure 5.29). Examination of fracture features and of the fracture surface revealed various structures. A high angle fracture indicated a rather ductile fracture within the 0.4C alloy, with cup-cone features also supporting ductile fracture. Voids were seen in the fracture surface with a few micro-cracks and some regions of cleavage failure. Interface separation was observed between austenite and twins or ε-martensite within the microstructure. Examination of the fracture stress – stain of the alloys revealed lower strength and ductility of alloys with ε-martensite (0.4C and 0.2C alloys), both reaching a fracture stress of ~1100-1200 MPa. The 0.6C alloy had higher strength and ductility and did not contain ε-martensite, leading to the conclusion that decohesion was occurring at γ-ε interfaces and not twin boundaries. The separation along the austenite-ε-martensite interface with the nucleation, growth and linkage of voids was the primary damage mechanism associated with the 0.4C alloy. Though the alloy had a ductile fracture and mainly produced twins

upon deformation, ε-martensite was still present which likely limited the strength and ductility. The presence of ε-martensite was also seen to limit the strength of the Fe-24Mn alloy by Liang (Liang 2008) with tests at 298K and 77K both limited to ~1200 MPa. The tensile and mechanical behaviour of the 0.4C alloy was initially similar to the 0.6C alloy (TWIP) with the fracture likely being limited by the existence of ε-martensite (similar to the 0.2C alloy – TRIP) and the high dislocation density along the γ-ε interfaces.

6.3 Modeling 0.6C and 0.4C Mechanical Behaviour

The effect of chemical composition on the work hardening behaviour of TWIP Fe-Mn-C steels was investigated and a model was proposed by Bouaziz et al. (Bouaziz 2009). The model attempted to describe the mechanical behaviour as a function of chemical composition with the overall flow stress being comprised of various contributions and is discussed in detail in Section 2.6. The total stress was the sum of the yield stress (YS), and two other stress components seen in Equation 6.1. The first stress contribution (σ_1) described isotropic hardening due to dislocation accumulation and took the form of the Voce law seen in Equation 6.2. The second stress component (σ_2) was the contribution related to the kinematic hardening component as seen in Equation 6.3.

$$\sigma = YS + \sigma_1 + \sigma_2 \tag{6.1}$$

$$\sigma_1 = \frac{k}{f}[1 - \exp(-f\varepsilon)] \tag{6.2}$$

$$\sigma_2 = m\varepsilon^p \tag{6.3}$$

Values for the unknown variables such as k, f and p were taken as independent of chemical composition setting values at $k = 2900$ MPa, $f = 4$, and $p = 1.75$ (Bouaziz 2009). Fitting for m was taken as Equation (2.10) and was dependent on chemical composition. Combining equations 6.1 through 6.3, the overall flow stress was modeled and compared to the experimental true stress – strain behaviour.

Attempts to fit the work hardening behaviour of the 0.6C and 0.4C alloy to the model of Bouaziz et al. (Bouaziz 2009) required some alterations. The yield stress (YS) proposed in the model followed Equation 2.7 and yielded higher values than the present experimental yield stress for the 0.6C and 0.4C alloys. Thus, instead of using Equation 2.7, the measured YS from the experimental data was applied to Equation 6.1.

Another variation used in the present model was for predetermined variables k and f. The k and f values used in Equation 6.2 for work hardening in austenite were calculated from Liang's Fe-30Mn alloy (Liang 2008) with no carbon (Bouaziz 2009). However with the presence of carbon in larger quantities such as 0.6 wt% ad 0.4 wt% and less manganese, the predetermined values of k and f from Bouaziz et al. (Bouaziz 2009) were no longer suitable. As the variables (k and f) are for an austenitic microstructure without twinning, data from the 0.6C plastic regime (prior to the onset of twinning) was used. True stress – strain data from the 0.6C alloy was taken up until 0.10 true strain where twinning commenced, and compared with the Kocks and Mecking Voce Equation 2.4 (Kocks 2003) and Equation 6.2 to determine the k and f values of a Fe-22Mn-0.6C alloy prior to twinning. After integrating Equation 2.4 and rearranging the equation to follow the form of Equation 6.2, the Voce equation becomes Equation 6.4. The parameters used

were similar to the Equation 2.4 with θ as the work hardening rate, θ_0 as a constant and σ_v as a scaling stress.

$$\sigma - \sigma_y = \sigma_v \left[1 - \exp\left(\frac{-\theta_0 \varepsilon}{\sigma_v}\right)\right] \tag{6.4}$$

From there, a plot of θ-σ was made for the 0.6C experimental data in the plastic regime prior to twinning (Figure 6.1), to determine the x and y-intercepts as σ_v and θ_0, respectively. Parameters f and k were determined as functions of θ_0 and σ_v as seen in Equation 6.5 and Equation 6.6. Thus, it was determined that k = 2500 MPa and f = 2.08 and these values were compared with the values of Bouaziz et al. (Bouaziz 2009) in Table 6.1, with the modeled data fitting the present experimental data.

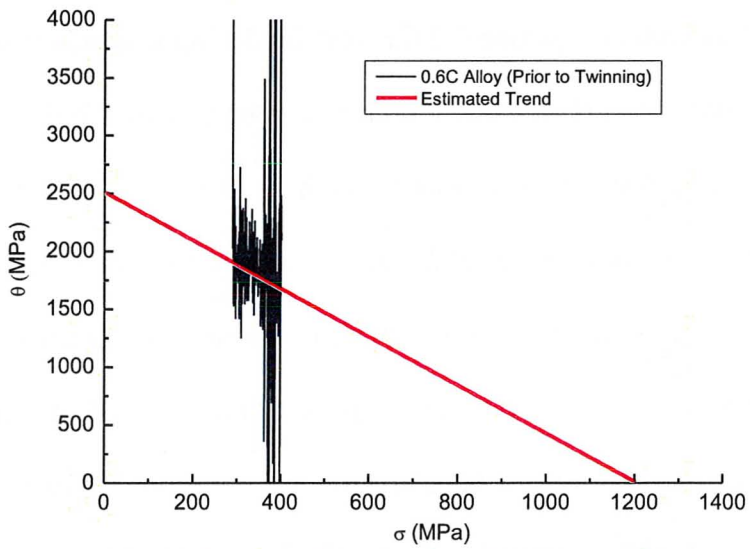

Figure 6.1 Kocks and Mecking Voce Equation for 0.6C Alloy

$$f = \frac{\theta_0}{\sigma_v} \tag{6.5}$$

$$k = \theta_0 \tag{6.6}$$

The model of Bouaziz et al. (Bouaziz 2009) reported the value *m*, to be linked with the SFE and to hold a relation with the chemical composition seen in Equation 2.10. When applied to the 0.6C and 0.4C alloy, the value did not yield a good fit to experimental tensile behaviour. Thus, the value of *m* was solved to yield the closest results to the experimental curve, which was 1001 for the 0.6C alloy and 374 for the 0.4C alloy. These values were compared with those of the Bouaziz et al. (Bouaziz 2009) model in Table 6.1.

Table 6.1 Parameter Values for 0.6C and 0.4C Alloy Tensile Property Model

Parameter	Bouaziz et al. (Bouaziz 2009) Model	Calculated Values for 0.6C and 0.4C
k (MPa)	2900	2500
f	4	2.08
p	1.75	1.75
m	1815 (0.6C) 1282 (0.4C)	1001 (0.6C) 374 (0.4C)

The modeled and experimental tensile behaviour for the 0.6C alloy was then plotted and can be seen in Figure 6.2 with the modeled behaviour closely reproducing the experimental tensile results. At low strain levels, the model overestimated the

experimental flow stress before reaching 0.35 true strain. The overestimation could have been due to the large grain size within the 0.6C alloy (150 μm), with the alloy behaving similar to single crystal deformation with dislocation glide with a large mean free path. The non-linear kinetics of twinning could have also been another contribution o the overestimation. After ε_t=0.35, significant twinning had dynamically refined the grain size, the model was not significantly different from the experimental flow stress. A reason for the disagreement between the model and experimental data at strains below 0.35, was that transformation dynamics were not considered or included in the model.

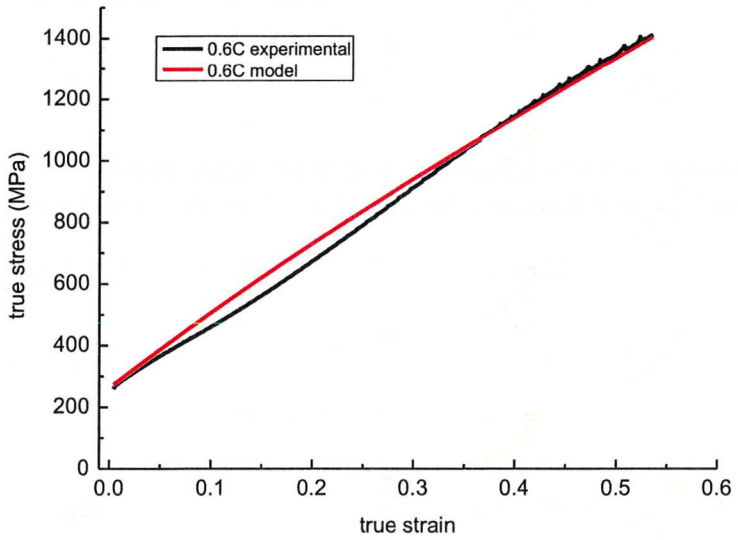

Figure 6.2 Tensile Experimental Results and Model Behaviour for 0.6C Alloy

The individual contributions (σ_1 and σ_2) relating the tensile behaviour due to dislocation glide (isotropic hardening) and due to transformation products (kinematic hardening) was also plotted to determine their various contributions (Figure 6.3). The

isotropic hardening in austenite (σ_1) gave a classic rounded behaviour and contributed more to the modeled flow stress. The kinematic hardening (σ_2) contributed less to the overall flow stress with an increased slope after 0.10 true strain (onset of twinning). The small kinematic contribution to the overall flow stress did not correlate with the experimental kinematic hardening observations as seen in Figure 5.10, where the kinematic hardening contributed significantly to the overall flow stress. The modeled σ_2 contribution was significantly lower than the experimental kinematic hardening trends because the model did not consider the effect of transformation kinetics, resulting in a smaller modeled kinematic hardening contribution compared to the experimental kinematic hardening data. It was seen from σ_1 (isotropic hardening) that without the TWIP effect the alloy would fail early but with the TWIP effect (kinematic hardening, σ_2 contribution) the true stress – strain was maintained and failure was delayed.

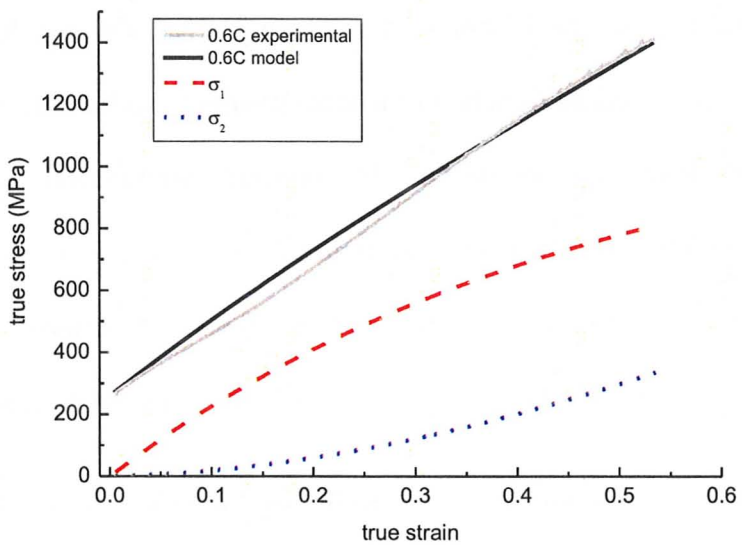

Figure 6.3 Individual Modeling Contributions for 0.6C Alloy

The work hardening rate of the experimental and modeled data are compared in Figure 6.4, with both curves displaying different features. The experimental curve showed an increase in work hardening from 415 to 1000 MPa before holding relatively constant until fracture. The modeled data displayed a continual decrease in work hardening until fracture and crossed over the experimental data at σ~585 MPa. The $\sigma <$ 585 MPa was higher for the modeled data because the kinematic hardening contribution was already taken into account, while in the experimental data, the onset of twinning did not occur until ~415 MPa. At $\sigma >$ 585 MPa, the experimental data was observed to increase in work hardening due to twinning (kinematic hardening contribution), while the model continuously decreased due to the kinematic hardening not contributing significantly enough to overall strengthening.

When looking at the isotropic and kinematic hardening contributions separately (σ_1 and σ_2 respectively), the isotropic hardening had a greater contribution to the work hardening rate relative to the kinematic hardening. The isotropic hardening (from dislocation glide) displayed no benefit to the strengthening mechanism with a continual decrease in work hardening, similar to the modeled contribution. The kinematic hardening contribution (from twinning) continuously increased in work hardening but was not sufficient enough to increase the overall modeled contribution due to the lack of consideration of transformation kinetics to the overall strengthening mechanism.

The differences between the experimental and modeled curves showed that the kinematic hardening contribution does not benefit the modeled data as significantly as within the experimental data. Though the modeled tensile curve fit the experimental data,

the modeled work hardening rate does not adequately capture the hardening mechanisms within the 0.6C alloy. The TWIP effect in the model was seen to not significantly benefit the work hardening rate and twinning not to occur at a steady rate, but starting fast and saturating. In addition, the serrations in the experimental data were also not accounted for in the model as already noted by Bouaziz et al. (Bouaziz 2009).

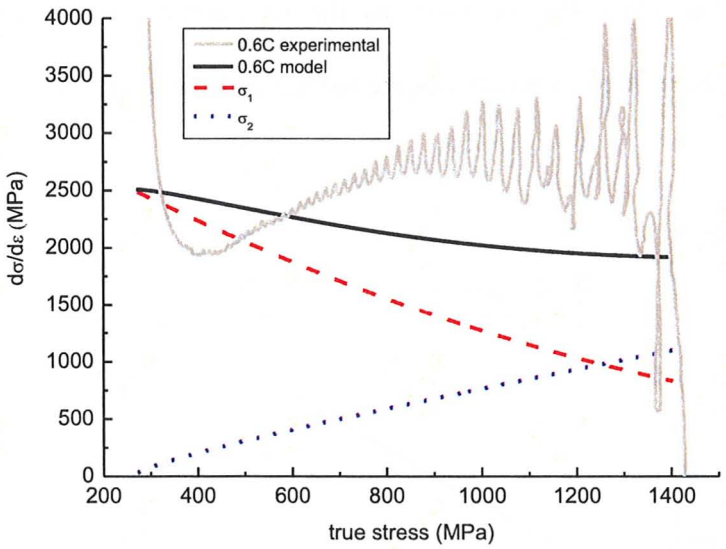

Figure 6.4 Work Hardening Experimental and Model Comparison for 0.6C Alloy

The same model was applied to the 0.4C alloy using Equations 6.1 through 6.3, and the parameters in Table 6.1. The modeled mechanical behaviour was plotted with the experimental tensile curve (Figure 6.5) and showed a reasonably close fit between the two curves. Initially the model and the experimental values were identical before the model began overestimating the flow stress at strain values lower than 0.30. After 0.30 true strain the model prediction was slightly lower than the experimental values,

underestimating the behaviour. The overall estimation was similar to the 0.6C modeled data with large grain size and transformation dynamics playing a key role. One additional consideration for the 0.4C alloy was the presence of ε-martensite, which was not considered in the model of Bouaziz et al. (Bouaziz 2009). The model examined the TWIP effect with various alloys but did not examine alloys with both TWIP and TRIP effects. In considering the effect of ε-martensite, the kinematic hardening contribution may be greater than currently modeled, as the parameter values would need to be recalculated and data refitted to accommodate for the additional effect.

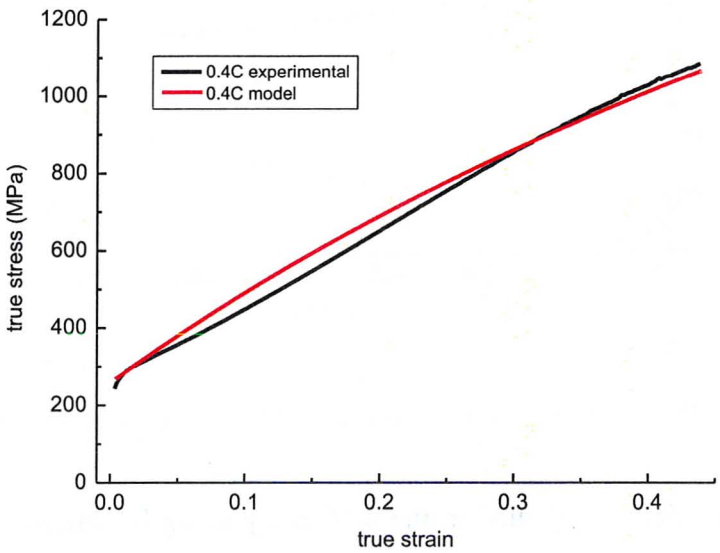

Figure 6.5 Tensile Experimental Results and Model Behaviour for 0.4C Alloy

The individual contributions to the modeled behaviour are seen in Figure 6.6 with σ_1 corresponding to the work hardening without the dynamic composite effect contribution (isotropic hardening) and σ_2 representing the work hardening contribution

from transformation products (kinematic hardening). The model's kinematic hardening contribution was not seen to become significant until approximately 0.12 true strain indicating the kinematic work hardening contribution due to transformation products was not significant until approximately 0.12 true strain. The small kinematic contribution did not match the experimental kinematic contributions (Figure 5.11), where the back stress was seen to contribute significantly to the overall flow stress and with the modeled contribution accounting for little of the overall flow stress. The modeled kinematic hardening contribution was underestimated for its effect to the overall tensile behaviour.

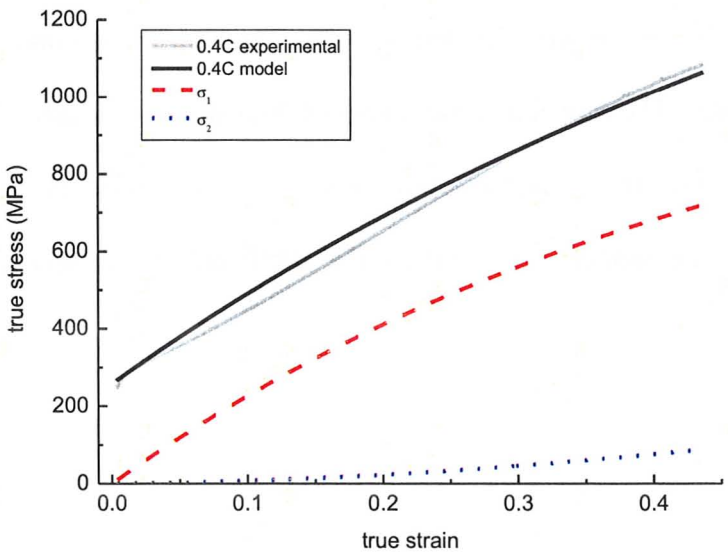

Figure 6.6 Individual Modeling Contributions for 0.4C Alloy

The work hardening behaviour of the experimental and modeled data for the 0.4C alloy was plotted and seen in Figure 6.7 with the two curves being significantly different. The experimental data showed an increase in work hardening from 360 to 670 MPa,

before decreasing to fracture, while the modeled data showed a continual decrease in the work hardening rate until fracture. At $\sigma < 563$ MPa, the experimental data was less than the modeled data, with the dislocation glide primarily contributing to the overall work hardening in the model. For $\sigma > 563$ MPa, the experimental data displayed significant work hardening from twinning while the modeled lacked the kinematic hardening contribution and displayed a continuously decreasing trend.

The continual decrease in the work hardening rate with the modeled data showed that the kinematic hardening contribution within the model was not significant enough to benefit the overall work hardening. The model's isotropic hardening contribution was seen to dominate the overall work hardening behaviour with the continuously decreasing work hardening rate. The model and experimental data were inconsistent due to the lack of consideration for the transformation kinetics, with the TWIP effect being underestimated in the model. As well as the TRIP effect not accounted for in the modeled data.

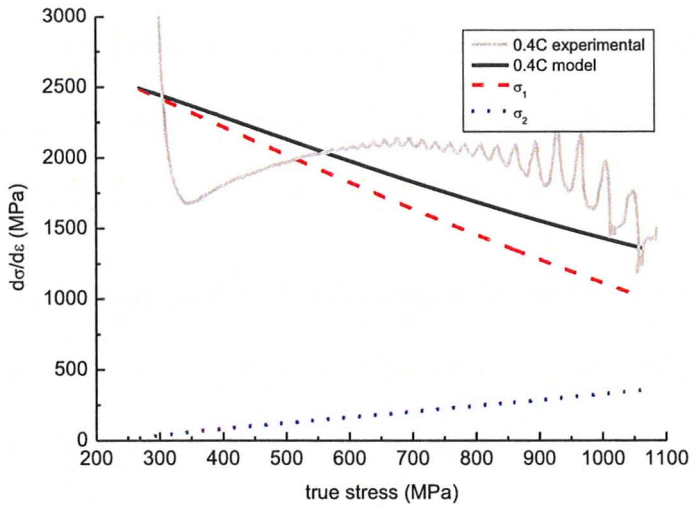

Figure 6.7 Work Hardening Experimental and Model Comparison for 0.4C Alloy

6.4 0.2C Alloy Summary and Analysis

The 0.2C alloy was predicted by the SFE phase map (SFE = 29.6 mJ/m^2) to contain austenite and thermal ε-martensite and, upon deformation, to produce strain-induced ε-martensite causing a TRIP effect. This was confirmed with initial microstructural observations displaying a dual-phase microstructure of austenite grains separated with ε-martensite plates (Figure 5.3). The EBSD phase maps showed transformation of austenite into ε-martensite upon deformation until fracture (Figure 5.24). TEM analysis and specifically Figure 5.25 of the deformed microstructure yielded high dislocation and SF density with fine plates of ε-martensite within grains of austenite. High dislocation density was observed around ε-martensite interfaces and at SF-austenite boundaries. As transformation saturated the microstructure, bent ε-martensite was observed with strain-induced ε-martensite bending the initially present thermal ε-martensite (Figure 5.27). This microstructural evolution was identical to the predictions

made by SFE phase maps as a TRIP alloy and similar to Liang's Fe-24Mn alloy (Liang 2008, Liang 2009), with Liang's alloy having a calculated SFE of 27.9 mJ/m^2, which was lower than the 0.2C alloy. This would possibly explain the larger amounts of ε-martensite observed within the Liang's alloy compared to the 0.2C alloy.

The mechanical behaviour (Figure 5.7) of the 0.2C resulted in an average UTS of 1009 MPa and average true uniform elongation of 0.32. The alloy exhibited higher flow stresses at lower strain levels compared with the 0.4C and 0.6C alloy, with a steady increase in strength until fracture. The work hardening rate (Figure 5.8) was relatively constant until 550 MPa, after which it decreased until fracture. The high work hardening was attributed to the production of ε-martensite as seen from microstructural evolution, with the strain-induced phase acting as new dislocation barriers, strengthening the material. The continued production of ε-martensite resulted in high work hardening rates until saturation at approximately 0.10 true strain (from XRD analysis in Figure 5.13), corresponding to a flow stress of approximately 550 MPa, after which the work hardening decreased to fracture. At saturation, as no more transformation occurred, high dislocation accumulation occurred at austenite- ε-martensite interfaces which led to fracture and relatively low ductility.

Back stress measurements to observe the kinematic hardening trends in the alloy were seen to behave differently compared with the other alloys. The response was seen to comprise a lower proportion of the flow stress as strain increased. The kinematic hardening contribution tapered off after the cessation of ε-martensite transformation at

ε_t=0.10, as seen in Figure 5.12. The production of ε-martensite was the key contributor to the kinematic hardening contribution.

The 0.2C alloy demonstrated a relatively brittle fracture with approximately 3% post-uniform elongation. Fracture analysis revealed numerous voids with some situated at intersections of different transformation products. Grain boundary and interface separation was seen at fracture with separation of the austenite matrix and the transformation products. Cup-cone features, voids, regions of cleavage and micro-cracks were shown on the fracture surface with an increase in the number of cleavage regions relative to the other higher carbon alloys. The primary damage mechanism was the disassociation of γ-ε interfaces and boundaries, with void formation commonly observed in these areas. The production of ε-martensite acted as barriers for dislocation motion until transformation ceased. After which, no effective barriers were introduced for dislocation movement, with dislocations travelling through the ε-martensite, leading to failure.

6.5 Modeling 0.2C Mechanical Behaviour

In modeling the mechanical behaviour of the 0.2C alloy, a different model was applied as the previous model was no longer applicable. The plastic deformation of a microstructure initially containing two phases, austenite and ε-martensite, required a more macroscopic model based on the rule of mixtures. The iso-work model suggested by Bouaziz and Buessler (Bouaziz 2004) considered each increment of work equal in every phase in a disordered microstructure and is discussed in detail in Section 2.7. When

applied to the 0.2C alloy with austenite and ε-martensite phases, Equation 6.7 gives the iso-work condition, with σ_γ and σ_ε as the flow stress in austenite and ε-martensite and ε_γ and ε_ε as local strains in austenite and ε-martensite, respectively. The equation states that the increment of work in one phase is equal to the increment of work in the other phase.

$$\boldsymbol{\sigma_\gamma d\varepsilon_\gamma = \sigma_\varepsilon d\varepsilon_\varepsilon} \tag{6.7}$$

The flow stress and macroscopic strain in Equation 6.8 and 6.9 respectively, are a composite of both austenite and ε-martensite phase weighted by their respective volume fractions, where σ_γ and σ_ε are functions of local strains ε_γ and ε_ε and the volume fraction of ε-martensite, F, is also a function of the applied strain. The flow stress of austenite and ε-martensite followed a Hollomon-type flow rule with a scaling parameter for the austenite phase as seen in Equation 6.10 and 6.11 respectively. Equations 6.7 through Equation 6.11 are similar to the ones discussed in Section 2.7 describing the iso-work model.

$$\boldsymbol{\sigma = (1 - F)\sigma_\gamma + F\sigma_\varepsilon} \tag{6.8}$$

$$\boldsymbol{\varepsilon = (1 - F)\varepsilon_\gamma + F\varepsilon_\varepsilon} \tag{6.9}$$

$$\boldsymbol{\sigma_\gamma = K_1\varepsilon_\gamma^{n_1} + Z} \tag{6.10}$$

$$\boldsymbol{\sigma_\varepsilon = K_2\varepsilon_\varepsilon^{n_2}} \tag{6.11}$$

Using Maple 12 software, Equations 6.10, 6.11 were substituted into 6.8 and integrated to obtain another expression which can be substituted into Equations 6.8 and 6.9. K_1, n_1 and Z parameters were determined by subtracting a Z value from the stress – strain data and fitting the data with a logarithmic plot. The K_2 and n_2 parameters were varied and solved to match the model to the experimental flow stress with the parameters used seen in Table 6.2. The modeled and experimental curves were plotted (Figure 6.8) and the model was seen to closely follow the experimental data. Variations of the modeled data were also plotted to examine distribution of local stresses and strains as a function of the total stress and total strain (global stresses and strains).

Table 6.2 Parameters for 0.2C Iso-Work Model

K_1	n_1	Z	K_2	n_2
2100	1	250	2688	0.646

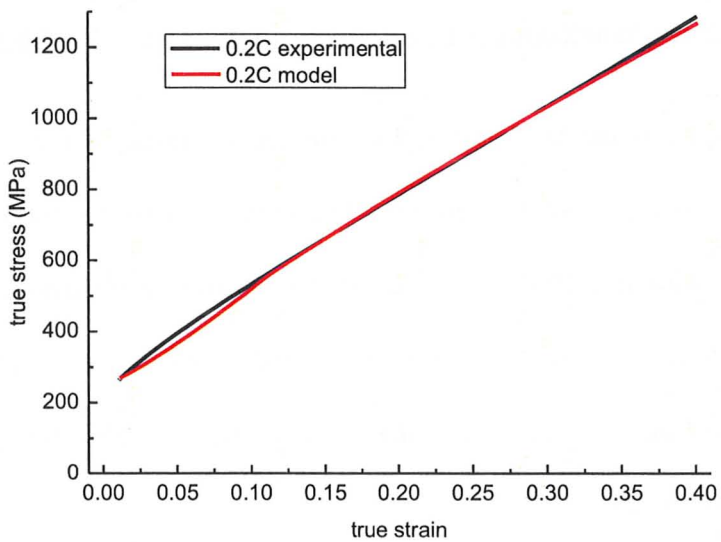

Figure 6.8 Tensile Experimental Results and Model Behaviour of 0.2C Alloy

The local stresses in austenite and ε-martensite were also examined as a function of the global strain as seen in Figure 6.9. The ε-martensite local stress was above the austenite phase indicating the ε-martensite was loaded more heavily. The difference between the model and the two phases was seen to be less at low levels of strain and increased slightly with strain before reaching constant proportions.

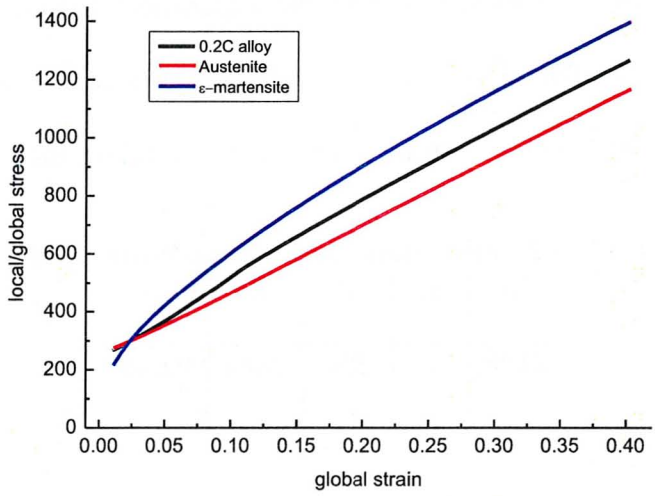

Figure 6.9 Iso-Work Model Local Stress – Global Strain of 0.2C Alloy

Global strain in the 0.2C alloy and the local strains in the two phases from Equation 6.6 were also plotted in Figure 6.10 to show the relative contributions of each phase to strain partitioning. Both austenite and ε-martensite were strained equally at low strains before austenite began contributing more to the global strain. This indicated the austenite as a softer phase compared to the ε-martensite and the difference was seen to increase with global strain.

From looking at the local and global stresses in Equation 6.8, a plot of the individual contributions of austenite and ε-martensite to the global stress is seen in Figure 6.11. The local stresses of both phases increased steadily with the global stress, with the austenite being the lower load bearer and the ε-martensite as the higher load bearing phase.

Overall, the modeled data agreed with the experimental curves, with the global – local stress – strain distributions showing the ε-martensite phase as the primary load bearing phase, with more stress concentration on the ε-martensite relative to the austenite phase.

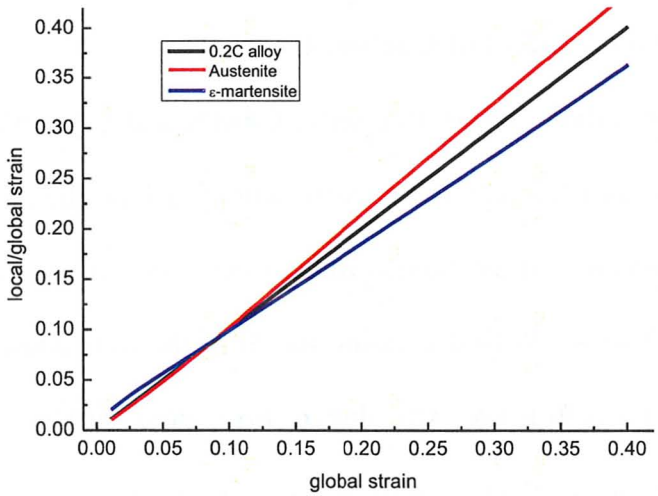

Figure 6.10 Iso-Work Model Strain Partitioning of 0.2C Alloy

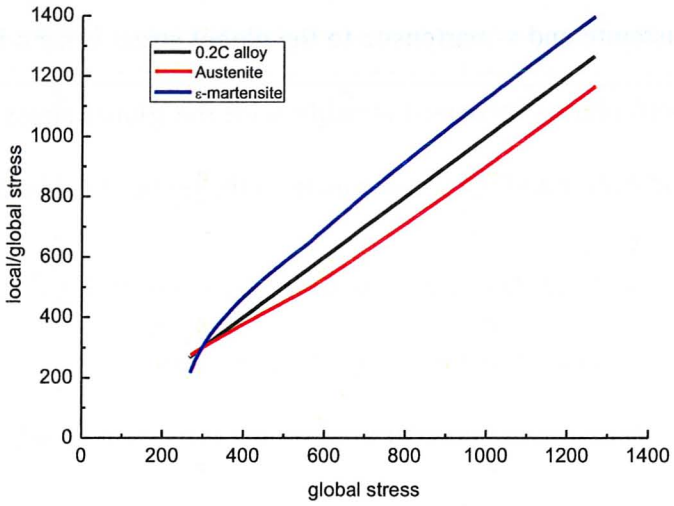

Figure 6.11 Iso-Work Model Stress Partitioning of 0.2C Alloy

6.6 Analysis on Effect of Carbon Content

The effect of carbon content (0.6 wt%, 0.4wt% and 0.2 wt%) on the three Fe-22Mn-C alloys was seen through the microstructural and mechanical evolution. The change in the SFE was one of the main considerations when varying the carbon content from 0.6 wt% to 0.2 wt%. With decreasing the SFE, the SFE phase map (Figure 2.5) showed the initial microstructure was shifted from pure austenite to a dual phase austenite-ε-martensite microstructure with SFE of 37, 33 and 30 mJ/m^2 being calculated for the 0.6C, 0.4C and 0.2C alloys respectively. The lower SFE made the dual-phase microstructure more energetically favourable compared to the pure austenite structure.

The deformation products were also changed due to the change in carbon content, going from mechanical twinning in the 0.6C and 0.4C alloys to production of ε-martensite in the 0.4C and 0.2C alloys. The highest carbon alloy (0.6C) exhibited the TWIP effect

and the lowest carbon alloy (0.2C) showed the TRIP effect with the 0.4C alloy displaying both TWIP and TRIP effects. The lowering of the carbon content and the production of ε-martensite made the 0.2C alloy stronger but less ductile, reaching high strengths quickly but failing at relatively low uniform elongations. The higher carbon alloys with twinning were slowly strengthened reaching higher ductilities compared to the 0.2C alloy.

With an alloy containing both TWIP and TRIP (0.4C), the microstructural evolution was seen to be dominated by the TWIP effect with mechanical twinning being the dominate deformation product observed in the EBSD phase maps. The SFE value (Allain 2004b) predicted that ε-martensite would be the primary deformation product, but microstructural analysis showed ε-martensite to play a lesser role in the microstructural evolution. This showed that the microstructural and mechanical behaviour cannot be solely predicted using the SFE, but that other factors need to be considered. This was also observed from work done by Wang et al. (Wang 2010) where the carbon content was seen to affect the SFE and the interaction with dislocations, demonstrating that at the SFE does not determine the overall microstructure and deformation mechanism. An increase in carbon was seen to increase the work hardening rate and improves the chance of twinning, as twinning is more stress-induced compared with the TRIP effect which is strain-induced (Wang 2010)

The mechanical behaviour of the 0.4C was seen to be mixed between the TWIP and TRIP effect, with work hardening behaviour similar to the higher carbon alloy but with the fracture limited in a similar way to the lower carbon alloy. The steadily increasing and constant work hardening seen by the 0.4C alloy was similar to the 0.6C

alloy, with similar serrations also exhibited. The presence of ε-martensite limited the ductility and dominated the fracture behaviour, similar to that seen in the 0.2C alloy.

Looking at other alloys with different carbon contents, the Fe-24Mn alloy by of Liang (Liang 2008), had virtually no carbon at all, with SFE = 27.9 mJ/m^2, behaving similarly to the 0.2C alloy yet producing more ε-martensite. The Fe-30Mn alloy of Liang with no carbon had SFE = 34.1 mJ/m^2, similar to that of the 0.4C alloy, but displayed a fully austenitic microstructure with only dislocation glide for the majority of its deformation with little twinning observed near fracture. With an increase in carbon content, Wang's Fe-30-0.5C alloy (Wang 2010) with SFE of 41.8 mJ/m^2, showed mechanical twinning upon tensile strain. Other alloys that also exhibiting the TWIP effect include Chen's Fe-18Mn0.6C alloy (Chen 2007) with SFE = 34.7 mJ/ m^2, a similar SFE value to Liang and Wang's Fe-30Mn alloy which only displayed dislocation glide. The SFE and the phase map predictions within the different alloys show that the SFE alone does not determine the deformation mechanism but that other factors play a role in the microstructural evolution and mechanical behaviour.

Overall, with the varying carbon content, the SFE change was a factor in the different microstructures and properties exhibited. However the SFE change was not the only factor to be considered as alloys with similar SFEs exhibited different properties and vice versa. The thermodynamics of the SFE and the predication of energetically favourable phases were, therefore, guidelines but were found not to dictate the alloy microstructure and deformation mechanism. The carbon-dislocation interaction also had an effect on the microstructure and deformation mode.

7. CONCLUSIONS

The Fe-22Mn-C alloys are suitable materials for the automotive industry due to their high sustained work hardening rates, leading to high strengths and ductilities. The effect of carbon content on the microstructural and mechanical property evolution was studied for Fe-22Mn-C alloys containing 0.6 wt%, 0.4 wt% and 0.2 wt% C.

The as-annealed microstructure of the 0.6C and 0.4C alloy revealed a matrix of equiaxed austenite grains with a few annealing twins prior to deformation. The 0.6C had a higher SFE than the 0.4C (37.2 mJ/m^2 and 33.4 mJ/m^2, respectively), with SFE calculations based on Allain et al. (Allain 2004b) predicting an austenitic microstructures for both alloys. The 0.2C alloy with a SFE of 29.6 mJ/m^2 revealed a dual-phase microstructure containing austenite grains separated by plates of thermal ε-martensite, as expected by the SFE predictions of Allain et al. (Allain 2004b).

The 0.6C alloy revealed sustained high rates of work hardening with high strength and ductility. An increase in the work hardening rate at 415 MPa arose from the onset of mechanical twinning. The production of twins and resultant back stresses contributed significantly to the overall flow stress, with the back stress increasing with twin production and saturating with twin saturation. The 0.4C alloy revealed a similar work hardening trend as the 0.6C alloy with lower overall strengths and ductilities. The onset of twinning and production of ε-martensite was observed with an increase in the work hardening rate at 360 MPa. The kinematic hardening contribution was attributed to the production of twins and ε-martensite and began saturating due to ε-martensite -

dislocation interactions and upon completion of ε-martensite production. The 0.2C alloy displayed high work hardening rates which quickly decreased to fracture with relatively low ductility achieved. The production of ε-martensite contributed to the high work hardening rates with saturation at approximately around 550 MPa. The Bauschinger effect within the 0.2C alloy revealed a significant contribution to the overall flow stress, with the back stress trend saturating at the end of ε-martensite production.

Attempts to model the mechanical behaviour of the 0.6C and 0.4C alloy required some modifications to the model of Bouaziz et al. (Bouaziz 2009) in order to fit the experimental data. The isotropic hardening was seen to contribute more to the overall flow stress with the kinematic hardening having a smaller effect and initiated at higher strains. The work hardening comparison of the experimental and modeled data showed the effect of the small kinematic hardening contribution with the work hardening rate not sustained by the kinematic hardening contribution. The disagreement in the work hardening rate for the modeled and experimental curves was due to no modeling of transformation kinetics, underestimating the overall kinematic hardening contribution.

The iso-work model by Bouaziz et al. (Bouaziz 2004) applied to the 0.2C alloy showed consistency between experimental and modeled data. Global and local stresses - strains were also plotted to understand the distribution of loads within each phase, with ε-martensite bearing more of the load relative to austenite. Both models were applicable to the alloys chosen and displayed an adequate match with the experimental flow stress data.

The microstructural evolution of the 0.6C alloy from EBSD phase maps revealed production of twins as the primary deformation product with XRD analysis showing no significant ε-martensite produced during deformation, thus confirming the SFE predictions of the TWIP effect as the primary deformation mechanism. The 0.4C alloy contained mechanical twins and strain-induced ε-martensite as deformation products with saturation of ε-martensite at 0.20 true strain, correlating with the kinematic hardening saturation. The microstructural evolution observed agreed with the TWIP – TRIP deformation mechanism per the SFE predictions. The 0.2C alloy contained austenite and ε-martensite with production of ε-martensite increasing upon deformation creating a TRIP effect as the deformation mechanism. Saturation of ε-martensite production occurred at 0.10 true strain, correlating with the saturation of the kinematic hardening contribution.

Fracture analysis of the 0.6C alloy revealed a highly necked region with the main damage mechanism being the linking of voids along grain or twin boundaries and led to an overall ductile failure. The fracture of the 0.4C alloy displayed various features with high dislocation density at ε-martensite interfaces concentrating stress and ultimately leading to fracture. The 0.2C alloy demonstrated relatively brittle failure with low post-uniform elongation. The primary damage mechanism was void nucleation and growth at the γ-ε boundaries and interfaces with ε-martensite containing high dislocation density.

The effect of carbon on the Fe-22Mn-C alloy was decreased SFE with decreasing carbon content. The decrease in carbon content shifted the thermodynamically favoured deformation mechanism from TWIP to TRIP effect. The strength and ductility of the alloys was lowered by the presence of ε-martensite. However, the interactions between

phases (twins, ε-martensite), dislocations, and the role of carbon also played a factor in the extent of the SFE influence on the mechanical behaviour and microstructural evolution. The presence of carbon allows for an increase in the work hardening rate and favours the TWIP effect (stress induced) over the TRIP effect (strain induced). Overall, the 0.6C TWIP alloy was the most suitable candidate for the automotive industry, with mechanical twins leading to high work hardening rates and a good combination of strength and ductility.

8. REFERENCES

Allain, S., Chateatu, J.-P. & Bouaziz, O. 2004a. A physical model of the twinning-induced plasticity effect in a high manganese austenitic steel. *Materials Science and Engineering A*, 387-389, 143-147.

Allain, S.,Chateau, J.-P., Bouaziz, O., Migot, S. & Guelton, N. 2004b. Correlations between the calculated stacking fault energy and the plasticity mechanisms in Fe-Mn-C alloys. *Materials Science and Engineering A*, 387-389, 158-162.

Allain, S., Chateau, J.-P., Dahmoun, D. & Bouaziz, O. 2004c. Modeling of mechanical twinning in a high manganese content austenitic steel. *Materials Science and Engineering A*, 387-389, 272-276.

Barbier, D., Gey. N., Allain, S., Bozzolo, N. & Humbert, M. 2009. Analysis of the Tensile Behaviour of a TWIP Steel Based on the Texture and Microstructure Evolutions. *Materials Science and Engineering A*, 500, 196-206.

Bate, P.S. & Wilson, D.V. 1986. Analysis of the Bauschinger Effect. *Acta Metallurgica*, 34(6), 1097-1105.

Bian, Y., 2009. Microstructure and Mechanical Properties of Al and Al/Si Alloyed TRIP-Assisted Steels Produced Through Galvanizing Heat Treatments. M.A.Sc. thesis. McMaster University.

Bracke, L., Mertens, G., Penning, J., De Cooman, B.C., Liebeherr, M., Akdut, N. 2006. Influence of Phase Transformations on the Mechanical Properties of High-Strength Austenitic Fe-Mn-Cr Steel. *Metallurgical and Materials Transactions A*, 37A, 307-317.

Bouaziz, O. & Guelton, N. 2001. Modelling of TWIP effect on work-hardening. *Materials Science and Engineering A*, 319-321, 246-249.

Bouaziz, O. & Buessler, P. 2004. Iso-work Increment Assumption for Heterogeneous Material Behavior Modelling. *Advanced Engineering Materials*, 6(1-2), 79-83.

Bouaziz, O. & Embury, J.D. 2007. Microstructural design for advanced structural steels. *Materials Science Forum*, 539-543, 42-50.

Bouaziz, O., Allain, S. & Scott, C. 2008. Effect of grain and twin boundaries on the hardening mechanisms of twinning-induced plasticity steels. *Scripta Materialia*, 58, 484-487.

Bouaziz, O., Zurob, H., Chehab, B., Embury, J.D., Allain, S. & Huang, M. 2009. Effect of chemical composition on work hardening of Fe-Mn-C TWIP steels. *Materials Science and Technology,* doi: 10.1179/026708309X12535382371852.

Chen, L., Kim, H.S., Kim, S.K. & De Cooman, B.C. 2007. Localized Deformation due to Portevin-LeChatelier Effect in 18Mn-0.6C TWIP Austenitic Steel. *ISIJ International*, 47(12), 1804-1812.

Dastur, Y.N. & Leslie, W.C. 1981. Mechanism of Work Hardening in Hadfield Manganese Steel. *Metallurgical Transactions A*, 12A, 749-759.

De Cooman, B.C., Chen, L., Kim, H.S., Estrin, Y., Kim, S.K. & Voswinckel, H. 2009. State-of-the-Science of High Manganese TWIP Steels for Automotive Applications. *Microstructure and Texture in Steels*, 2, 165-183.

Ferreira, P.J. & Müllner, P. 1998. A Thermodynamic Model for Stacking-Fault Energy. *Acta Materllurgica*, 46(16), 4479-4484.

Frommeyer, G., Brüx, U. & Neumann, P. 2003. Supra-Ductile and High-Strength Manganese-TRIP/TWIP Steels for High Energy Absorption Purposes. *ISIJ International*, 43(3), 438-446.

Grässel, O., Krüger, L., Frommeyer, G. & Meyer, L.W. 2000. High strength Fe-Mn-(Al,Si) TRIP/TWIP steels development – properties – application. *International Journal of Plasticity*, 16, 1391-1409.

Gutierrez-Urrutia, I., Zaefferer, S. & Raabe, D. 2010. The effect of grain size and grain orientation on deformation twinning in Fe-22wt%Mn-0.6wt%C TWIP steel. *Materials Science and Engineering A*, 527, 3552-3560.

Karaman, I., Sehitoglu, H., Gall, K., Chumlyakov, Y.I. & Maier, H.J. 2000a. Deformation of single crystal Hadfield steel by twinning and slip. *Acta Materialia*, 48, 1345-1359.

Karaman, I., Sehitoglu, H., Beaudoin, A.J., Chumlyakov, Y.I., Maier, H.J. & Tomé, C.N. 2000b. Modeling the deformation behaviour of Hadfield steel single and polycrystals due to twinning and slip. *Acta Materialia*, 48, 2031-2047.

Karaman, I., Sehitoglu, H., Chumlyakov, Y.I., Maier H.J. & Kireeva, I.V. 2001. The Effect of Twinning and Slip on the Bauschinger Effect of Hadfield Steel Single Crystals. *Metallurgical and Materials Transactions A*, 32A, 695-706.

Kelly, A. & Groves, G.W. 1970. *Crystallography and Crystal Defects*. Harlow: Longmans.

Kocks, U.F. & Mecking, H. 2003. Physics and phenomenology of strain hardening: the FCC case. *Progress in Materials Science*, 48, 171-273.

Hamada, A.S., Karjalainen, L.P., Ferraiuolo, A., Gil Sevillano, J., De Las Cuevas, F., Pratolongo, G. & Reis, M. 2010. Fatigue Behaviour of Four High-Mn Twinning Induced Plasticity Effect Steels. *Metallurgical And Materials Transactions A*, 41A, 1102-1108.

Idrissi, H., Ryelandt, L., Veron, M., Schryvers, D. & Jacques, P.J. 2009. Is there a relationship between the stacking fault character and the activated mode of plasticity of Fe-Mn-based austenitic steels? *Scripta Materialia*, 60, 941-944.

Idrissi, H., Renard, K., Ryelandt, L., Schryvers, D. & Jacques, P.J. 2010. On the Mechanism of Twin Formation in Fe-Mn-C TWIP steels. *Acta Materialia*, 58, 2464-2476.

Kim, J.K., Chen, L., Kim, H.S., Kim, S.K., Estrin, Y. & De Cooman, B.C. 2009. On the Tensile Behaviour of High-Manganese Twinning-Induced Plasticity Steel. *Metallurgical and Materials Transactions A*, 40A, 3147-3158.

Lee, Y-K., Choi, C-S. 2000. Driving Force for γ→ε Martensitic Transformation and Stacking Fault Energy of γ in Fe-Mn Binary System. *Metallurgical and Materials Transactions A*, 31A, 355-360.

Liang, X. 2008. Structure and Mechanical Properties of Fe-Mn Alloys. M.A.Sc. thesis. McMaster University.

Liang, X., McDermid, J.R., Bouaziz, O., Wang, X., Embury, J.D. & Zurob, H.Z. 2009. Microstructural evolution and strain hardening of Fe-24Mn and Fe-30Mn alloys during tensile deformation. *Acta Materialia*, 57, 3978-3988.

Lü, Y., Hutchinson, B., Molodov, D.A. & Gottstein, G. 2010. Effect of deformation and annealing on the formation and reversion of ε-martensite in an Fe-Mn-C alloy. *Acta Materialia*, 58, 3079-3090.

Nagy, E., Mertinger, V., Tranta, F., Sólyom, J. 2004. Deformation Induced Martensitic Transformation in Stainless Steels. *Materials Science and Engineering A*, 378, 308-313.

Nakano, J., Jacques, P.J. 2010. Effects of the Thermodynamic Parameters of the HCP Phase on the Stacking Fault Energy Calculations in the Fe-Mn and Fe-Mn-C Systems. *CALPHAD*, 34, 167-175.

Olson, G.B. & Cohen, M. 1976a. A General Mechanism of Martensitic Nucleation: Part I. General Concepts and the FCC → HCP Tranformation. *Metallurgical Transactions A*, 7A, 1897-1904.

Olson, G.B. & Cohen, M. 1976b. A General Mechanism of Martensitic Nucleation: Part III. Kinetics of Martensitic Nucleation. *Metallurgical Transactions A*, 7A, 1915-1923.

Putaux, J.-L. & Chevalier, J.-P. 1996. HREM Study of Self-Accomdated Thermal ε-Martensite in an Fe-Mn-S-Cr-Ni Shape Memory Alloy. *Acta Materialia*, 44(4), 1701-1716.

Reed-Hill, R.E., Abbaschian, R. 1992. *Physical Metalurgy Principles*. PWS-Kent Publishing Co., Boston, 3.

Rémy, L. 1981. The Interaction Between Slip and Twinning Systems and in the Influence of Twinning on the Mechanical Behavior of fcc Metals and Alloys. *Metallurgical Transactions A*, 12A, 387-407.

Rémy, L. & Pineau A. 1976. Twinning and Strain-Induced F.C.C. → H.C.P. Transformation on the Mechanical Properties of Co-Ni-Cr-Mo Alloys. *Materials Science and Engineering*, 26, 123-132.

Rémy, L. & Pineau A, 1977. Twinning and Strain-Induced F.C.C. → H.C.P. Transformation in the Fe-Mn-Cr-C System. *Materials Science and Engineering*, 28, 99-107.

Scott, C., Guelton, N., Allain, S. & Faral, M. 2005. The Development of a New Fe-Mn-C Austenitic Steel for Automotive Applications. *Materials Science & Technology 2005 Conference*. 127-138.

Sowerby, R., Uko, D.K. 1979. A Review of Certain Aspects of the Bauschinger Effect in Metals. *Materials Science and Engineering*, 41, 43-58.

Spencer, K. 2004. The Work Hardening of Austenitic Stainless Steel, Applied to the Fabrication of High-Strength Conductors. Ph.D. thesis, McMaster University.

Thermo-Calc Software available at www.thermocalc.com.

Venables, J.A., de Angelis, R.J., & Cohen, J.B. 1963. Deformation Twinning. *Metall. Soc. A.I.M.E.*, Gordon & Breach, New York, 25 (2), 77–116.

Wang, X. 2009. TEM Analysis, Private Communications.

Wang, X., Zurob, H.S., Embury, J.D., Ren, X. & Yakubtsov, I. 2010. Microstructural features controlling the deformation and recrystallization behaviour of Fe-30%Mn and Fe-30%Mn-0.5%C. *Materials Science and Engineering A*, 517, 3785-3791.

9. APPENDIX

9.1 CO/CO_2 Decarburization Equations

The time required to decarburize the steel was determined with diffusion equations using Maple Programming Software with the following conditions. A sheet of $2l$ thickness was placed in carbon rich atmosphere with temperature T and decarburizing time t. The initial uniform concentration of the steel (Cp), decarburizing concentration (Cs) and diffusion coefficient DC with a schematic shown in Figure 9.1 with Cs<Cp, creating a decarbuizing atmosphere instead of a carburizing atmosphere as shown in the figure. The diffusion solution for a plane of thickness $2l$ is given in Equation 8.1 with initial conditions, C=Cp, $-l<x<l$, t=0 and boundary conditions, C=Cs, $x=\pm l$, $t\geq 0$. The diffusion coefficient was calculated for T=1100°C and found to be 6.1315e-12 m^2/s. The conditions were set with Cs=0.20 and Cp=0.60 to determine the time t required to decarburize the steel with thickness of 1.5 mm (l=7.5e-4 m). The calculated decarburization time required was four hours for the 0.2C alloy and was kept consistent for the other two alloys.

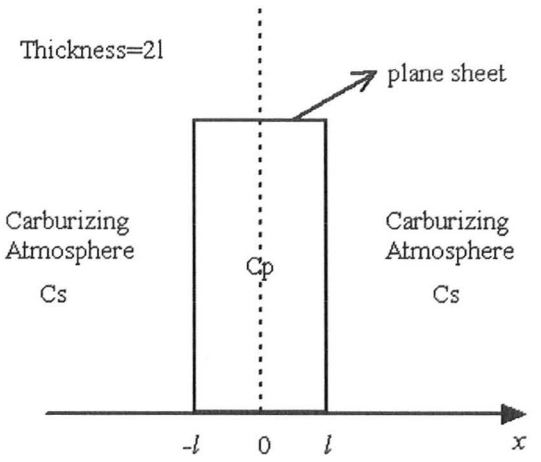

Figure 9.1 Decarburization Illustration

$$\frac{C - Cp}{Cs - Cp} = 1 - \frac{4}{\pi}\sum_{n=0}^{\infty}\frac{(-1)^n}{2n+1}e^{-\frac{DC(2n+1)^2\cdot\pi^2\cdot t}{4l^2}}\cos\left(\frac{(2n+1)\cdot\pi\cdot x}{2l}\right) \quad \textbf{(8.1)}$$

9.2 Calculating CO/CO_2 Gas Ratios

Using Thermo-Calc Software, the CO/CO_2 ratio was determined by fixing the carbon activity on the surface and calculating the ratio of gas needed to acquire that activity. The commands used are listed in Table 9.1 with an explanation of why the command was used. The conditions are set for the 0.2C alloy and the activity was determined. The system was set again with the specific activity required and the CO/CO_2 gas needed to achieve that was calculated with commands in Table 9.2. The resultant CO and CO_2 were calculated to determine the gas ratio required. The same method was applied to the 0.4C alloy to determine the CO/CO_2 gas ratio with a change in the composition in the set conditions. A summary of the expected activities and gas ratios are listed in Table 9.3 for the 0.2C and 0.4C alloys.

Table 9.1 Thermo-Calc Commands to Determine C Activity

Command	Purpose
Goto d:	Selecting data base
Def-sys	Defining system
Fe Mn C	Defining system to contain Fe, Mn and C
Get	Get references in data base
Go p-3	Go to poly-3 data base
S-c	Set conditions
n=1 p=101325 T=1373 w(Mn)=0.22 w(C)=0.002	Setting composition, pressure, temperature for 0.2C alloy
L-c	List conditions set above to confirm
C-e	Calculate equilibrium based on set conditions
L-e (need to push enter twice)	List equilibrium conditions

Table 9.2 Thermo-Calc Commands to Determine CO/CO_2 Ratio

Command	Purpose
Goto d:	Selecting data base
Switch ssub3	Switching to new gas database
Def-sys	Defining system
C O	Defining system to contain C and O
Get	Get references in data base
Go p-3	Go to poly-3 data base
S-c	Set conditions

n=1 p=101325 T=1373 arc(C)=3.7896e-3	Setting activity, pressure, temperature for 0.2C alloy
L-c	List conditions set above to confirm
C-e	Calculate equilibrium based on set conditions
L-e	List equilibrium conditions

Table 9.3 Activities and Gas Ratios for 0.2C and 0.4C Alloy

Alloy	acr(C)	CO	CO_2	Gas Ratio
0.2C	3.7896e-3	9.3063e-1	6.9374e-2	13.41
0.4C	8.1266e-3	9.6520e-1	3.4799e-2	27.74

9.3 Detailed Mounting Conditions

Cold epoxy mounts were made with 15 parts resin and 2 parts hardener and set to harden for at least eight hours prior to removing from the holder. Mounts were used Scanning Electron Microscopy (SEM) secondary electron imaging as well as X-Ray Diffraction (XRD) analysis. Samples could also be prepared by being glued to resin mounts using Krazy® glue for simple polishing using the automatic polisher. Samples would then be demounted by use of acetone prior to electropolishing, for analysis by Electron Back-Scattered Diffraction (EBSD).

9.4 Detailed Polishing Conditions

Struers® Automatic Polisher was used for polishing prior to SEM imaging, XRD analysis and electropolishing for EBSD. It was important to clean the sample surface

after each polishing step to avoid contamination from cloths, lubricants or other factors. Water was sed as a lubricant and for cleaning at early polishing stages and not used at finer polishing stages, with samples rinsed with ethanol instead. The polishing procedure followed is outlined in Table 9.4. The OM was used between steps to examine the surface for significant scratches and if steps needed to be repeated.

Table 9.4 Polishing Steps

Cloth	Time (min)	Load (N)	Lubricant
SiC-800	5	5	Water
SiC-1200	10	5	
SiC-2400	10	5	
SiC-2400	10	5	
MD-Dac 3μm diamond	15	10	BLUE
MD-Nap 1μm diamond	15	10	

9.5 Detailed Etching Conditions

The solution of 5% nitric acid in methanol was prepared each time prior to etching in order to ensure fresh etchant for maximum effectiveness in revealing the microstructure. The samples were immersed and swabbed with the etchant for approximately 45 seconds to reveal the microstructural features. All sample rinsing and cleaning was performed with ethanol to avoid adverse reactions of the sample surface.